Reference: Swayze, G.A., R.N. Clark, A.F.H. Goetz, T.G. Chrien, and N.S. Gorelick, Effects of spectrometer band pass, sampling, and signal-to-noise ratio on spectrometer identification using the Tetracorder algorithm, *Journal of Geophysical Research, 108*(E9), 5105, doi:10.1029/2002JE001975, 2003.

The Effects of Spectrometer Bandpass, Sampling, and Signal-to-Noise Ratio on Spectral Identification Using the Tetracorder Algorithm

Gregg A. Swayze[1], Roger N. Clark[1], Alexander F.H. Goetz[2], Thomas G. Chrien[3], and Noel S. Gorelick[4]

[1]U.S. Geological Survey, MS 964 Box 25046
Denver Federal Center, Denver, Colorado 80225
(303) 236-0925 email: gswayze@speclab.cr.usgs.gov

[2]Center for the Study of Earth from Space (CSES)/
Cooperative Institute for Research in Environmental Sciences (CIRES) and
Department of Geological Sciences
University of Colorado, Boulder, Colorado 80309-0216

[3]Raytheon, Electronics Systems, Mailstop E51/A290
2000 East El Segundo Boulevard
P.O. Box 902
El Segundo, CA 90245-0902

[4]Mars Global Surveyor (TES) Space Flight Facility
Department of Geology, Box 871404, Arizona State University
Tempe, Arizona 85287-1404

Version 3.1 3/17/03

1.0 ABSTRACT

Estimates of spectrometer bandpass, sampling interval, and signal-to-noise ratio required for identification of pure minerals and plants were derived using reflectance spectra convolved to AVIRIS, HYDICE, MIVIS, VIMS, and other imaging spectrometers. For each spectral simulation, various levels of random noise were added to the reflectance spectra after convolution and then each was analyzed with the Tetracorder spectral identification algorithm (Clark et al., 2003). The outcome of each identification attempt was tabulated to provide an estimate of the signal-to-noise ratio at which a given percentage of the noisy spectra were identified correctly. Results show that spectral identification is most sensitive to the signal-to-noise ratio at narrow sampling interval values but is more sensitive to the sampling interval itself at broad sampling interval values because of spectral aliasing – a condition when absorption features of different materials can resemble one another. The bandpass is less critical to spectral identification than the sampling interval or signal-to-noise ratio because broadening the bandpass does not induce spectral aliasing. These conclusions are empirically corroborated by analysis of mineral maps of AVIRIS data collected at Cuprite, Nevada between 1990 and 1995, a period during which the sensor signal-to-noise ratio increased up to sixfold. There are values of spectrometer sampling and bandpass beyond which spectral identification of materials will require an abrupt increase in sensor signal-to-noise ratio due to the effects of spectral aliasing. Factors that control this threshold are the uniqueness of a material's diagnostic absorptions in terms of shape and wavelength isolation, and the spectral diversity of the materials found in nature and in the spectral library used for comparison. Array spectrometers provide the best data for identification when they critically sample spectra. The sampling interval should not be broadened to increase the signal-to-noise ratio in a photon-noise-limited system when high levels of accuracy are desired. It is possible, using this simulation method, to select optimum combinations of bandpass, sampling interval, and signal-to-noise ratio values for a particular application that maximize identification accuracy and minimize the volume of imaging data.

2.0 INTRODUCTION

The increasing pace of imaging spectrometer development worldwide is a testimony to the emerging uses for high spectral resolution data. However, little study of the spectral resolution and detector sensitivity required to identify surface materials has occurred, in large part, because the development of identification algorithms and spectral libraries has lagged behind spectrometer design and construction. Although spectrometer sensitivity continues to increase with advances in detector and optical technology, the question remains: what level of sensitivity is needed to confidently identify surface materials? Aspects of this question can be answered by systematically surveying how the spectral signatures of surface materials vary as a function of sensor spectral resolution and detector sensitivity, thus allowing the tradeoffs between these spectral parameters to be better understood and incorporated into the designs of future imaging spectrometers.

Previous studies evaluated the effects of spectral resolution and signal-to-noise ratio on identification of agricultural crops using data from broad-band sensors (Fu et al., 1969; Ready et al., 1971; and Landgrebe, 1978). Goetz and Calvin (1987) simulated the effects of spectral

resolution and signal-to-noise ratio on identification using binary vector analysis and maximum likelihood classification to measure the success rate of separating closely spaced Gaussian absorptions that had various levels of random noise. Although this study used synthetic Gaussian absorptions of identical size instead of overlapping natural absorptions, it was among the first to use simulated hyperspectral data. Goetz and Boardman (1989) added scaled random noise to synthetic Gaussian spectra and six natural mineral spectra and then subjected these to endmember unmixing to determine the percentage of correct identifications. Their study showed a linear relationship between misidentifications, spectral noise, and spectral resolution. The present study is an extension of these earlier studies.

3.0 BACKGROUND

Some background information is necessary in order to evaluate the methods used to simulate the performance of the imaging spectrometers. We review the definitions of signal-to-noise ratio, sampling interval and bandpass, examine the design of the four imaging spectrometers, define the two spectral regions used for identifying materials, and present an overview of the Tetracorder identification algorithm (Clark et al., 2003).

3.1 The Electronic and Vibrational Spectral Regions

There are a variety of electronic and vibrational processes that shape reflectance spectra of surface materials (Hunt, 1977). The electronic absorptions occur primarily from 0.1 - 1.35 μm and vibrational absorptions occur from about 0.9 to 1000 μm. Both spectral regions are used to identify surface materials, although each provides spectral information originating from different mechanisms. This study models identification using the visible - shortwave infrared (VIS - SWIR) spectral region from 0.4 - 2.5 μm because this is the wavelength range of most imaging spectrometers that measure reflected light. Electronic absorptions arise from charge transfers and crystal field effects of the transition-metals, conduction bands and color centers. In this study we refer to the 0.4 - 1.35 μm region as the electronic absorption region. Vibrational absorptions arise from vibrational modes of molecular bonds. In this study we use overtone and combination band absorptions in the reflected light portion of the spectrum located within the 1.35 - 2.5 μm region, here referred to as the vibrational region. These absorptions occur at shorter wavelengths than the fundamental absorptions and are considerably weaker, but in many cases they are detectable with remote sensing. Because electronic and vibrational processes are active at different wavelengths, spectral identifications can be made for different classes of surface materials using information from these two spectral regions (Hunt, 1977; Clark, 1999; Clark et al., 2003).

The intensity of spectral features in reflectance is a function of the intrinsic absorption strength, scattering properties, and abundance of a material (Hapke, 1981, and references therein). For a number of reasons the absorptions of one material may dominate an entire wavelength region in a mixture (Clark 1983; Clark, 1999). For example, the reflectance spectrum of an intimate mixture of equal amounts of alunite and jarosite is dominated in the vibrational region by alunite with its intense 2.17-μm absorption as compared with jarosite and its weaker absorption at 2.27 μm (Figure 1). Jarosite, with a 0.92-μm Fe^{3+}-absorption, dominates the electronic region because alunite lacks any significant absorptions at these wavelengths. This

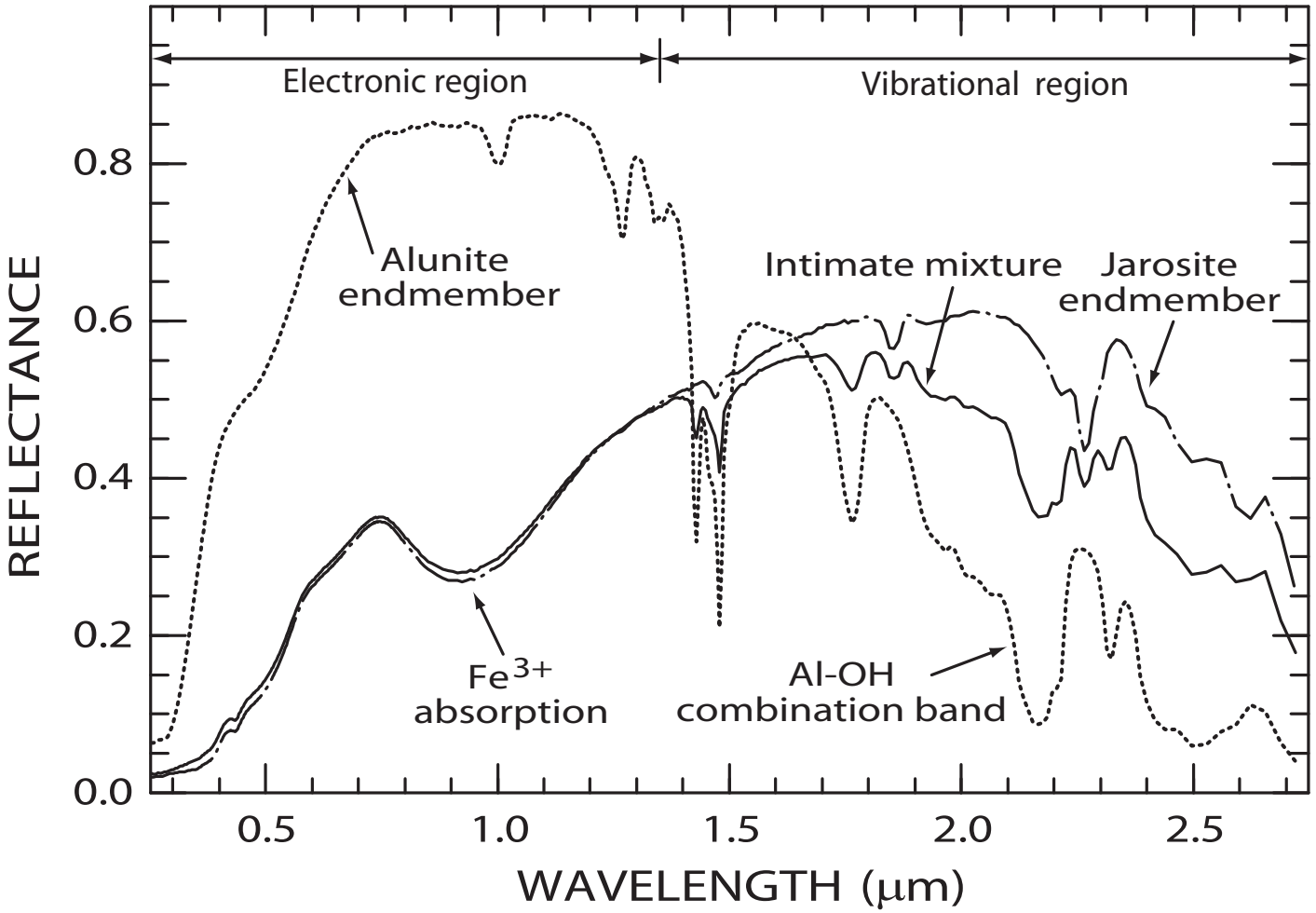

Figure 1. Reflectance spectra of an intimate mixture of 50 wt% alunite and 50 wt% jarosite, as well as alunite and jarosite endmembers. Jarosite has an electronic Fe^{3+} absorption at 0.95 μm and alunite has a vibrational Al-OH combination absorption band at 2.17μm. Note that jarosite spectrally dominates the electronic region while alunite dominates the vibrational region in the intimate mixture.

distinction, identified while testing single components, is applicable to spectra of intimate and areal (linear) mixtures which are spectrally dominated by one component in a given wavelength region, a situation that occurs in many surface environments (Clark et al., 1991, 1992; Swayze, 2000).

In the course of this study, a spectral library was created that contains spectra representative of the major classes of natural materials on the Earth's surface with absorptions in the 0.4 - 2.5 μm range (Table 1). Mineral spectra were grouped into electronic or vibrational categories depending on the wavelength position of their dominant spectral absorption. Figure 2 shows spectra of some representative materials from the spectral library. Of particular interest are the chlorite, kaolinite, alunite, muscovite, and carbonate mineral groups. Compositional and structural variations between members of these mineral groups cause subtle shifts in wavelength position and changes in absorption-band shape that can be used to uniquely identify each member.

Table 1. Categories of materials in the spectral library used in this study.

no. spectra	Electronic absorption region	no. spectra	Vibrational absorption region
14	Grass, deciduous and conifer trees, Desert plants	4	Grass, dry grass, and conifer tree
1	Snow	1	Snow
9	Fe-oxides and Fe-hydroxides (Range of hematite grain sizes)	12	Na- and K-alunite and jarosite (Composition and temperature series)
4	Fe-sulfates and jarosite temperature series	6	Montmorillonite and muscovite (Compositional series)
4	Amorphous Fe-materials	4	Kaolinite group minerals
2	Desert varnish	2	Kaolinite/smectite
12	Amphiboles and pyroxenes	5	Amphiboles
3	Chlorite (Compositional series)	5	Chlorite (Compositional series)
3	Mn- and Cu-carbonates	6	Mn-, Ba- Fe-, Mg- and Ca-carbonates
2	Rare Earth oxides	11	Mineral mixtures
5	Weathered rocks	10	Other clays and micas
11	Other	7	Evaporites
		4	Ammonium-bearing minerals
		7	Other
70	Total	84	Total

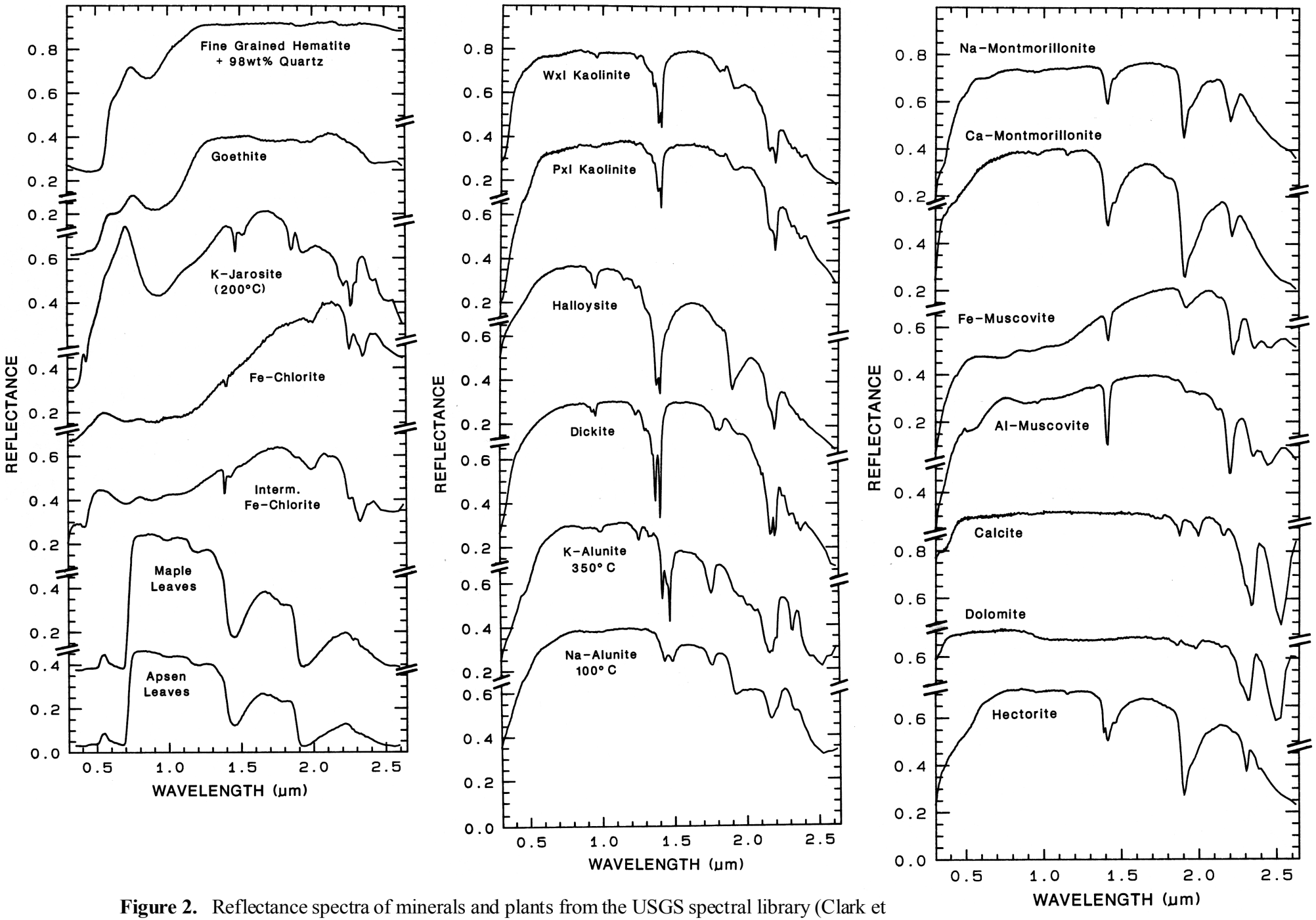

Figure 2. Reflectance spectra of minerals and plants from the USGS spectral library (Clark et al., 1993a). Interm. = intermediate; Wxl = well-crystallized; Pxl = poorly-crystallized.

3.2 Definition of Signal-to-Noise Ratio, Sampling Interval and Bandpass

Signal-to-noise ratio (S/N) is the mean signal level divided by one standard deviation of the fluctuations of the signal. Sampling interval (SI) is the spectral distance between the centers of adjacent spectral channels sampled along a spectrum (Figure 3). Bandpass (BP) is defined as the full-width at half maximum (FWHM) spectral response of a spectrometer channel to a monochromatic light.

In a grating imaging spectrometer, the SI is set by geometry only; specifically, the angular dispersion of the grating or prism, the focal length of the camera, and the pitch (or center-to-center spacing) of the detector elements. The BP may be affected by a combination of geometry, diffraction, and optical aberrations. Geometry includes the width of the entrance slit, width of the detector elements, angular dispersion, and spectrometer focal length. If geometry dominates and the entrance slit and detector width are equal, the result is a triangle-shaped spectral response for each detector. Diffraction and optical aberrations round out the corners of the triangle shape. Imaging spectrometers such as AVIRIS and VIMS have approximately Gaussian-shaped spectral response functions with BP approximately equal to the SI.

Figure 3 shows how changes in the sampling interval of a detector array can give rise to different types of sampling. Nyquist sampling occurs when BP = 2 SI and critical sampling occurs when BP = SI (e.g., Telford et al., 1976). Detector limited critical sampling occurs when the optical response bandwidth is narrower than the spectral width of the detector channels. In this case a wider wavelength swath of light is sampled by each detector element resulting in a flat topped BP that is comparable to the SI. Undersampling occurs when the BP and spectral width of the detector channels are narrower than the SI and gaps exist between adjacent detector elements. Oversampling occurs when the BP > 2 SI (not shown in Figure 3). To avoid confusion in this study the word "band" is reserved for describing spectral absorption features and is not used to describe spectral channels. Combinations of BP and SI are useful in describing the spectral response function of an imaging spectrometer. Some spectroscopists define spectral resolution as twice the BP at critical sampling and equal to the BP at Nyquist sampling. As most imaging spectrometers critically sample spectra, their spectral resolution would be twice their BP width by this definition. For more information on existing hyperspectral systems see Birk and McCord (1994), Clark (1999), and Kruse (1999).

3.3 How Signal-to-Noise Ratio, Sampling Interval, and Bandpass Interrelate

The highest S/N achievable in any given channel in an imaging spectrometer is limited by photon noise (N_{photon}) from the signal that is proportional to the square root of the number of photons converted to electrical signal for that channel. The actual S/N will be lower when other noise sources come into play, because the total noise (N_{total}) is the root-sum-square of all noise sources:

$$N_{total} = \sqrt{N_{photon}^2 + N_{other}^2} \quad (1)$$

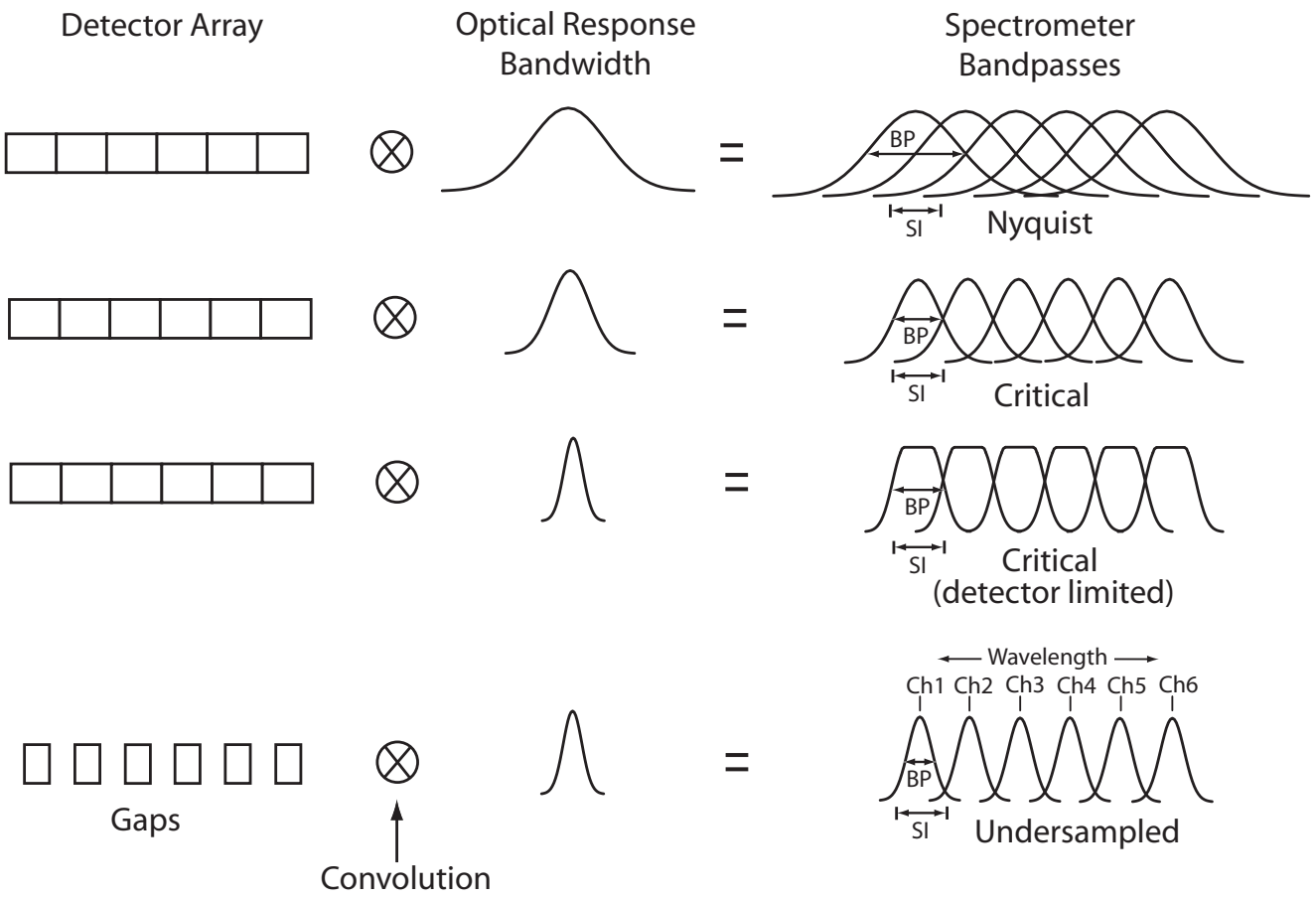

Figure 3. Definition of different types of spectral sampling in spectrometers. Nyquist sampling occurs when the bandpass (BP) is twice the sampling interval (SI). Critical sampling occurs when the BP and the SI are comparable. Detector limited critical sampling occurs when the optical response bandwidth is narrower than the spectral width of the detectors resulting in flat topped bandpasses. Undersampling occurs when the BP is less then the SI. The implication in undersampling is that light is being wasted between adjacent spectral channels. The spectrometer BP is the convolution of the optical response bandwidth and the spectral width of a detector.

therefore S/N will decrease when other noise (N_{other}) is non-zero. Other noise sources include fluctuations in detector dark current, readout-related noise, quantization noise, photon noise arising from thermal emission from the instrument, nonuniformity in the detector array and detector calibration issues. Additionally, mechanical vibrations may cause noise when observing a heterogenous scene.

In an array detector, the lower limit to the bandpass is set by the detector size and optical geometry. Consider a spectrometer whose throughput to the focal plane is constant with uniform light intensity and grating efficiency at all wavelengths. In such a system, broadening the BP by decreasing the resolution of the grating has no affect on signal, thus S/N is independent of BP but is dependent on SI when the SI is equal to the detector size. For example, changing the BP spreads the wavelengths of light falling on different detectors, but does not change the total light falling on the detectors. But if we double the number of detectors, each having half the spacing, then the light per detector correspondingly decreases. Thus, the number of detectors define the percentage of the incoming light seen by each detector, hence signal is proportional to the detector size and therefore to SI, as SI is inversely proportional to the number of detectors.

Because of the interdependence of S/N and SI, and spectral complexity of the features in spectra of surface materials, it is difficult to make general statements as to the optimal combination of these parameters in a spectrometer. Consequently, we have chosen to evaluate the effects of each parameter by modeling. Known spectra were convolved to different combinations of SI and BP, random noise was added, and an attempt was made to identify these spectra using a band-shape fitting algorithm (Clark et al., 2003). The advantage of such controlled modeling is that the correct answer is known with certainty, therefore algorithm performance and accuracy can be better understood.

3.4 Four Imaging Spectrometers

Idealized characteristics of four imaging spectrometers were selected to limit the number of cases tested to a reasonable range of spectrometer characteristics. Chosen for the simulations were: the Airborne Visible/Infrared Imaging Spectrometer (AVIRIS)(Vane et al., 1993; Chrien et al., 1995; Green et al., 1998); Hyperspectral Digital Imagery Collection Experiment (HYDICE) (Basedow et al., 1995); Multispectral Infrared and Visible Imaging Spectrometer (MIVIS) (Stanich and Osterwisch, 1994; Bianchi et al., 1994); and Visual Infrared Mapping Spectrometer (VIMS) (Miller et al., 1996; Brown et al., 2003). The first three are airborne instruments and the fourth is onboard the Cassini spacecraft on its way to study Saturn. AVIRIS sampling and bandpass parameters are for the 1994 flight season (written comm. R. Green); HYDICE parameters are for the preflight model (pers. comm., W. Farrand and W. Basedow); MIVIS parameters are for the 1994 flight season (written comm., K. More); VIMS parameters are for the preflight model (written comm., VIMS Team).

3.5 Why Use the USGS Tetracorder Algorithm?

The Tetracorder spectral analysis algorithm (Clark et al., 2003) was chosen for this study because it has been comparatively successful in identifying surface materials using imaging spectrometer data (Clark et al., 1991, 1992, 2001, 2003; Swayze et al., 1992, 2000, 2002;

Crowley, 1993; Crowley and Zimbelman,1997; King et al., 1995; Kokaly et al., 2003; Livo et al., 1999; McDougal et al., 1999; Dalton et al., 2000). It is one of the few algorithms currently in use for spectral identification and it has the flexibility to work over a wide range of applications, and is capable of simultaneously analyzing spectra of solids, liquids, and gases.

Tetracorder performs better in spectral identification than band ratio or band centewidth-depth algorithms because it uses information from the entire spectral feature, not just from a few channels (Clark et al., 2003). It integrates information from all the channels in a spectral feature, and because the S/N increases as the square root of the number of channels used in the match, it can work well on noisy data. Linear unmixing and neural-network identification schemes also integrate information from entire spectral features (or spectra) and these types of algorithms may give comparable results. Tetracorder differs from linear unmixing algorithms by using competition between library spectra to select the "best" spectral match, and it does not assume that all mixtures are linear (Clark et al., 2003).

Although spectra of pure materials were tested, we believe that the results of our study are broadly applicable to other investigations, which may involve analysis of spectral mixtures or use of identification algorithms other than Tetracorder, because of the unavoidable tradeoffs between BP, SI, and S/N, and because of the adverse effects of spectral aliasing. These are universal constraints encountered by all methods of spectral identification.

4.0 MODELING AND METHODS

In order to study when spectral absorptions from different materials can be confused, random noise was added to spectra of materials and Tetracorder's success rate of correctly identifying these materials, using their noisy spectra, was measured. The S/N at which Tetracorder achieved 50% and 90% success rates was determined for different BP and SI combinations. Figure 4 shows a flow chart of this process. Spectra of pure materials were used in all simulations because they allow the establishment of the coarsest spectral resolution and minimum S/N required to distinguish between these materials using reflectance spectra. Because modeling involves only pure phases and not the vast number of the mineral mixtures possible in nature, this study establishes upper limits for detectability using Tetracorder and the four spectrometer characteristics. Spectral identification of materials in intimate and areal mixtures will require higher S/N, narrower bandpasses, and finer sampling than for pure materials because of overlapping absorptions and weaker diluted bands. Yet, these simple test cases have practical value because spectral mapping has shown that many areas of the Earth's surface are spectrally dominated at any given wavelength by absorptions from one material (Clark et al., 2003). Spectra of 4 plants and 26 hydrothermal alteration minerals, called test spectra, were chosen to simulate spectral "unknowns" for matching to the entire spectral library. Table 2 lists general chemical formulas of the minerals.

At the time of modeling, the Tetracorder spectral library contained 154 spectra that spanned the range of natural surface materials including minerals, plants, and snow. These spectra were selected from the larger Clark et al. (1993a) spectral library which contains reflectance spectra for more than 480 individual samples representing 250 different materials.

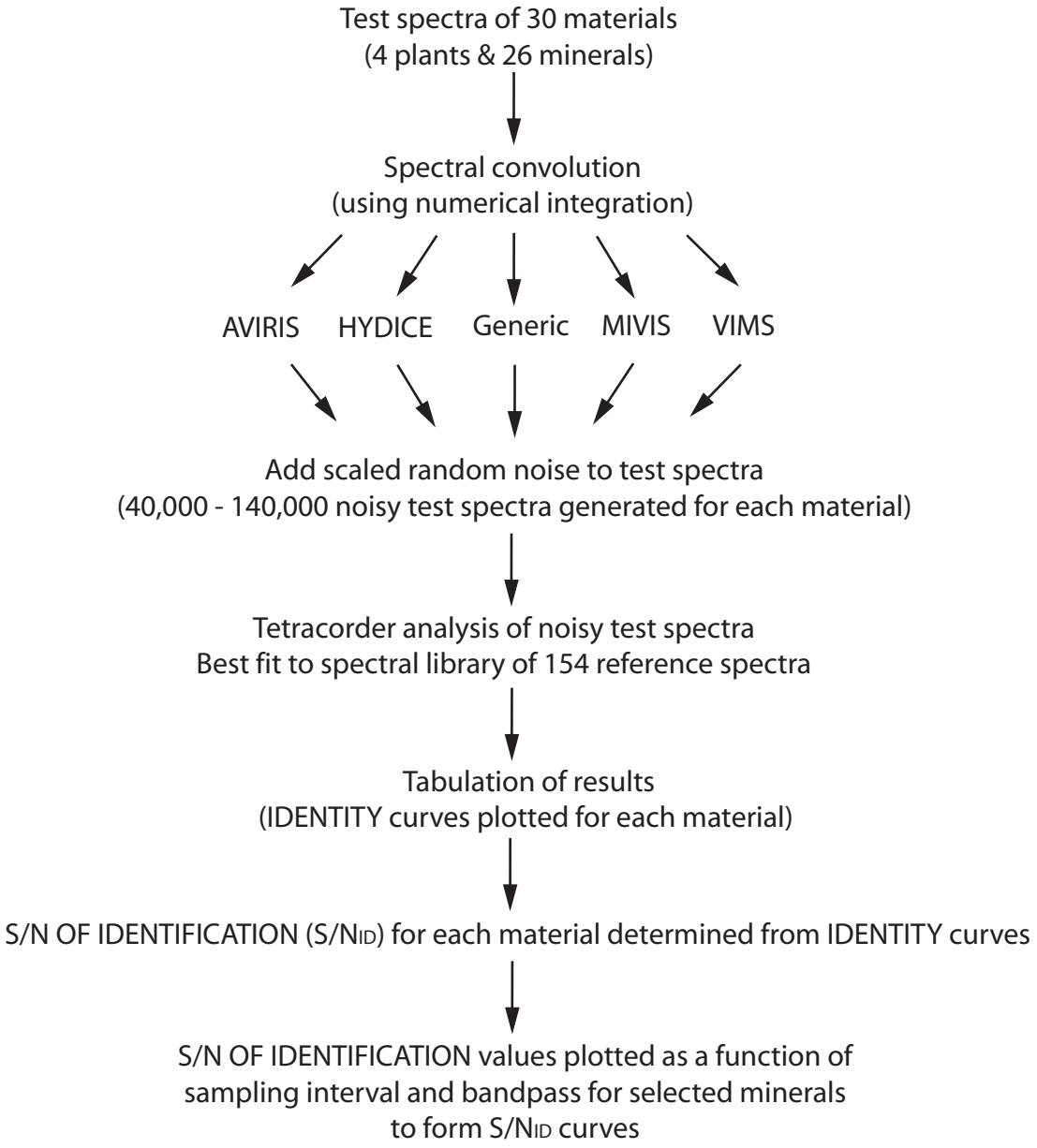

Figure 4. Steps involved in processing and spectral identification of test spectra to derive spectral identity curves and signal-to-noise of identification values.

Table 2. Chemistry of some minerals used in this study.

Alunite	$(K,Na)Al_3(SO_4)_2(OH)_6$
Calcite	$CaCO_3$
Chlorite	$(Mg,Fe^{2+})_5Al(Si_3Al)O_{10}(OH)_8$
Fe-Chlorite	$(Fe^{2+},Mg,Fe^{3+})_5Al(Si_3Al)O_{10}(OH,O)_8$
Dickite	$Al_2Si_2O_5(OH)_4$
Dolomite	$CaMg(CO_3)_2$
Goethite	$\alpha FeO(OH)$
Gypsum	$CaSO_4 \bullet 2H_2O$
Halloysite	$Al_2Si_2O_5(OH)_4$
Hectorite	$(Mg,Li)_3Si_4O_{10}(OH)_2Na_{0.3}(H_2O)_4$
Hematite	Fe_2O_3
Fe-Illite	$K(Al,Fe)_2(Si,Al)_4O_{10}[(OH)_2,H_2O]$
Jarosite	$(K,Na)Fe_3^{3+}(SO_4)_2(OH)_6$
Kaolinite	$Al_2Si_2O_5(OH)_4$
Montmorillonite	$(Na,Ca)_{0.33}(Al,Mg)_2Si_4O_{10}(OH)_2 \bullet nH_2O$
Al-Muscovite	$KAl_2(Si_3Al)O_{10}(OH)_2$
Fe-Muscovite	$K(Al,Fe^{3+})Fe^{2+}Si_4O_{10}(OH)_2$
Nontronite	$Na_{0.33}Fe_2^{3+}(Si,Al)_4O_{10} \bullet nH_2O$

*Formulas modified from Fleischer (1980)

The majority of these spectra were measured in bidirectional - hemispherical reflectance and corrected to absolute reflectance using a NIST traceable halon standard (Clark et al., 1990b). The remainder were measured in bidirectional reflectance on a Fourier Transform infrared spectrometer relative to a stainless steel mirror standard. Where applicable, samples were examined with X-ray diffraction, X-ray fluorescence, and electron microprobe analysis to establish mineral identity and purity. Electronic and vibrational absorption assignments for many minerals can be found in Hunt and Salisbury (1970, 1971), Hunt and Ashley (1979), Farmer (1974), and Clark et al. (1990b).

4.1 Spectral Convolution

The bandpass (BP) curves of the four imaging spectrometers are shown in Figure 5. For each spectrometer, the sampling interval (SI) is equal to or slightly narrower than the BP for each channel. Test spectra and Tetracorder library spectra were convolved to the sampling and bandpasses of these imaging instruments using a Gaussian-profile to approximate the actual spectral response functions of these sensors. Because the laboratory spectra do not have infinite spectral resolution, their convolution to the resolution of an imaging spectrometer can be approximated by integrating the area between their respective BP response curves.

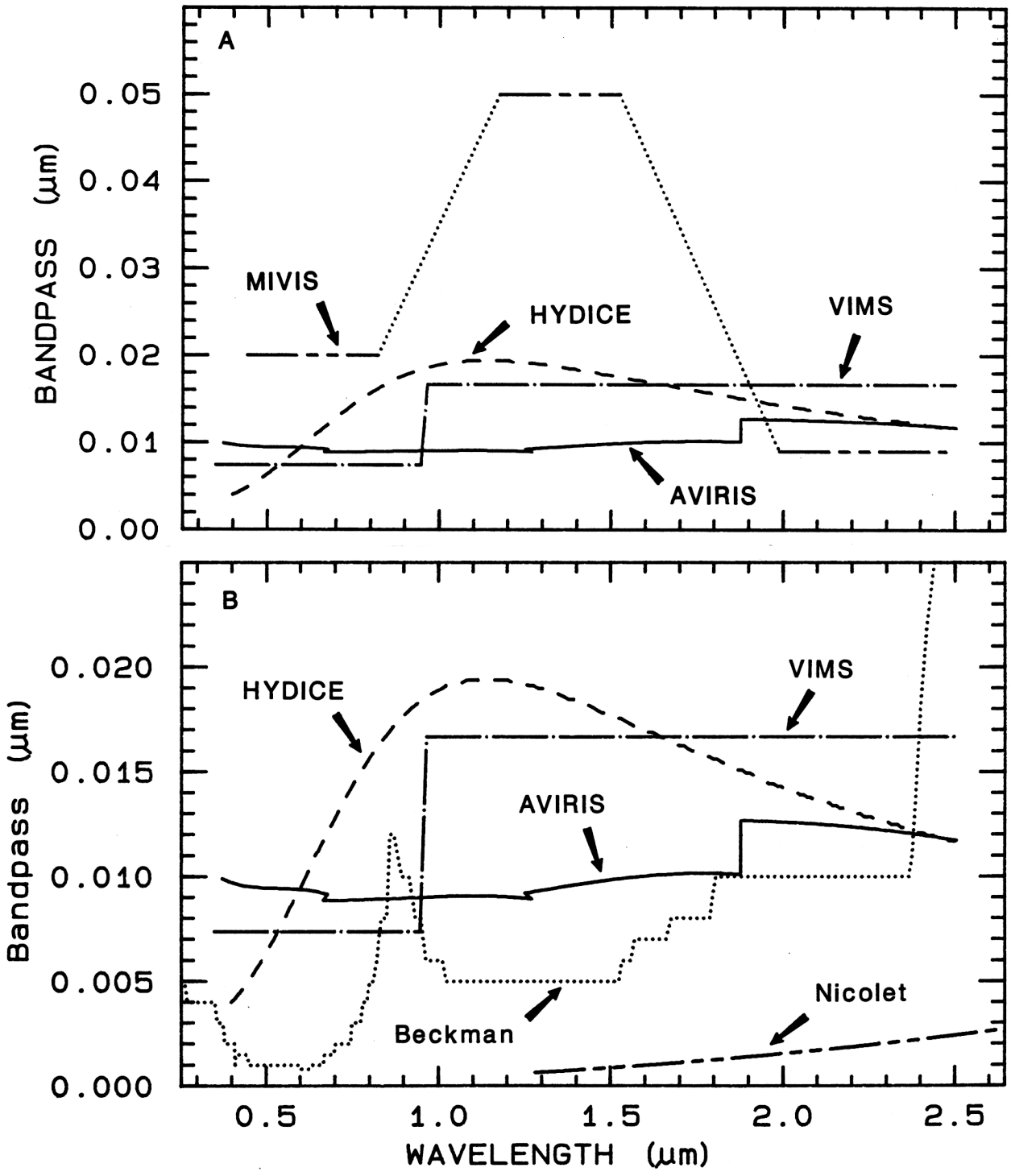

Figure 5. A) Spectral bandpasses of the AVIRIS, HYDICE, VIMS and MIVIS imaging spectrometers. All spectrometers except MIVIS have continuous spectral coverage from 0.4-2.5 μm (VIMS covers the range from 0.3-5.1 μm). MIVIS has no spectral coverage between 0.83-1.15 and 1.55-2.00 μm (gaps shown as dotted lines) but does have additional coverage from 8.2-12.7 μm which was not simulated in this study. B) Imaging spectrometer bandpasses compared to USGS Spectroscopy Laboratory Beckman and Nicolet spectrometer bandpasses.

Figure 6 shows two Gaussian-shaped profiles representing the laboratory (input) and imaging spectrometer (output) bandpass response curves. To calculate the reflectance of an output channel, the difference in area between the BP curves is first multiplied by the light source's irradiance profile (E), the optical and atmospheric transmittance (T), detector response (α), and the reflectance values of the input spectrum. For convenience, the first three terms can be represented by F where F = E T α. Next, the resulting value is added to the reflectance of the input spectrum times F at the output channel. To normalize the convolved output reflectance level, the resulting value, calculated above, is divided by the sum of a convolved spectrum whose reflectance values are all one and the value of F at the output channel. This process can be represented mathematically by:

$$R_j = \frac{F_j R_{kj} + \int_{\lambda_1}^{\lambda_n} F(\lambda) R_k(\lambda) \left(BP_j(\lambda) - BP_{kj}(\lambda) \right) d\lambda}{F_j + \int_{\lambda_1}^{\lambda_n} F(\lambda) \left(BP_j(\lambda) - BP_{kj}(\lambda) \right) d\lambda} \quad (2)$$

where R_j is the reflectance at channel j of the output spectrum, F_j is the value of F at channel j, R_{kj} is the reflectance value of the input spectrum at channel j, R_k is the reflectance of the input spectrum, BP_j is the spectral bandpass response curve of the output spectrum at channel j, BP_{kj} is the bandpass response curve of the input spectrum at channel j, and λ_n is the wavelength of the last channel of the input spectrum. If the F value is relatively constant over the wavelength range of BP_j and BP_{kj}, then its effects can be ignored. This calculation is done for each channel in the output spectrum. Because our spectral comparisons are made outside of the strong atmospheric absorptions and because our coarsest bandpass is only 31nm wide, we assumed F to be constant during our convolutions.

The integrals in Equation 2 are approximated using numerical integration which sums rectangular segments, where the width of each integration rectangle is defined by the wavelength interval between successive channels in the input spectrum. Spectral convolutions were done after the Beckman spectra were resampled by cubic splining to a SI several times narrower than that of the output spectra. This step increased the accuracy of the numerical integration during convolution. Nicolet spectra were already finely sampled and did not require cubic spline resampling. Convolution of well-crystallized kaolinite to the generic SI and BP values using Equation 2 was done using Nicolet spectra from 4 to 8 nm and Beckman spectra from 10 to 31 nm. The sampling increment was arbitrarily started at 0.4 μm and incremented without regard to the location of kaolinite's diagnostic absorptions. The same was done for convolution of goethite, hematite, K-jarosite, K-alunite, calcite, and Na-montmorillonite to generic SI and BP using Beckman spectra from 10 to 31 nm.

The Beckman spectra have finer sampling and bandpasses then the imaging instruments,

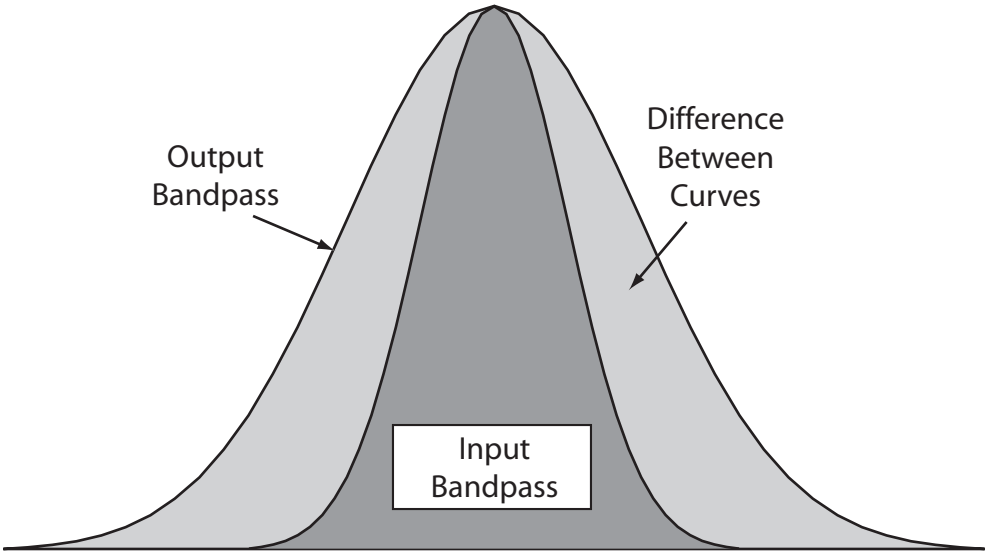

Figure 6. During spectral convolution the difference in area between input and output spectrometer bandpasses is represented by the integrals in Equation 2.

except from 0.85 - 0.91 μm and 2.39 - 2.5 μm where the Beckman spectrometer has BP and SI values as broad as 12 nm at 0.85 μm and > 13 nm beyond 2.39 μm (Figure 5B). Because library spectra have only broad spectral features in the 0.85-μm region, their convolution to imaging instruments with narrower sampling and bandpasses than those of the Beckman spectrometer (e.g., AVIRIS and VIMS) will not introduce significant errors. However, convolution of Beckman spectra to the imaging instruments does result in a slight broadening of spectral features beyond 2.39 μm. All features used for modeling in this study are located at shorter wavelengths. The Nicolet spectra were measured at narrow sampling and bandpass values and their convolution to the imaging instruments is accurate at all wavelengths. Figure 7 shows a spectrum of well-crystallized kaolinite convolved to the bandpasses and sampling intervals of the imaging spectrometers. Subtle differences in the 2.2-μm kaolinite doublet provide the basis for differentiation of this mineral from other kaolinite group minerals (see Figure 2). The most notable differences are in the 1.4-μm region which is concealed, for the most part, from terrestrial sensors by atmospheric water vapor.

4.2 Atmospheric and Vegetative Interferences

In terrestrial remote sensing, spectral features of surface materials that coincide with strong atmospheric absorptions cannot be measured by imaging spectrometers due to atmospheric attenuation of the light signal. Figure 8 shows a synthetic transmission spectrum of the Earth's atmosphere. The 1.4- and 1.9-μm regions have very strong atmospheric water vapor absorptions that obscure diagnostic surface absorptions in remotely sensed images (compare Figures 2 and 8). In this study we avoided using spectral features which coincide with these atmospheric absorptions to better simulate conditions experienced by terrestrial imaging spectrometers. Additional water vapor absorptions at 0.92 and 1.12 μm are weak and their spectral signature can be modeled well enough to be removed so that these spectral regions can be used in our simulations. We avoided using spectral absorptions near 0.69-μm during Tetracorder analysis of the test spectra because this wavelength region coincides with the strong chlorophyll absorption of vegetation. A trace of vegetation, otherwise undetectable, can mimic the 0.69-μm absorptions in Fe-bearing minerals thus increasing the number of misidentifications. For some extraterrestrial applications there will be no atmospheric absorptions, therefore, useful surficial spectral information may be collected at all wavelengths. This additional information may lead to better identification than is possible when atmospheric absorptions obscure the surface at critical wavelengths.

4.3 Addition of Random Noise to the Test Spectra

In order to simulate the effects of variable S/N on the identification process, we added scaled random noise, with a Gaussian distribution about a zero mean, to each convolved test spectrum. We used "drand48" to generate the random numbers (HP-UX 9.0). Signal-to-noise ratio is here defined for a surface of 50% reflectance, a standard commonly used in reflectance studies, where the reflectance level is divided by the standard deviation of the Gaussian noise spectrum, with standard deviation uniform at all wavelengths. In order to simulate the performance of the sensors, the level of noise added to each test spectrum was defined for a uniform 50% reflectance surface, even though the spectrum receiving the noise may have had a reflectance level higher or lower than 50%. This process can be represented mathematically as:

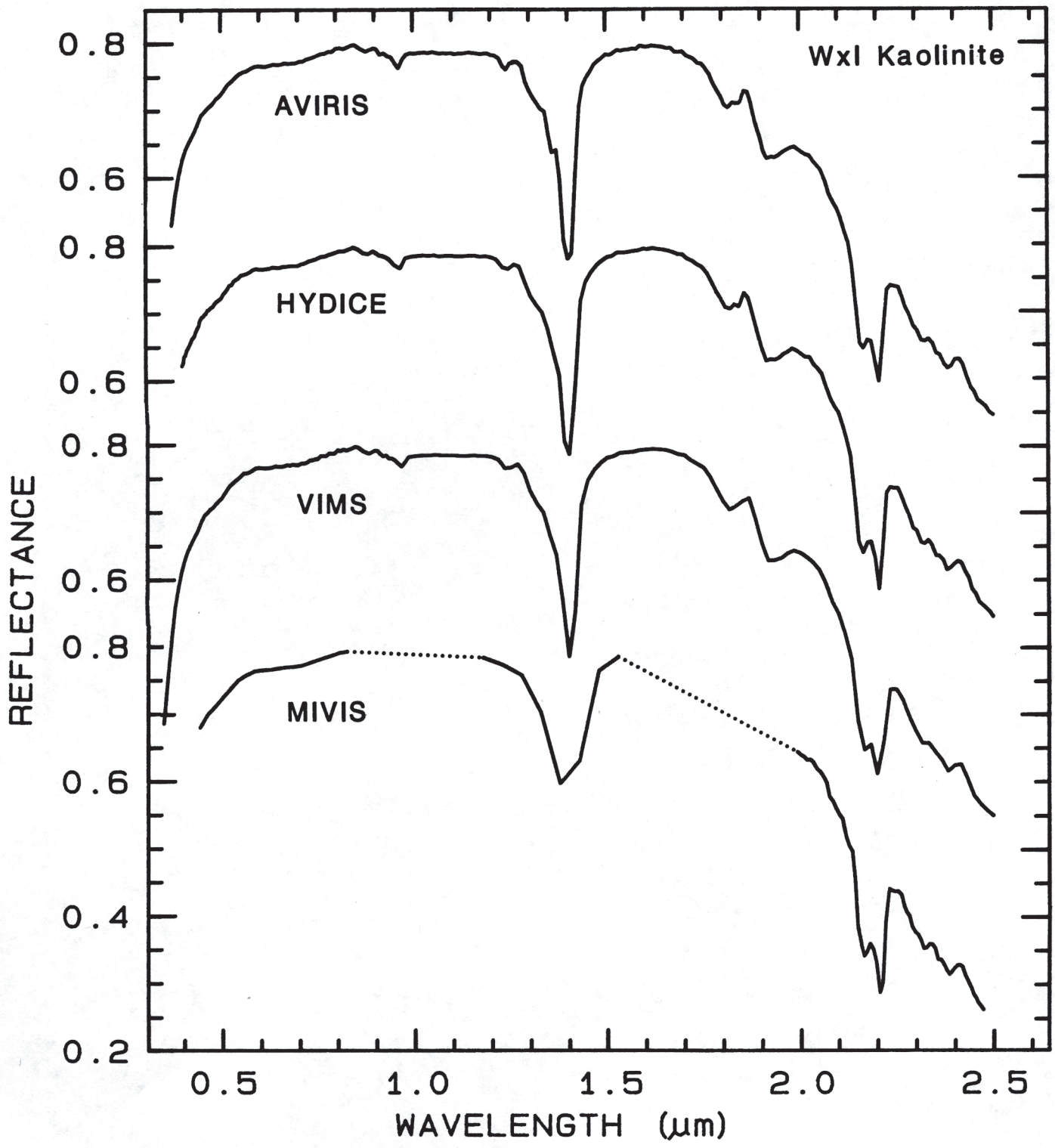

Figure 7. Reflectance spectra of a well-crystallized kaolinite convolved to AVIRIS, HYDICE, VIMS, and MIVIS resolution. Dotted lines in the bottom spectrum represent wavelengths regions where spectral data is not collected by the MIVIS instrument.

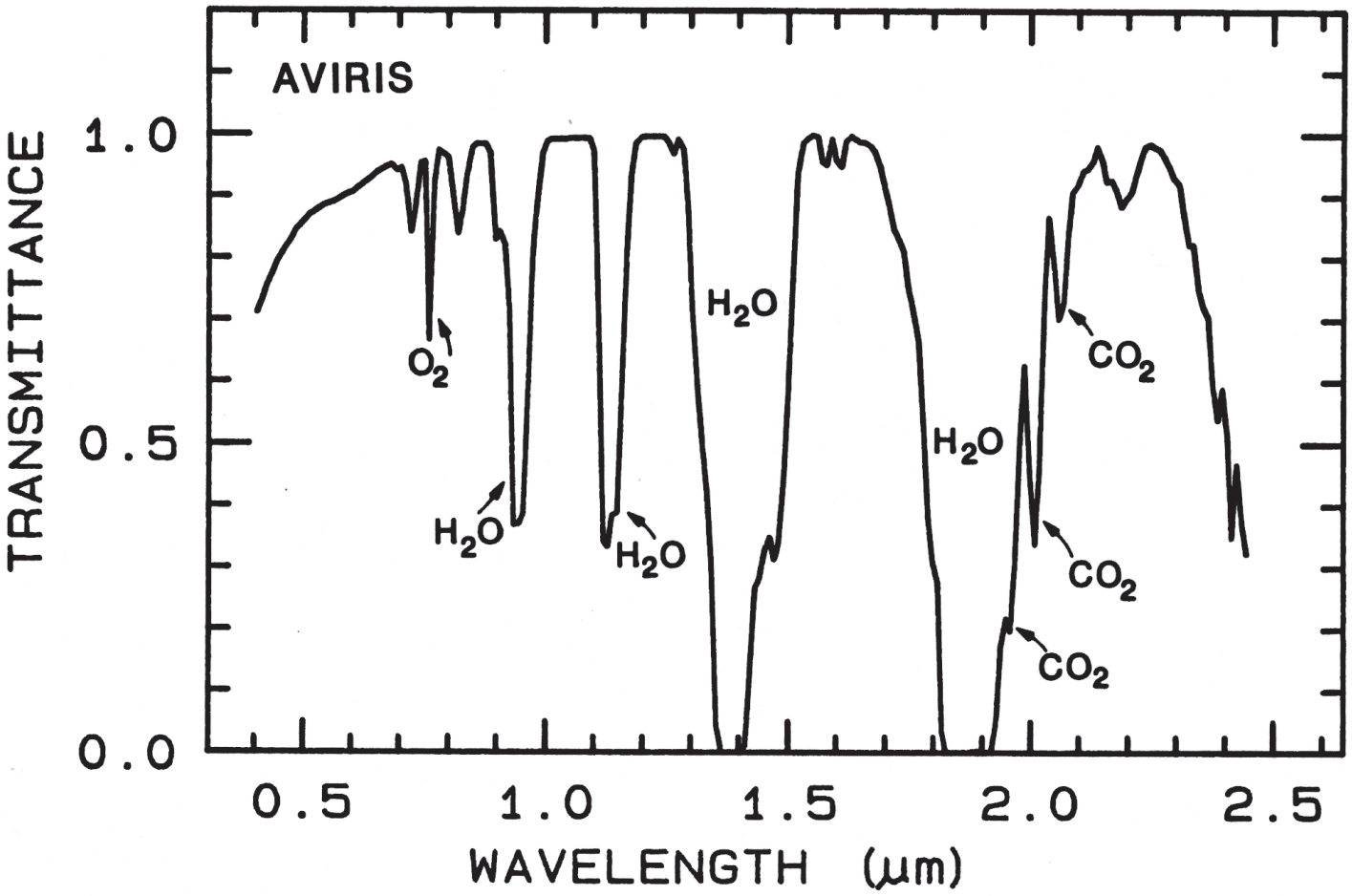

Figure 8. Transmission spectrum of the Earth's atmosphere at AVIRIS resolution calculated using the LOWTRAN atmospheric modeling program (Kneizys et al., 1989). Model uses a single path (top of atmosphere to surface) with mid-latitude summer sun and atmospheric conditions. Terrestrial atmospheric H_2O absorptions are frequently strong enough to conceal surface absorptions at 1.4 and 1.9 μm preventing these spectral regions from being used to map materials at the surface.

$$R_n(\lambda) = R_t(\lambda) + N(\lambda) \qquad S/N_{N(\lambda)} = \frac{R_{50\%}(\lambda)}{\sigma_{N(\lambda)}} \tag{3}$$

where $R_n(\lambda)$ is the test spectrum with added noise, $R_t(\lambda)$ is the test spectrum, $N(\lambda)$ is the noise spectrum, $S/N_{N(\lambda)}$ is the S/N of the noise spectrum, $R_{50\%}(\lambda)$ is a spectrum with uniform 50% reflectance, and $\sigma_{N(\lambda)}$ is the standard deviation of the noise spectrum. Random noise spectra added to test spectra had S/N levels that spanned the ranged from 1 to 500. Figure 9 shows spectra of kaolinite, at AVIRIS resolution, with various levels of added noise. Recognition of the kaolinite doublet at 2.2 μm is difficult at S/N less than 10.

4.4 The Tetracorder Algorithm

The Tetracorder algorithm (Clark et al., 1990a; Clark et al., 2003) uses a modified least-squares band-shape fitting technique to identify materials spectrally and create maps of their distribution. The primary algorithm works by scaling a library spectrum to an observed spectrum, in this case a convolved test spectrum with noise added to simulate an imaging spectrometer spectrum, using the modified least-squares solution to derive a numerical value called Fit. The algorithm derives Fits for all of the spectra in its library and selects the material with the highest Fit as the best spectral match. Comparisons are done only in the wavelength regions of diagnostic absorptions. In most cases Tetracorder identifies the spectrally-dominant material in each spectral region whether (e.g., electronic and vibrational), but it is capable of identifying mixtures if representative spectra of those mixtures are added to its library. Eleven mineral mixtures were included in the spectral library used by Tetracorder for this study. When Tetracorder identifies a material as spectrally dominant that material does not have to be pure, it can also be intimately or areally mixed with other phases. Spectral dominance means the diagnostic absorptions of that material are the strongest features in a given spectral region and are not obscured beyond recognition by absorptions from other phases. If the highest Fit falls below a threshold then "No Match" is found and the observed spectrum is not unidentified. See Clark et al. (2003) for a more detailed discussion.

4.5 Identification as a Function of Signal-To-Noise Ratio

One method of determining the S/N at which a spectrum can be identified as belonging to a specific material, to a given degree of accuracy, involves adding noise to test spectra at known S/N levels and then running these noisy test spectra through Tetracorder and tabulating the results of the identifications. This was done for 30 test spectra convolved to AVIRIS spectral resolution and 7 test spectra convolved to the spectral resolution of the other three spectrometers. More simulations were done for AVIRIS because we had actual imaging data with which to check the accuracy of our predictions in greater detail than was possible for the other spectrometers.

For statistical accuracy, variable numbers of noisy test spectra were generated at each S/N level for each convolved test spectrum. High S/N values required only 400 noisy test spectra,

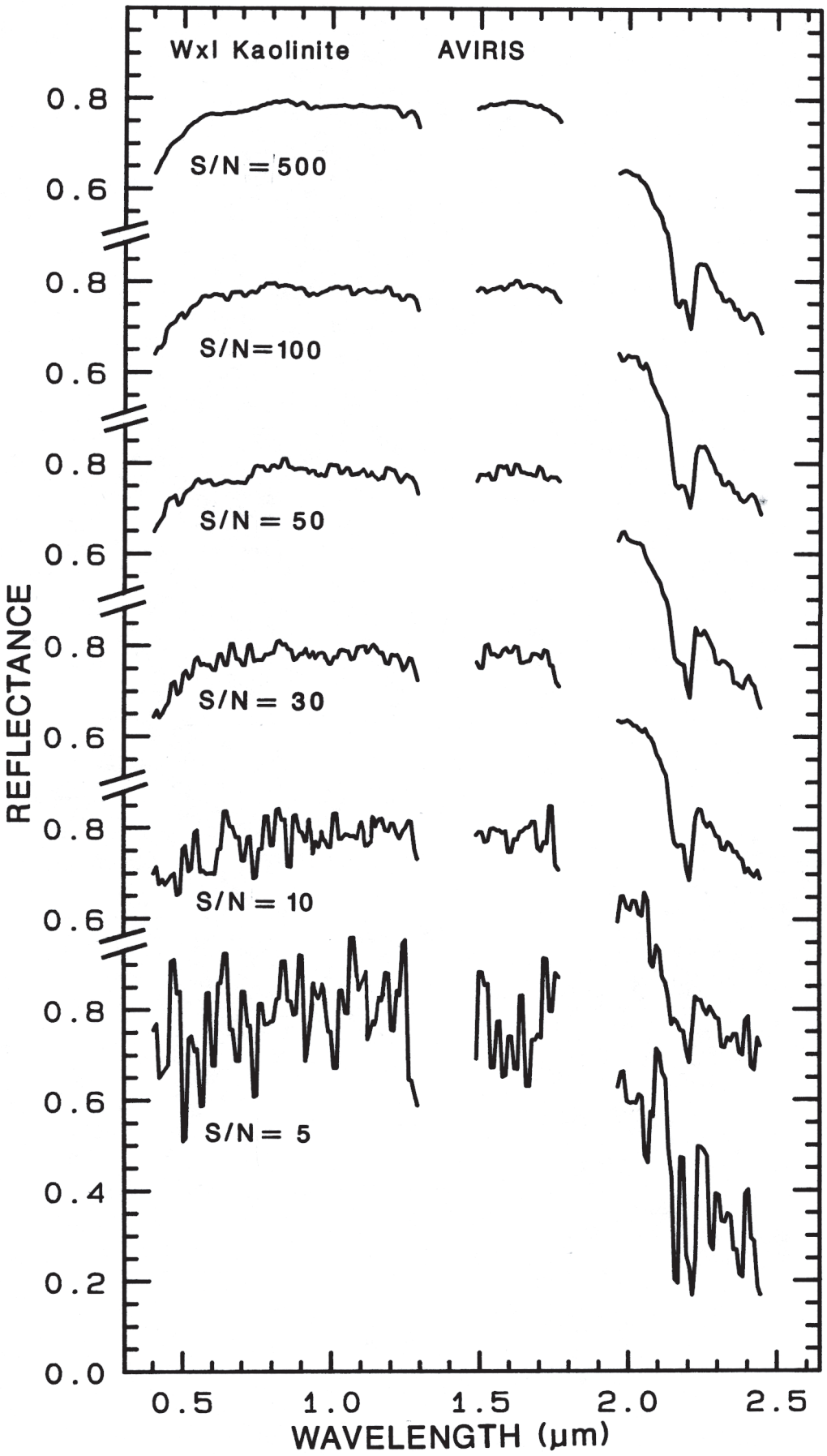

Figure 9. Laboratory spectrum of kaolinite convolved to AVIRIS resolution with various levels of random noise added. Signal-to-noise ratio is defined here as fifty percent reflectance divided by the standard deviation of the Gaussian noise, with the standard deviation of the noise at a constant level at all wavelengths over the entire spectrum.

while low S/N values required as many as 9,000 noisy test spectra to calculate the percentage of spectra correctly identified with an acceptable degree of precision. Between 40,000 and 140,000 noisy test spectra were evaluated by Tetracorder to construct each identity curve and more than 40 million spectra were evaluated for this study. Figure 10A shows the identity curve for calcite at AVIRIS resolution. Figure 10B shows the corresponding receiver operating characteristic (ROC) curves (Metz, 1978) which plot the correct identification (true positive rate) against the incorrect identification (false positive rate) for spectral identification of the noisy calcite test spectra. Tetracorder has little difficulty identifying the noisy test spectra as calcite at or above the 50% correct level until the S/N is less than 27 because the 2.34-μm calcite absorption is broad and its wavelength position distinct compared to other materials in the spectral library, and unlike unmixing algorithms, Tetracorder is not forced to make a spectral match (Clark et al., 2003). The signal-to-noise of identification (S/N_{ID}) is defined as the S/N at which a given percentage of noisy test spectra are correctly identified by Tetracorder. Tetracorder never has an incorrect identification rate above 10% for calcite, even as S/N drops to zero (Figure 10A). The next section explains why the 50% and 90% correct levels were chosen as standards for this study.

4.6 Choosing Confidence Levels

Most pattern recognition studies have dealt with recognizing absorption shapes in spectra of individual pixels (Swain, 1978). These studies have used statistical analyses of n-dimensional vector space to create decision surfaces around naturally clustered data for use in supervised and unsupervised classifications. Tetracorder performs this classification task, producing images of the spatial distribution of each detected material. The next step is pattern recognition of pixel clusters in the image. Because the accuracy of identification can be strongly influenced by the S/N of the spectral data, the potential for misidentifications increases as S/N decreases. Misidentified pixels will tend to add noise to images, sometimes obscuring meaningful surface patterns. This noise can be reduced by mathematically identifying areas in each image where the pixels of a diagnostic material are dense enough to form recognizable patterns such as those of rock outcrops, plant communities, and urban structures, to name a few. For this task, a clustering algorithm was developed that calculates the density of neighboring illuminated pixels as a function of distance from an illuminated pixel for each material image. Values are tabulated for each illuminated pixel in the image for successively longer distances to illuminated neighboring pixels. High densities sustained over long distances indicate a significantly large cluster of pixels. Threshold values indicating levels of significance were derived by comparing how well maps of surface materials matched geologic outcrop maps. Using this algorithm, images with significant pixel clusters can be automatically tagged for follow up investigation.

The pattern recognition algorithm can also be used to better understand the importance of identity curves for remote sensing. It can be used to evaluate quantitatively the degree of accuracy necessary to recognize spatial patterns using synthetic mineral maps. This can be accomplished by measuring the proportions of calcite, dolomite, epidote, “Other”, and “No Match” identified at the 15, 30, 50, 70, and 90% correct levels of the calcite identity curve (Figure 11). Figure 12 shows noisy synthetic composite images, where for each correct level the percentage of colored pixels represents the proportion of test spectra identified by Tetracorder as

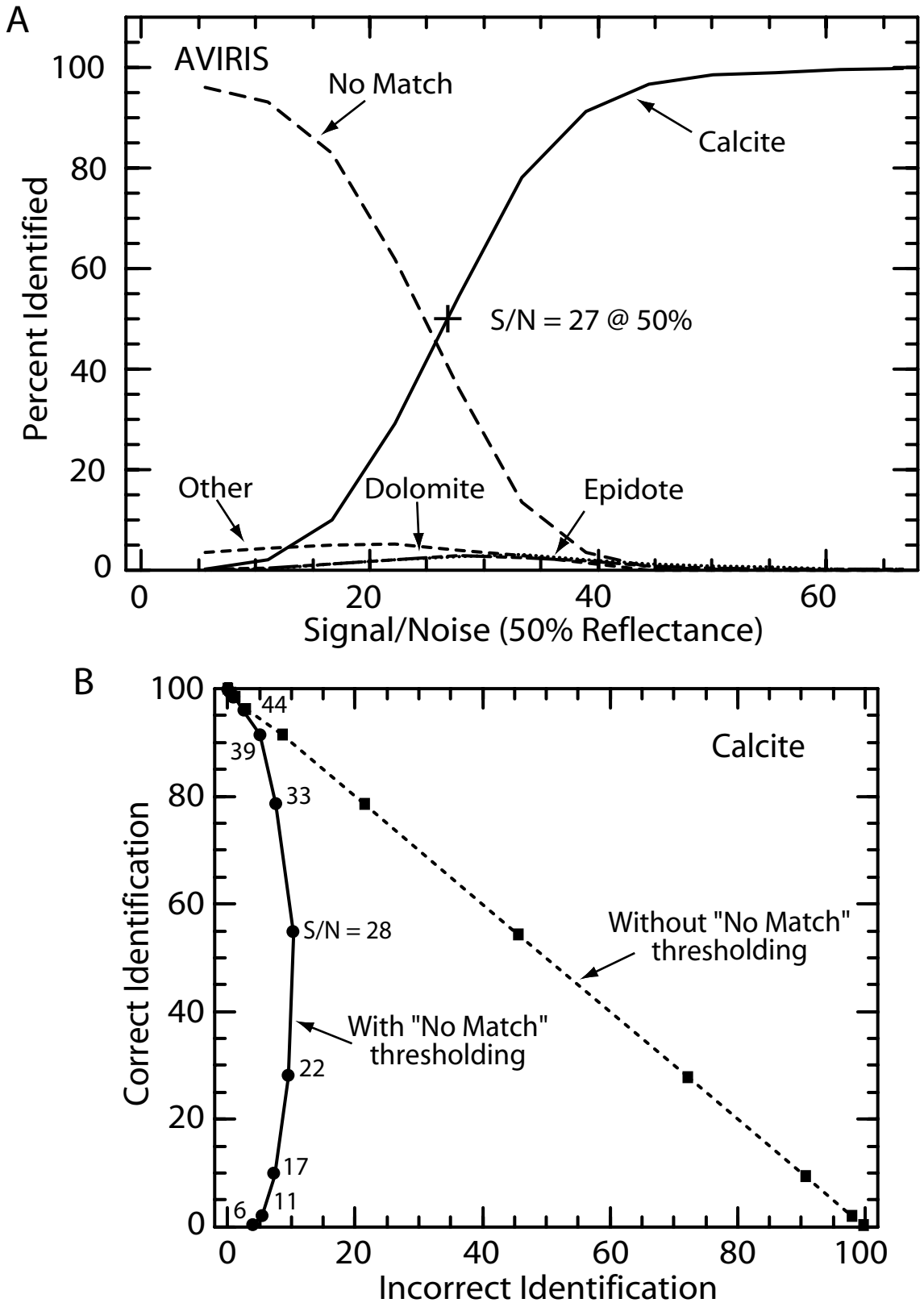

Figure 10. A) Percentage of noisy calcite test spectra correctly identified by Tetracorder as a function of signal-to-noise ratio (S/N) at AVIRIS spectral resolution. This is the calcite identity curve. The curves labeled dolomite and epidote give the percentage of noisy calcite spectra misidentified as those of dolomite and epidote respectively. "Other" refers to the percentage of spectra misidentified as those of materials other than dolomite and epidote. "No Match" refers to the percentage of spectra with Fit, Depth, or Fit*Depth values which fell below Tetracorder thresholds. Fifty percent of the noisy test spectra were correctly identified as calcite at a S/N of 27. The S/N values are for a 50% reflectance surface. B) Receiver operating characteristic curve for noisy calcite test spectra. Numbers next to circles are the S/N values of the test spectra and also apply to the corresponding squares. Most test spectra are incorrectly identified at low S/N (dashed curve) but with the "No Match" threshold activated (solid curve) the number of test spectra incorrectly identified decreases substantially.

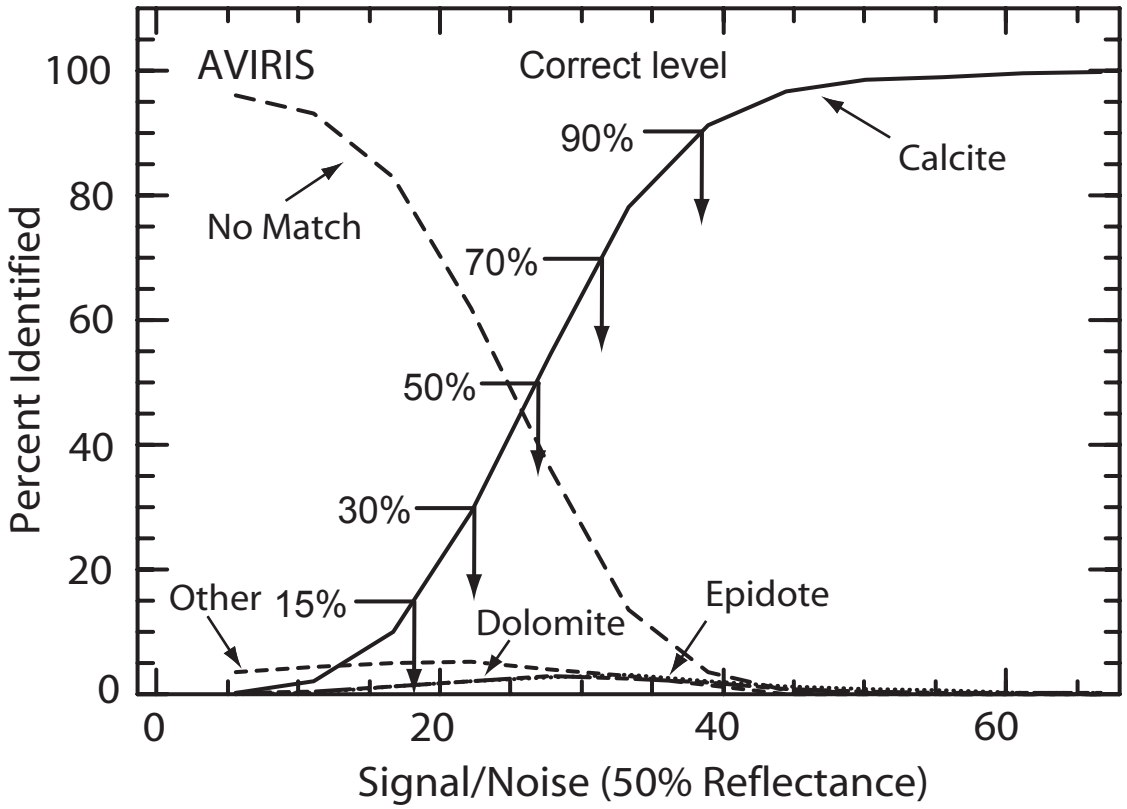

Figure 11. Identity curve for calcite at AVIRIS spectral resolution (Figure 10A). Arrows indicate the signal-to-noise of identification (S/N_{ID}) values (on the Signal / Noise axis) at the 15, 30, 50, 70, and 90% correct levels. The proportion of calcite, dolomite, epidote, "Other", and "No Match" identifications can be calculated for each S/N_{ID} value using this diagram.

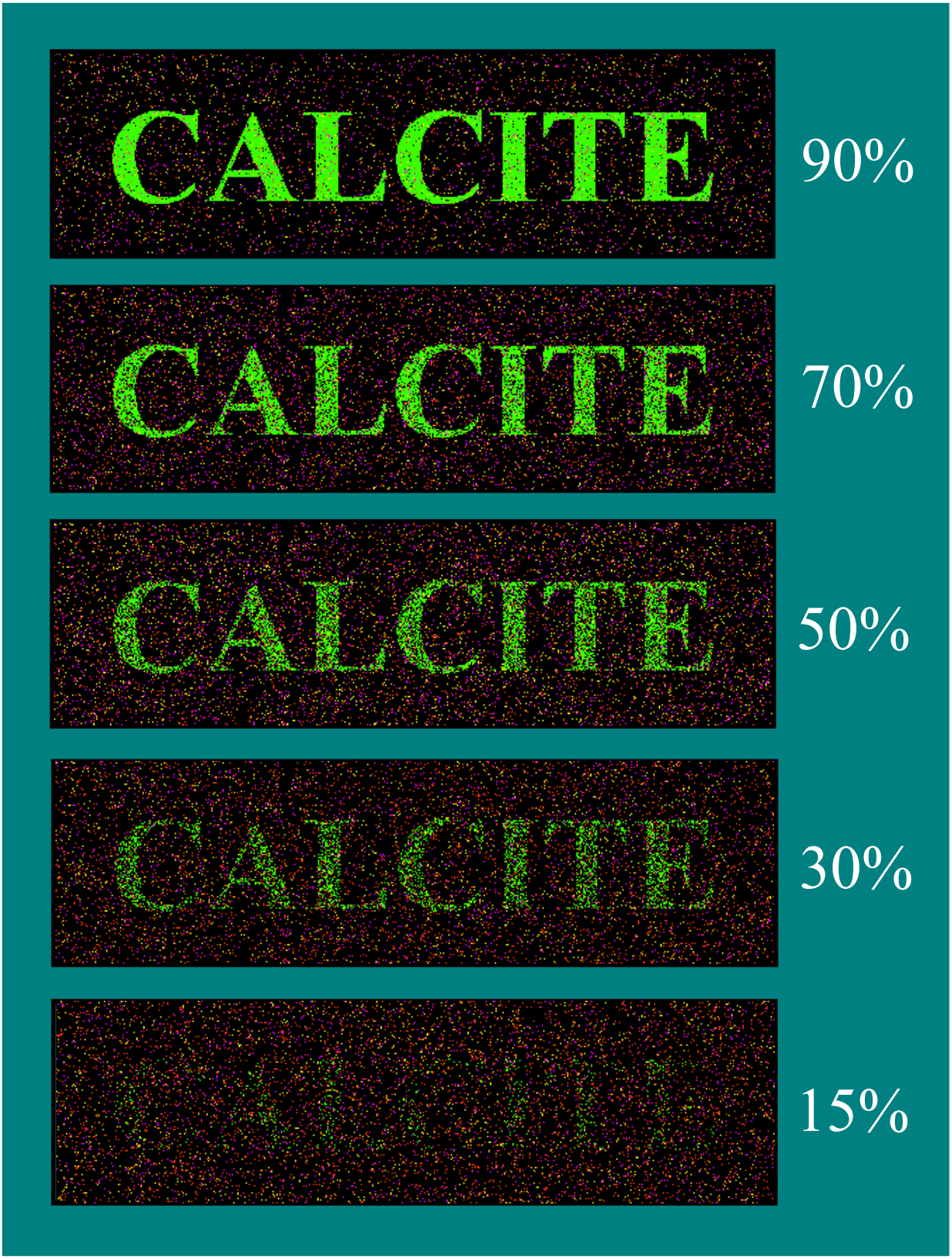

Figure 12. Synthetic color composite images based on the spectral identity curve for calcite (Figure 11) showing the effects of signal-to-noise ratio on the ability to correctly identify materials and recognize distribution patterns. The percentage of colored pixels in each image correspond to the proportion of calcite (green), dolomite (yellow), epidote (magenta), "Other" (red), and "No Match" (black) identified by Tetracorder using noisy calcite test spectra at the 15, 30, 50, 70, and 90 % correct levels. To create a cluster of pixels (e.g., a pattern similar to a geologic outcrop) as would be seen in noisy imaging spectrometer data all green calcite pixels were made black except in the letters of the word "calcite."

calcite, dolomite, epidote, "Other," and "No Match." When the clustering algorithm was run on these images, it recognized a significant pattern in the 50%, 70%, and 90% level images, but only a tentative pattern in both the 15% and 30% level images. A significant spatial pattern can still be recognized visually, even at the 50% correct level. This is due to binning of incorrectly identified pixels into more than one mineral category, allowing correctly identified pixels to dominate the composite image. The 50% correct level is minimally adequate for recognizing large patterns such as rock outcrops and plant communities, however, the 90% correct level produces much clearer patterns and S/N levels allowing this degree of accuracy should be the goal of future spectrometers. Nevertheless, because the 50% level intersects the steep part of the identity curve (Figure 11), it can be used to determine corresponding values of S/N_{ID} more accurately than can higher correct levels, which intersect the identity curves where they are flatter. Therefore, the 50% correct level was adopted to facilitate comparisons between identity curves in this study. We believe these findings are generally applicable to pattern recognition regardless of the method used for spectral identification.

4.7 Standardizing Band Depths and Continuum Levels

Natural variations in band depths and continuum levels of diagnostic absorptions in each of the 26 mineral test spectra make the S/N_{ID} derived for each mineral unique to that particular sample. Even though the overall spectral shape is similar for different samples of the same mineral, grain size variations influence the strength of absorption features and continuum levels for each sample. As a result the initially derived S/N_{ID} values were sample dependent. To minimize the effects of grain-size variations the initial S/N_{ID} values were adjusted to reflect a sample with a spectrum having a main absorption band depth of 10% and continuum level of 50% reflectance critically sampled with a BP and SI = 10nm. For materials with electronic absorptions, the main band occurs near 1.0 μm, and for materials with vibrational absorptions, the main band is the strongest absorption between 2.1 - 2.4 μm.

5.0 RESULTS

5.1 Spectral Lessons

As can be seen in Figure 2, spectra of the kaolinite group minerals differ only in the relative strength of the first band of the 2.2-μm absorption doublet and slightly longer wavelength position and narrower width of the first of the doublet bands in dickite (when ignoring the 1.4-μm bands). Figure 13 shows the identity and ROC curves for well-crystallized (wxl) kaolinite at AVIRIS spectral resolution. When random noise is added, the wxl kaolinite test spectra are sometimes confused with those of poorly-crystallized (pxl) kaolinite and to a lesser extent dickite and halloysite. However, confusion with spectra of the other 80 materials in the vibrational absorption library is relatively insignificant as indicated by the low value of the "Other" curve. Fifty percent of the test kaolinite spectra were correctly identified by Tetracorder at a S/N = 37.

Although wxl kaolinite has a subordinate 2.34-μm absorption (Figure 14), as do all of the kaolinite group minerals (Figure 2), using these absorptions in the Tetracorder analysis actually impedes spectral identification. Figure 15 shows the identity and ROC curves for wxl kaolinite with and without use of the 2.34-μm absorption. The S/N required for 50% correct identification

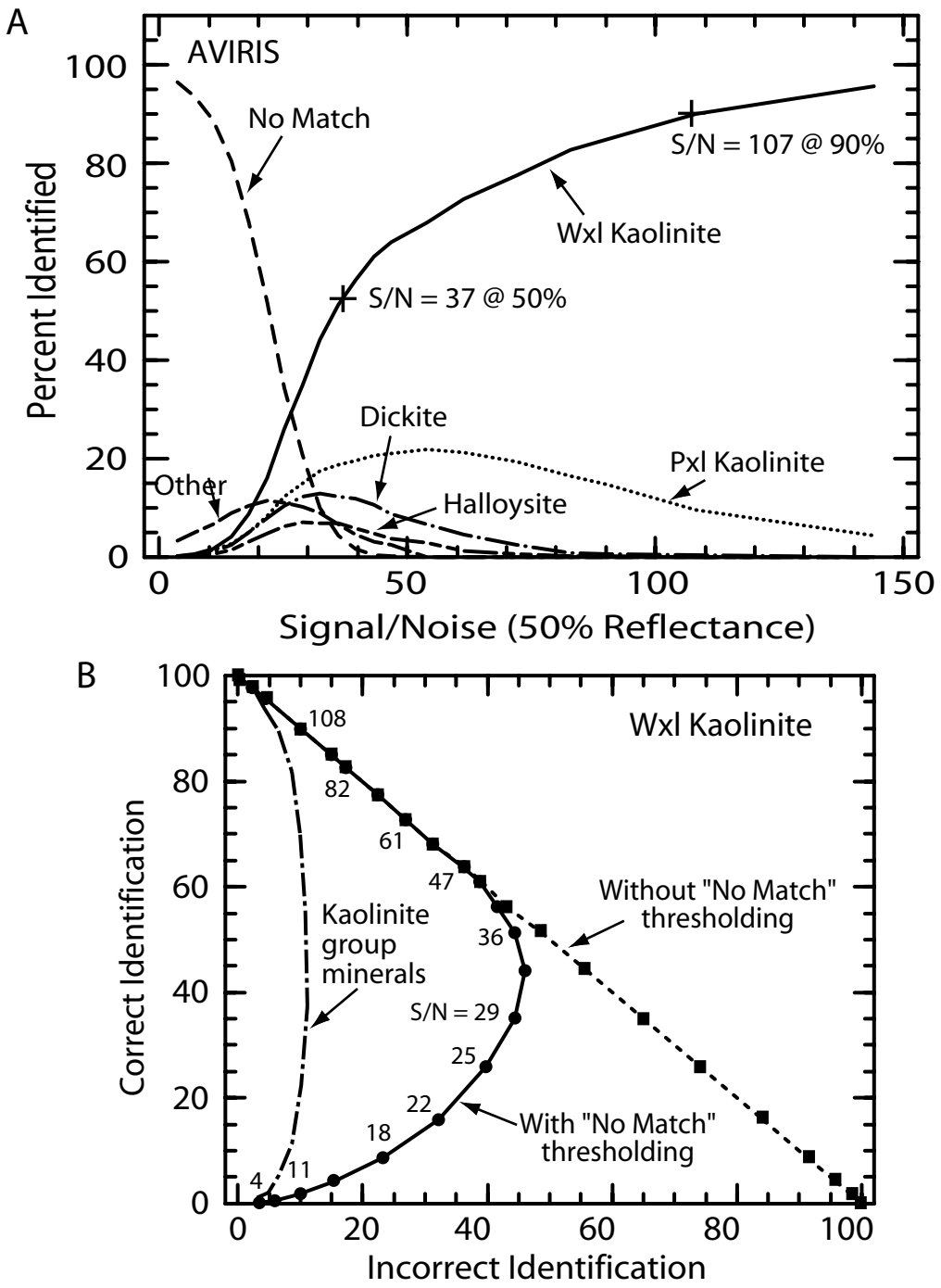

Figure 13. A) Percentage of noisy well-crystallized (wxl) kaolinite test spectra correctly identified by Tetracorder as a function of signal-to-noise ratio (S/N) at AVIRIS spectral resolution. This is the wxl kaolinite identity curve. The curves labeled dickite, halloysite, and poorly-crystallized (pxl) kaolinite give the percentage of spectra misidentified as those minerals. "Other" refers to the percentage of spectra misidentified as those of materials other than dickite, halloysite, and pxl kaolinite. "No Match" refers to the percentage of spectra with Fit, Depth, or Fit*Depth values which fell below Tetracorder thresholds. The other three spectrometers have similar curves. Fifty percent of the noisy kaolinite test spectra were correctly identified by Tetracorder at a S/N of 37; ninety percent were correctly identified at a S/N of 107. B) Receiver operating characteristic curve for noisy wxl kaolinite test spectra. Numbers next to circles are the S/N values of the test spectra and also apply to the corresponding squares. Most test spectra are incorrectly identified at low S/N (dashed curve) but with the "No Match" threshold activated (solid curve) the number of test spectra incorrectly identified decreases substantially. Dash-dot curve lumps the other kaolinite group minerals (e.g. pxl kaolinite, dickite, and halloysite) with wxl kaolinite to show that most of the incorrect identifications are due to confusion with these spectrally similar minerals.

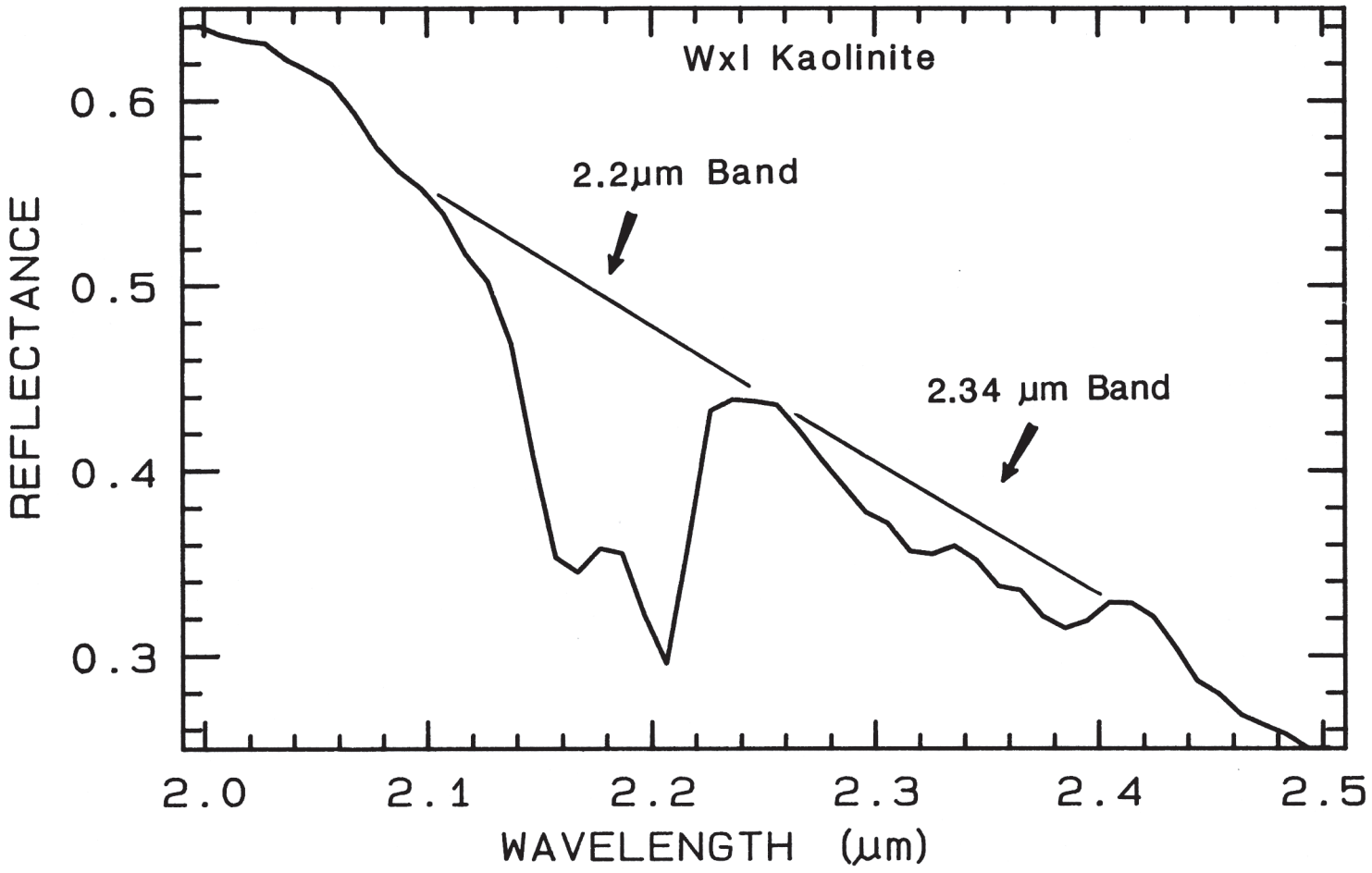

Figure 14. Reflectance spectrum of well-crystallized kaolinite showing details of the 2.2- and 2.34-µm absorptions and their continua.

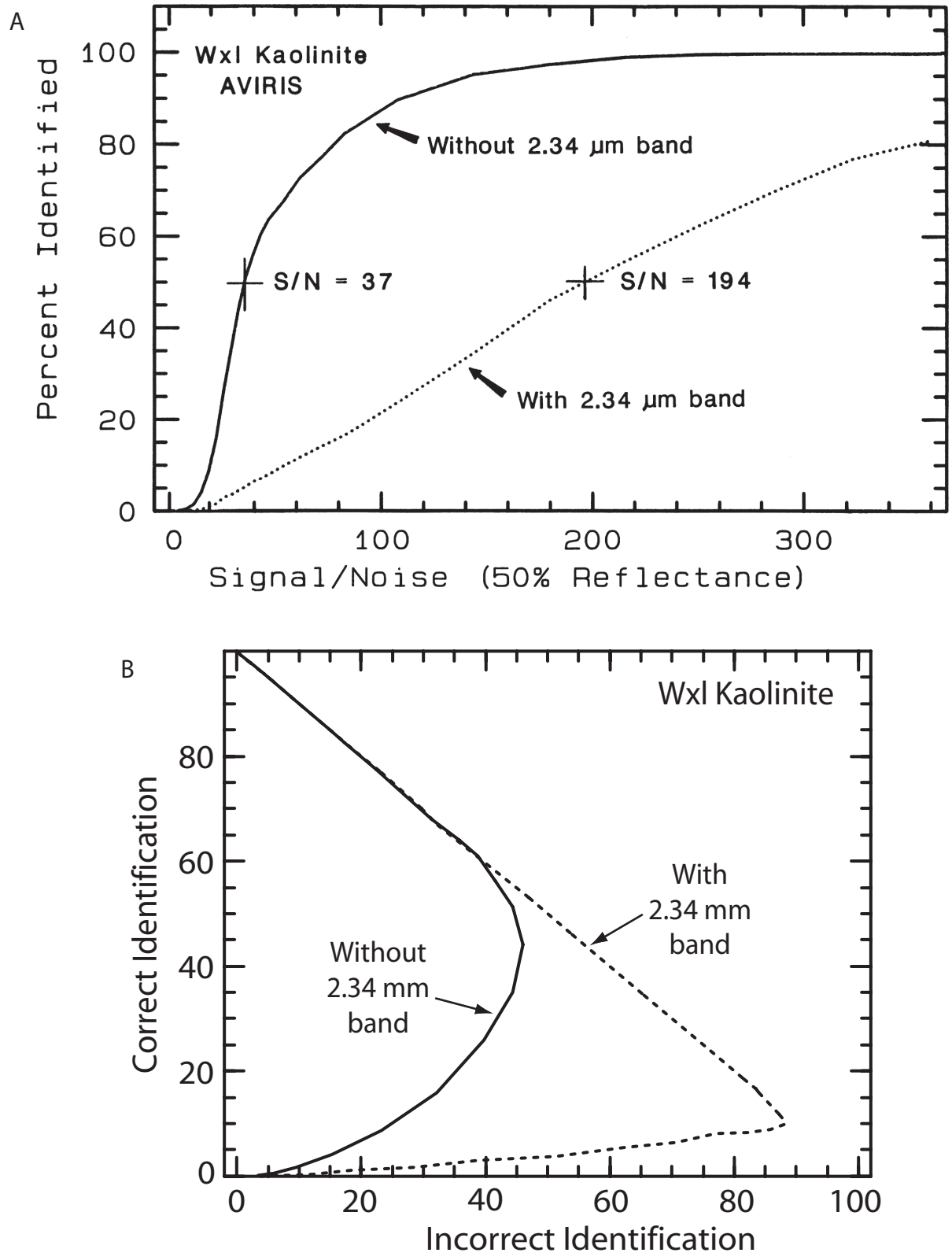

Figure 15. A) Identity curves for well-crystallized kaolinite at AVIRIS spectral resolution with and without inclusion of the 2.34-µm subordinate absorption in the Tetracorder analyses. Note the signal-to-noise ratio required for 50% correct identification of noisy kaolinite test spectra, using the 2.34- and 2.2-µm absorptions, is significantly higher than that required using only the 2.2-µm doublet for identification. B) Receiver operating characteristic curves for well-crystallized kaolinite with and without inclusion of the 2.34-µm subordinate absorption in the Tetracorder analyses.

($S/N_{ID50\%}$) of kaolinite test spectra, using the 2.34-μm absorptions, is 194 as compared with 37 using only the 2.2-μm doublet for identification. This result can be explained by the relative weakness of the 2.34-μm absorption. Generally, if a subordinate absorption is weak relative to the main absorption, noise will preferentially degrade the subordinate band's Fit resulting in more misidentifications. The comparison given in Figure 15 assumes that the S/N in the spectral regions of both main and subordinate absorptions is the same. Least-squares fitting of subordinate absorptions should be restricted to those cases where they are used to eliminate possibilities (e.g., testing for the presence of a 2.35-μm absorption to differentiate between muscovite and montmorillonite; see Clark et al., 2003). However, these subordinate absorptions may aid in identification when the S/N of the data is high enough to reveal their spectral details.

The identification of goethite using two of its Fe-absorptions (Figure 16) helps illustrate another spectral identification lesson. The 0.48-μm absorption appears weaker than the 0.98-μm absorption, but when both absorptions are divided by their continua to normalize their depths (Clark and Roush, 1984), the 0.48-μm absorption is actually 1.5 times deeper than the 0.98-μm absorption. Therefore, the 0.48-μm absorption is the strongest absorption of goethite within the 0.4 - 2.5 μm wavelength range. However when identity and ROC curves are calculated using both the 0.48- and 0.98-μm absorptions, they reveal that the deeper absorption band impedes identification. Figure 17 shows that identification using both absorptions requires a $S/N_{ID50\%}$ = 142 compared to $S/N_{ID50\%}$ = 20 using only the 0.98-μm absorption. Saturated bands like the 0.48-μm absorption are so low in reflectance, noise affects them preferentially, causing a poor individual Fit value which degrades the overall Fit value, ultimately leading to proportionately more misidentifications. However, imaging spectrometers typically have better S/N in the 0.5-μm region than at 1.0 μm, making it advantageous to use both absorptions for identification in most remote sensing applications. Figure 18 shows the identity and ROC curves for goethite (using only the 0.98-μm absorption) at AVIRIS resolution. Goethite test spectra were misidentified as lepidochrosite (a polymorph of goethite with a slightly broader absorption) and as a mineral with a non-uniquely shaped Fe^{2+}-absorption in the 1.0-μm region. In summary, use of weak subordinate bands or saturated absorptions with low reflectance levels can impede spectral identification unless the S/N of the spectrum is high enough to preserve sufficient spectral detail in these bands to aid the identification process.

5.2 Using Reflectance Values of Continuum Endpoints in the Fit Calculations

In an effort to improve the accuracy of Tetracorder, a test was done to see if including continuum endpoints in the Fit calculations would improve identification. Calcite was chosen for the test because its identity curve is rather simple. Figure 19 shows calcite identity and ROC curves with and without the use of endpoint channels in the Fit calculations. Results show that using continuum endpoints boosts the Fit values so that the S/N of identification at the 50% correct level ($S/N_{ID50\%}$) is reduced from 36 to 27, improving identification accuracy by 25% at the same S/N level. Tests on other minerals show improvements up to 50%. Continuum endpoints appear to provide additional spectral constraints valuable to the identification process, particularly at coarse spectral resolution where narrow absorptions are defined by only a few channels. Without least-squares fitting two or more continuum endpoints on either side, absorptions only one channel wide give perfect Fit values. These perfect Fits are caused by least-

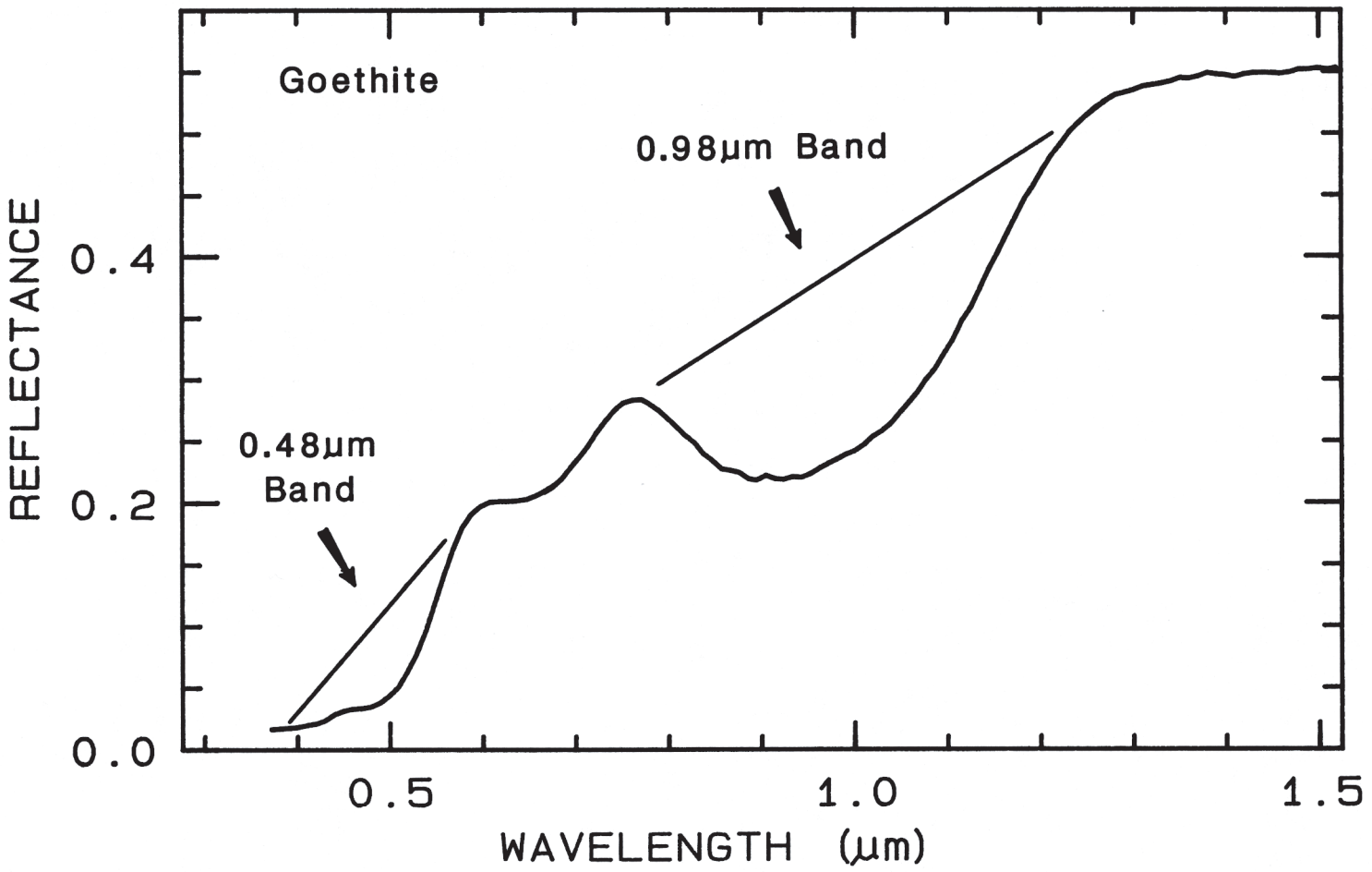

Figure 16. A reflectance spectrum of goethite with continua over the diagnostic absorption bands.

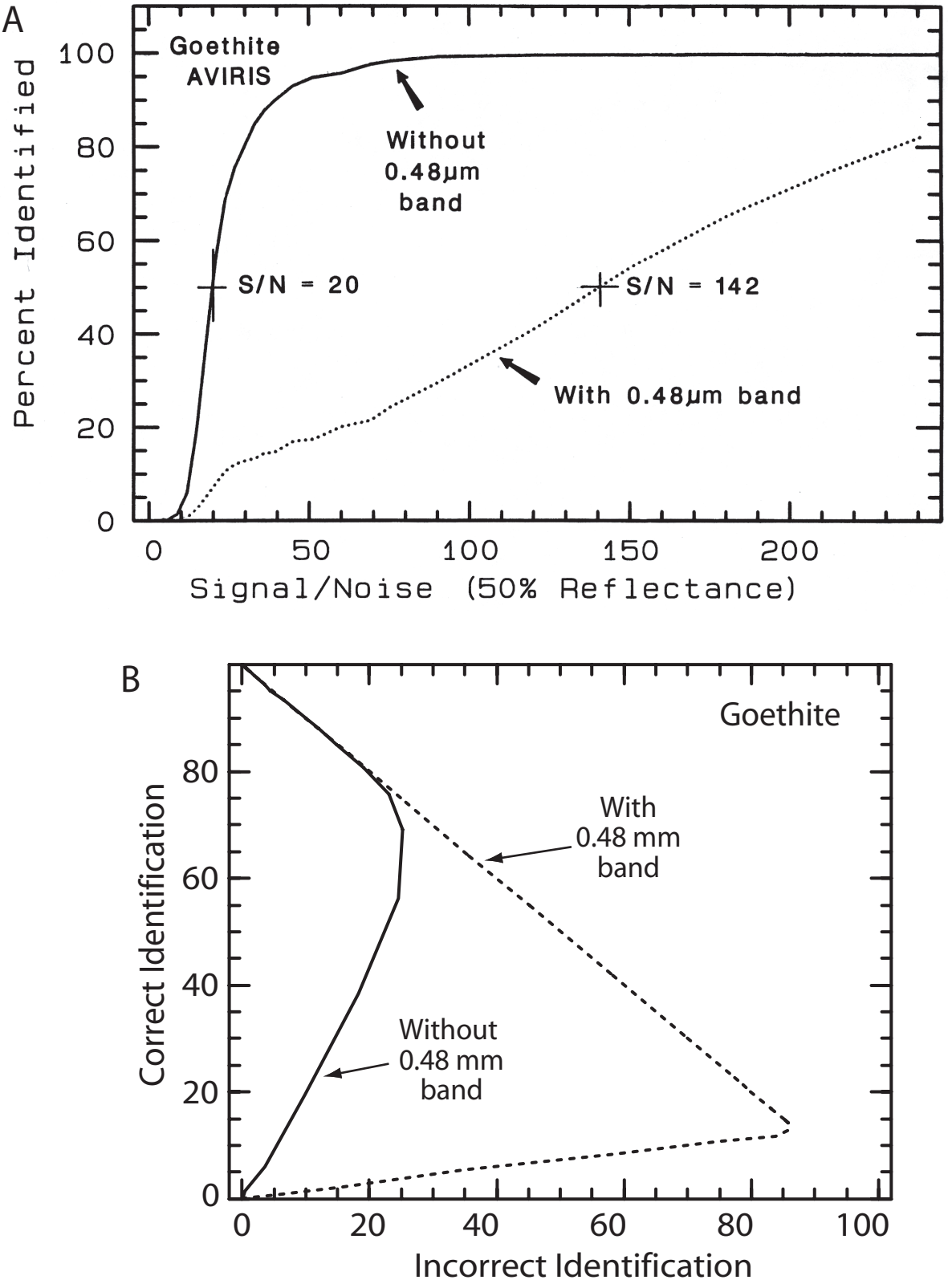

Figure 17. A) Goethite identity curves at AVIRIS spectral resolution with and without the use of the 0.48-µm absorption in Fit calculations. Because the 0.48-µm absorption is spectrally saturated, giving it a low reflectance, addition of random noise, uniform in magnitude at all wavelengths, preferentially degrades the Fit Tetracorder derived for goethite. B) Receiver operating characteristic curves with and without the use of the goethite 0.48-µm absorption in Fit calculations.

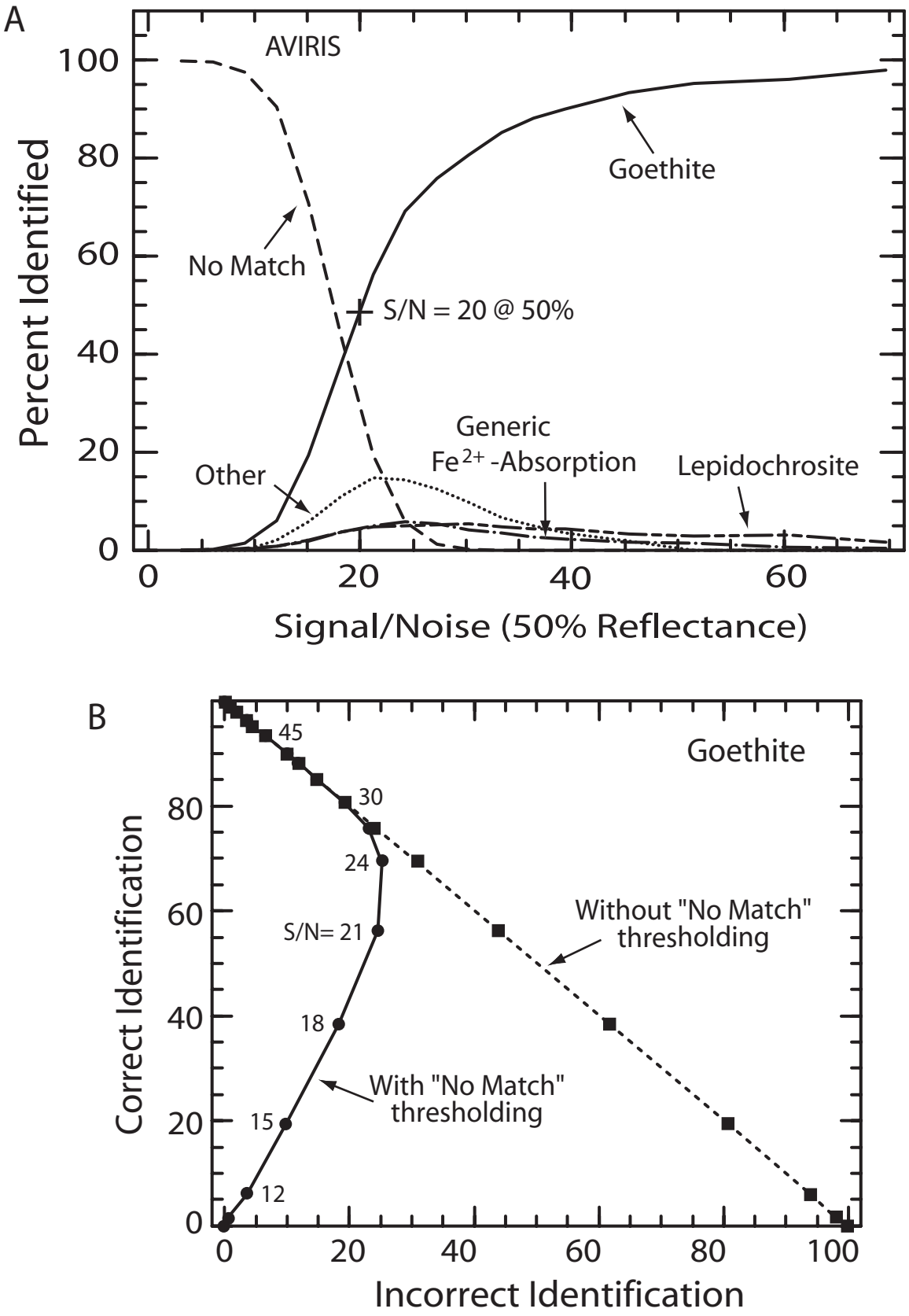

Figures 18. A) Percentage of noisy goethite test spectra correctly identified by Tetracorder as a function of signal-to-noise ratio (S/N) at AVIRIS spectral resolution using only the 0.98-μm absorption for Fit calculations. See text for explanation of curves. B) Receiver operating characteristic curves for noisy goethite test spectra. Numbers next to circles are the S/N values of the test spectra and also apply to the corresponding squares. Most test spectra are incorrectly identified at low S/N (dashed curve) but with the "No Match" threshold activated (solid curve) the number of test spectra incorrectly identified decreases substantially.

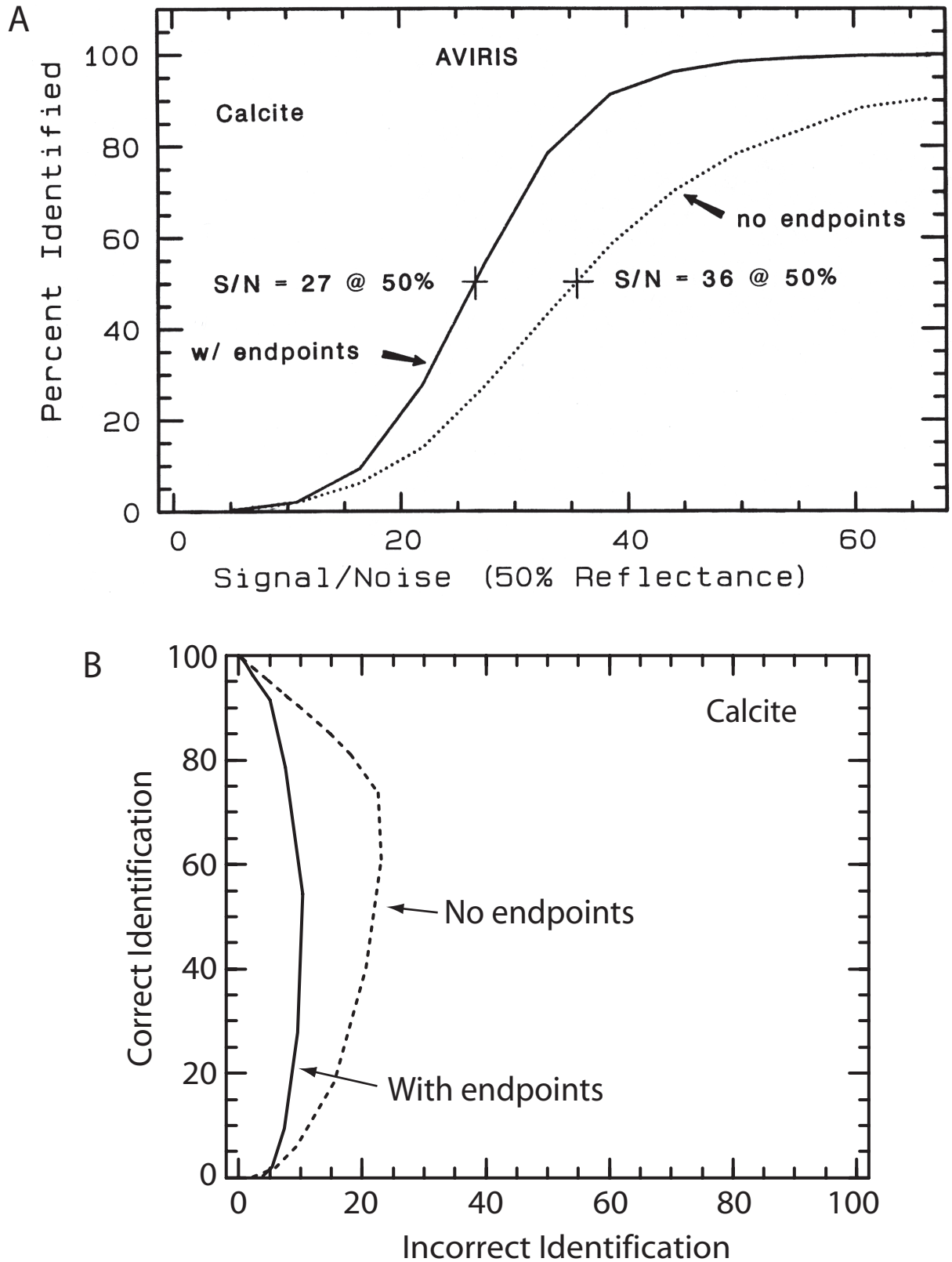

Figure 19. A) Identity curves for calcite at AVIRIS spectral resolution with and without the use of continuum endpoints in the Fit calculations. In general, for a given level of signal-to-noise ratio use of continuum endpoints increases the accuracy of Tetracorder identifications by25% for calcite and up to 50% for other minerals. B)Receiver operating characteristic curves for identification of noisy calcite spectra with and without the use of continuum endpoints in the Fit calculations.

squares scaling a one channel test spectral feature to a one channel library spectral feature. Unfortunately, there is a tendency for noise to imitate spectral features only one or two channels wide. Including multiple endpoints in the calculation gives a Fit based on five or more channels, thus reducing noise-related perfect Fits. For this same reason it is preferable to make the continuum span complex absorptions composed of multiple bands like the kaolinite doublet instead of breaking the continuum into shorter spans over each individual band. Doing so decreases the likelihood of noise mimicking a single absorption and contributing an erroneous perfect Fit to the identification process.

5.3 *S/N of identification* as a Function of Absorption Band Depth

In order to predict the impact of spectral abundance and grain-size variations that influence the strength of absorption bands and ultimately the identification process, a set of calcite test spectra were made with artificially reduced 2.34-μm band depths (Figure 20) to simulate the effect of mixing with other spectrally bland materials. Band depths of these spectra ranged from 3% to 100% of the original band's depth. Next, random noise was added to these spectra and they were identified by Tetracorder. Figure 21A shows the $S/N_{ID50\%}$ measured for each band depth in the set. Dividing these S/N_{ID} values by their corresponding band depth normalizes the band depth variations (Figure 21B). The fact that all of the normalized values plot on a horizontal line indicates that the S/N_{ID} is inversely proportional to band depth. For example, decreasing the band depth of a material by 50% requires doubling the S/N of its spectrum to achieve the same level of identification accuracy compared to the undiluted material. This test assumes that materials added to the pixel or mixture in order to decrease the depth of the target material's absorptions have spectra that are featureless at the wavelengths of the target material's diagnostic absorptions. If this condition is met, then the band depth of a material in areal or intimate mixtures can be used to estimate the S/N required for its identification using the identity curve for the pure material and its band depth measured from the mixture.

5.4 Imaging Spectrometer S/N Performance

All four imaging spectrometer configurations performed well in the test simulations. However, the simulations imply perfect atmospheric correction and identification of mostly pure endmember materials and a few mixtures. The actual performance under field conditions will be hampered by errors in radiative modeling of atmospheric transmission, solar irradiance, and path radiance corrections. In addition, surface materials commonly occur in as mixtures at the spatial scale of these sensors. Therefore, the following S/N_{ID} values given for each sensor should be viewed accordingly. For mathematical convenience most of the S/N_{ID} values in the following discussion are for identification at the 50% correct level; significantly higher S/N levels may be needed to attain the higher accuracy necessary for many remote sensing applications.

AVIRIS performance will be considered first. Table 3 shows the $S/N_{ID50\%}$ values for 30 materials at AVIRIS spectral resolution. For the AVIRIS simulations, materials were divided into two groups: those having electronic absorptions and those having vibrational absorptions. In the electronic region, the most difficult identifications were between spectra of the hematite grain size series, where a $S/N_{ID50\%} > 332$ was required to separate coarse hematite from medium hematite. Coarser grains absorb more and scatter less resulting in deeper broader 0.46- and 0.88-

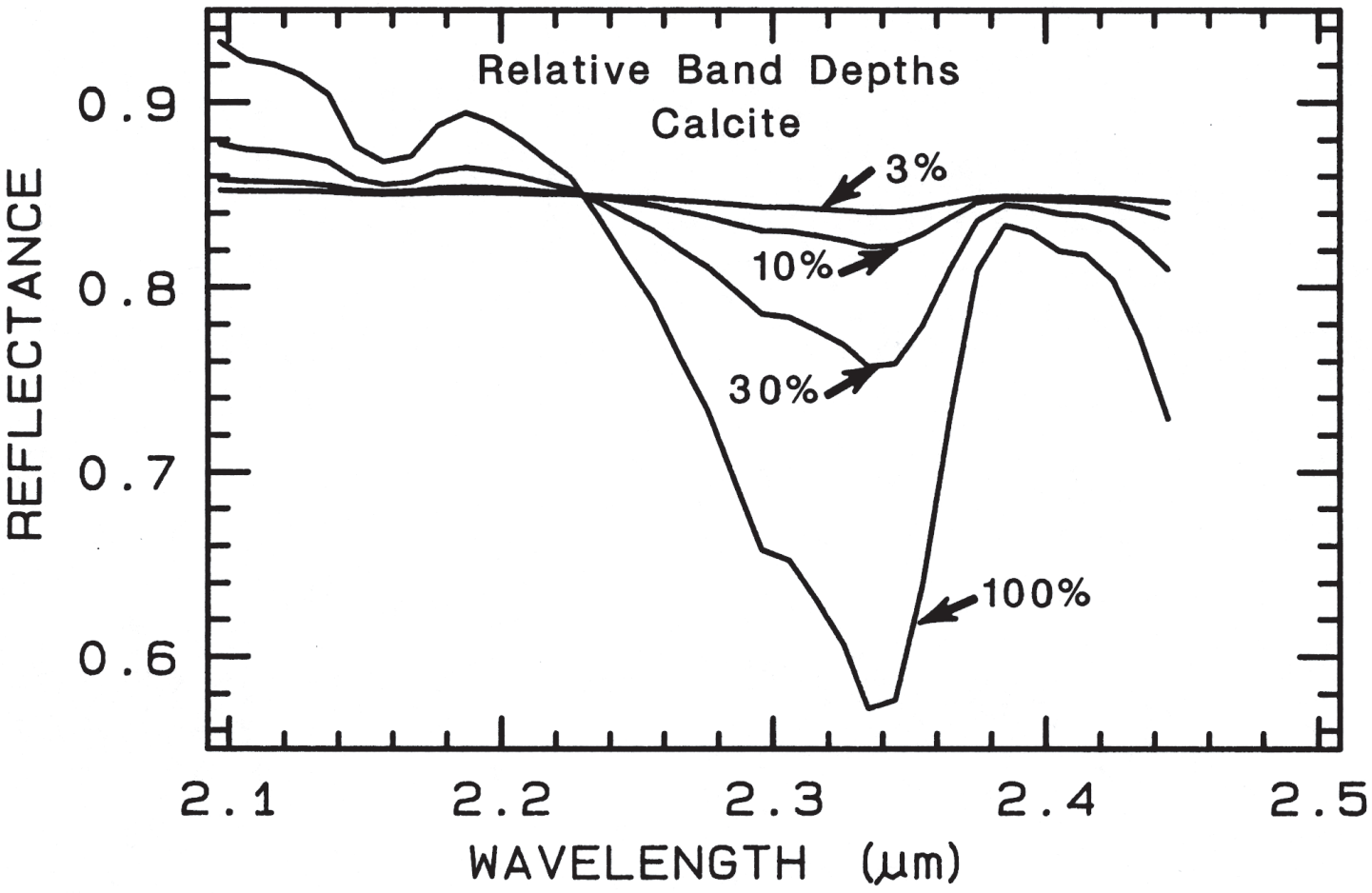

Figure 20. Reflectance spectra of the calcite 2.34-μm absorption at different band depths. All spectra were produced from the 100% strength absorption by multiplying by the appropriate fraction and adding a constant to restore the spectrum to its original reflectance level. This series of spectra simulate areal mixtures of calcite with a spectrally bland material in proportions that reduce the 2.34-μm absorption depth to the indicated level.

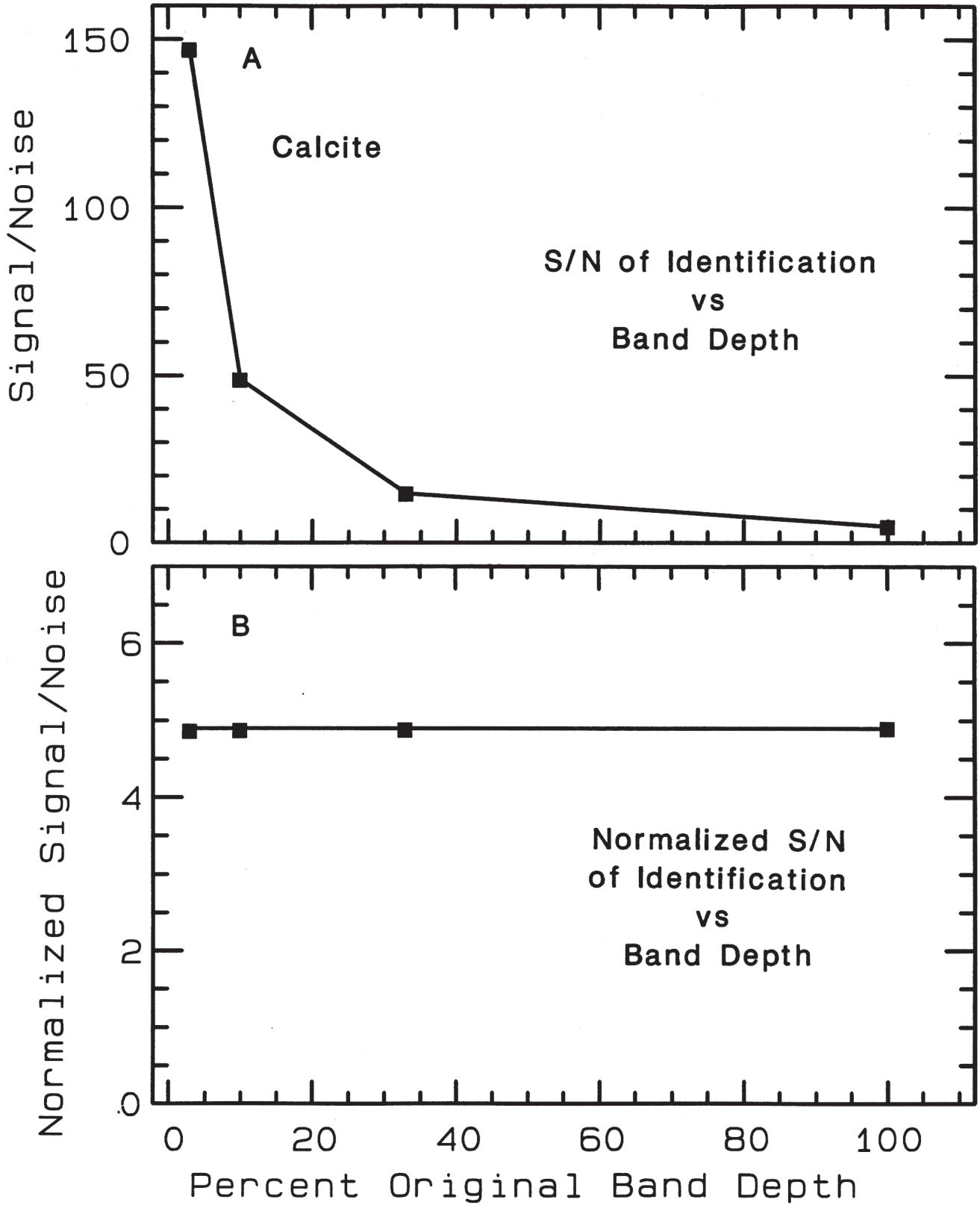

Figure 21. A) Signal-to-noise of identificationat 50% correct level as a function of the percentage of the original band depth for the calcite spectra shown in Figure 20. B) Signal-to-noise of identification (S/N_{ID}) normalized by dividing by the percent original band depth. Because these values plot on a horizontal line, the S/N_{ID} increases linearly as band depth decreases.

Table 3. AVIRIS: signal-to-noise of identification (S/N_{ID}) at 50% correct level.

Material	S/N_{ID}	Main Interference
Electronic Region (0.4 - 1.35 μm)		
Amorphous Fe-hydroxide	20	Nanocrystalline hematite
Fe-chlorite	29	Amphiboles, olivine
Goethite	20	Generic Fe^{2+} absorption (significant)
Nanocrystalline hematite	15	Fine-grained hematite
Fine-grained hematite	36	Coarse-grained and nanocrystalline hematite
Medium-grained hematite	379	Coarse-grained hematite, jarosite (200°C)
Coarse-grained hematite	332	Coarse- & medium-gr. hematite, jarosite (90°C)
K-jarosite (90°C)	108	K-Jarosite (200°C), coarse-grained hematite
K-jarosite (200°C)	36	K-Jarosite (90°C), generic Fe^{2+} absorptions
Nontronite (Fe-smectite)	108	Generic Fe^{2+} absorption
Juniper tree	182	Rubber rabbit brush
Maple leaves	146	Aspen leaves
Vibrational Region (1.35 - 2.5 μm)		
K-alunite (450°C)	42	K-alunite (250°C & 150°C), wxl kaolinite
Calcite	27	Epidote (very slightly)
Fe-chlorite	33	Intermediate Fe-chlorite
Dickite (kaolinite polymorph)	33	Poorly-crystallized kaolinite
Dolomite	27	Magnesite-hydromagnesite (slightly)
Gypsum	33	None
Halloysite (kaolinite group mineral)	46	Poorly-crystallized kaolinite
Fe-Illite	41	Intermediate Al- and Fe-muscovites
Well-crystallized kaolinite	37	Poorly-crystallized kaolinite
Poorly-crystallized kaolinite	82	Well-crystallized kaolinite
Na-jarosite	44	H_3O-jarosite
Na-montmorillonite	34	Fe-Illite, intermediate Al-muscovite
Al-muscovite	92	Interm. Al-muscovite, kaolinite/smectite mix
Intermediate Al-muscovite	63	Al-muscovite, kaolinte/smectite mix
Fe-muscovite	68	Fe-Illite, intermediate Al-muscovite, Ca-mont.
Nontronite (Fe-smectite)	24	Magnesite-hydromagnesite
Lawn grass	46	Fir Tree (slightly)
Dry long grass	31	Hectorite ("No Match" set high)

gr. = grained; wxl = well-crystallized; interm. = intermediate; mont. = montmorillonite.

μm absorptions in spectra of coarse hematite, all without shifts in the positions of the absorption band centers. Jarosite, goethite, and hematite can be differentiated by AVIRIS at $S/N_{ID50\%} > 36$ for concentrations producing 10% band depths. A S/N > 800 is needed to spectrally distinguish most grain-size and abundance combinations of these phases in the field to a moderate degree of accuracy at AVIRIS resolution (Swayze et al., 2000).

In the vibrational region, spectral identification of the chemical composition of muscovite is possible using AVIRIS spectral resolution. Incorporation of Fe and Mg into the octahederal sites in muscovite distorts the crystal structure causing octahederal layer Al-OH bonds to lengthen (Swayze, 1997). This change in bond length shifts the 2.2-μm absorption in muscovite spectra to longer wavelengths and Fe-OH and Mg-OH bonds give rise to shoulders on the long wavelength side of the 2.2-μm absorption (see Figure 2) allowing spectral differentiation of the solid-solution series members. Although subtle, these changes can be used to spectrally map muscovite composition. Marinez-Alonso (2000) attributes the apparent Al-OH combination band shifts to changes in the relative strengths of different fundamental bands produced by Al-coordinated OH, due to OH located in different crystallographic sites of the unit cell, and to lack of perfect crystallinity, as observed by Saksena (1964). A $S/N_{ID50\%} > 63$ is required to distinguish pure intermediate Al-muscovite from either Al-rich or Al-poor muscovite and kaolinite/smectite mixtures using AVIRIS data.

Alunite spectra can provide compositional information and formation temperatures. Substitution of Na for K in alunite shifts the 1.48- and 2.16-μm absorptions toward longer wavelengths (Figure 2). In Al-deficient alunites, higher formation temperatures drive off excess H_2O, increasing the order of the OH sites, causing the 2.16-μm absorption to widen (Swayze, 1997). Spectral differentiation between 450°C and 250°C alunite requires a $S/N_{ID50\%} > 42$ at AVIRIS resolution.

Simulation results for HYDICE (Table 4) are similar to those for AVIRIS, except for alunites, where the broader bandpass (BP) of HYDICE in the 1.5-μm region results in a wider, less diagnostic 1.46-μm absorption, requiring a higher S/N_{ID}, despite the narrow BP of HYDICE in the 2.2-μm region. In contrast, MIVIS spectra cannot be used to accurately define the 1.0-μm Fe-absorptions because of a gap in spectral coverage from 0.82 to 1.17 μm. This gap prevents placement of continuum endpoints on the long wavelength side of the 1.0-μm absorptions. However, MIVIS data can be used to distinguish between Fe-bearing materials by using the 0.4-μm region absorptions but at an order of magnitude higher S/N (Table 4). Thus, the potential loss of diagnostic spectral information beyond the silicon detector cutoff at 1.0 μm must be weighed against cost savings when designing spectrometers. MIVIS performance was similar to that of AVIRIS and HYDICE in the vibrational region where it has a narrow BP. It is possible that MIVIS performance could be enhanced with additional spectral information from the thermal IR channels between 8.2 and 12.7 μm. Information from these additional wavelengths was not evaluated in this study.

The VIMS configuration performed satisfactorily considering its relatively broader spectral resolution in the near-infrared spectral region (~ 17 nm). VIMS's step-like change from narrow to broad BP at 0.96 μm has little effect on the S/N_{ID} of minerals with broad electronic absorptions at 1.0 μm when compared to those of the other spectrometers (Table 4). VIMS performed almost as well as AVIRIS in the electronic region simulations. However, in the vibrational region, the broader BP of VIMS prevented materials from being identified as consistently as with AVIRIS, but the S/N_{ID} was not much higher than that for AVIRIS. VIMS's measurement of absorptions between 2.5 and 5.1 μm could provide additional information,

however, these wavelengths were not evaluated for VIMS in this study. When detectable, the additional spectral information acquired from these wavelengths may improve identification at S/N values below those listed in Table 4.

Table 4. Signal-to-noise of identification at 50% correct level for the four spectrometers.

Material	AVIRIS	HYDICE	MIVIS	VIMS
	Electronic Region (0.4 - 1.35 μm)			
Goethite	20	22	209	23
Fine-grained hematite	36	29	55	32
K-jarosite (200°C)	36	60	207	38
Brown camouflage	n.d.	15	n.d.	n.d.
	Vibrational Region (1.35 - 2.5 μm)			
K-alunite (450°C)	42	54	68	64
Calcite	27	27	28	30
Well-crystallized kaolinite	37	37	47	54
Na-montmorillonite	34	35	31	48

n.d. = not determined.

5.5 An Example Using Actual AVIRIS Data

Mineral maps derived from AVIRIS data sets using the Tetracorder algorithm were created as part of this study. Optical and electronic improvements to AVIRIS have increased the S/N of the sensor up to sixfold during the five years between collection of the two data sets (Figure 22).

The data sets where acquired on July 23, 1990, and on June 23, 1995, by the AVIRIS instrument mounted on an ER-2 aircraft flying at an altitude of 20 km over Cuprite, Nevada. In each case solar flux, atmospheric absorptions, and scattering where removed from the data using the ATREM program (Gao et al., 1993). Artifacts from the above processing where then removed by multiplying the data sets by correction factors derived from field spectra of a ground calibration site (Clark et al., 1993b; Clark et al., 2002). Each data set was mapped using the same Tetracorder spectral library. Figures 23 and 24 show the electronic and vibrational region mineral maps for the 1990 and 1995 data sets. The main geologic features at Cuprite are the twin hydrothermal alteration centers consisting of concentric zones of alunite surrounded by kaolinite zones (Abrams et al., 1977; Ashley, et al., 1980; Goetz and Strivastava, 1985; Shipman et al., 1987; Kruse, et al., 1990; Simon, 1990; and Swayze, 1997). In terms of Fe-mineralogy, the western center is characterized by widespread jarosite and goethite and the eastern center is

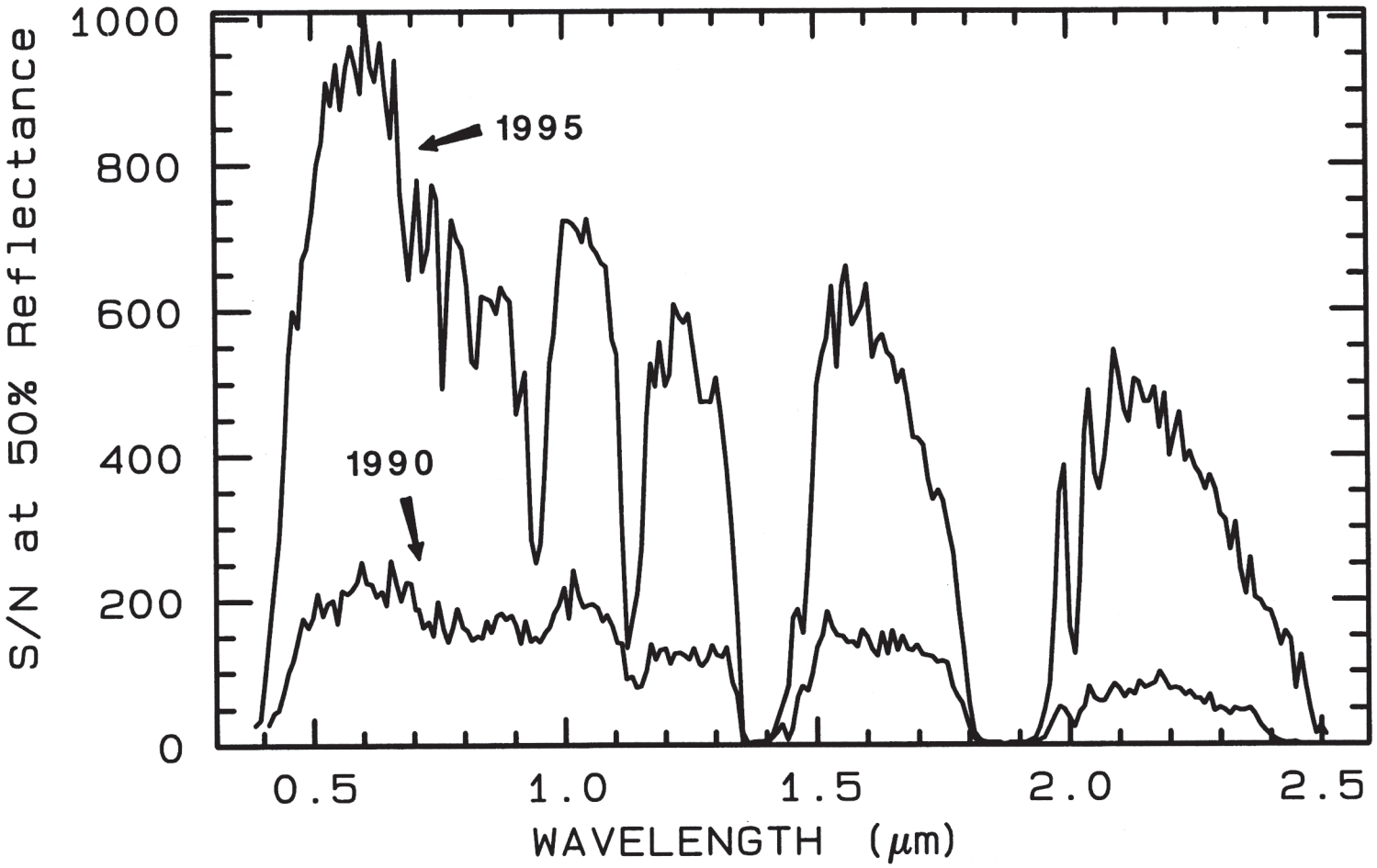

Figure 22. Signal-to-noise ratios (S/N) at 50% reflectance of AVIRIS 1990 and 1995 data over Cuprite, Nevada. Solar zenith angles and atmospheric conditions are those experienced during the overflights. The AVIRIS 1990 S/N profile was derived from the standard deviation of a hundred pixel average reflectance spectrum of AVIRIS data over the Alkali Flat playa 6 km south of Cuprite. The AVIRIS 1995 S/N profile was derived from the standard deviation of the dark measured at the end of the flight line corrected to reflectance using the method outlined by Boardman (1995).

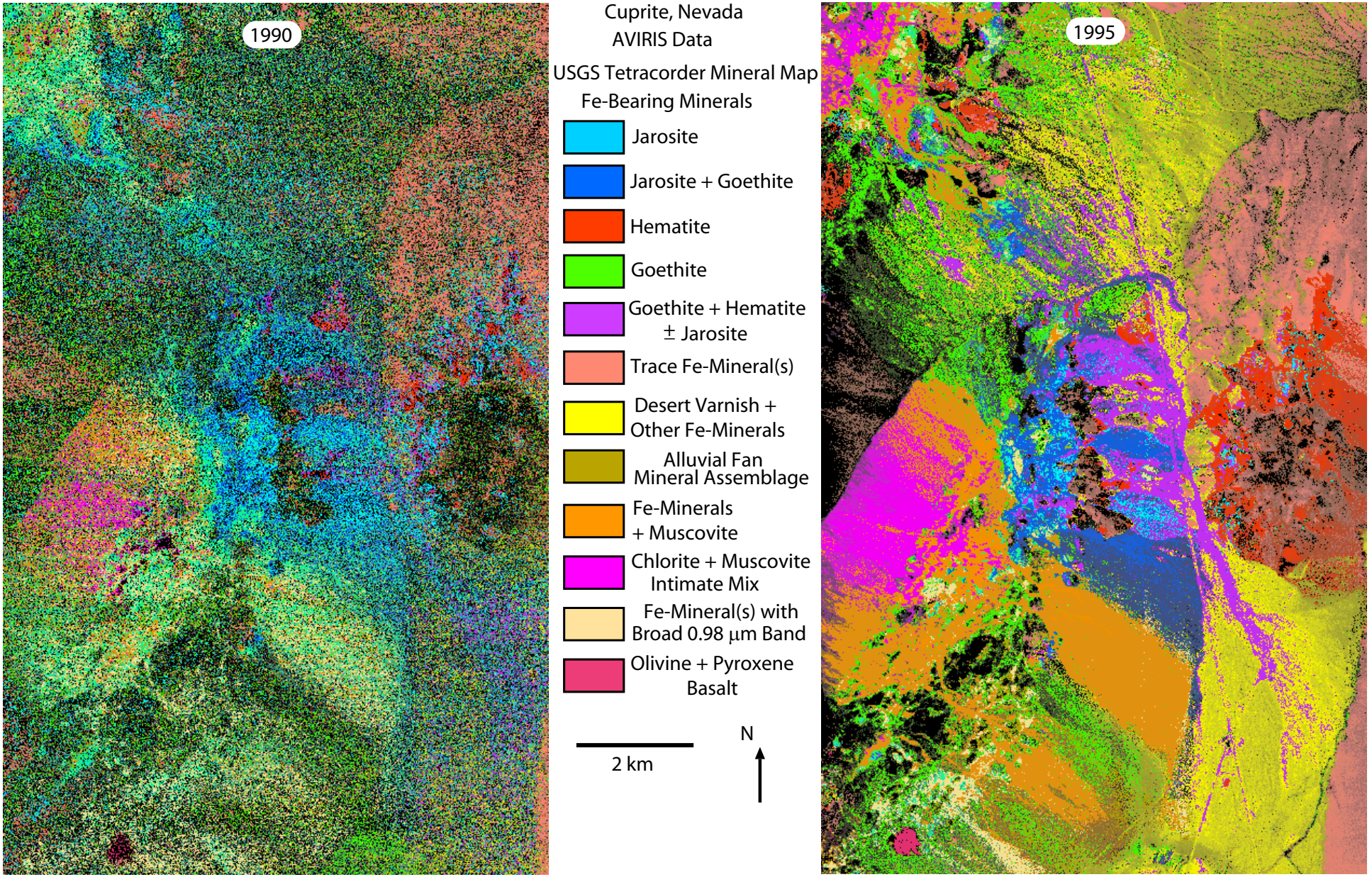

Figure 23. Mineral map of the electronic absorption spectral region (0.4 -1.35μm) created using the Tetracorder algorithm from AVIRIS data collected in July 1990 and June 1995 over the hydrothermal alteration systems at Cuprite, Nevada. The signal-to-noise ratio of the 1995 data is about four times higher than that of the 1990 data in this spectral region. Neither image is geometrically registered to avoid resampling of pixels which could modify the pattern of noise, consequently they approximately cover the same area on the ground.

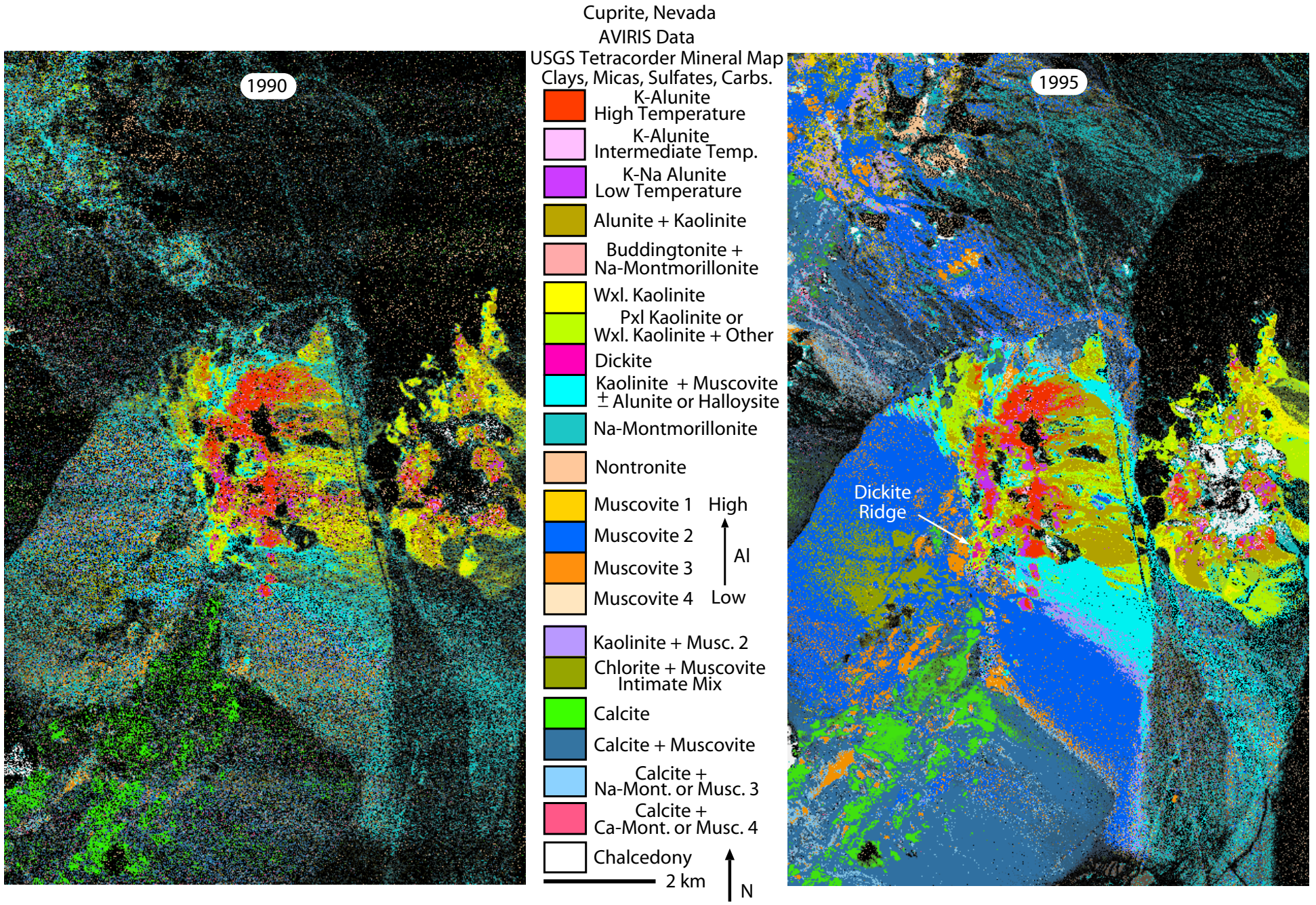

Figure 24. Mineral map of the vibrational absorption spectral region (1.35 - 2.5µm) created using the Tetracorder algorithm from AVIRIS data collected over Cuprite. The signal-to-noise ratio of the 1995 data is about six times higher than that of the 1990 data in this spectral region. The 1990 map has mineral patterns with noise levels similar to that of the 50% correct level example shown in Figure 12, whereas the level of mineral pattern noise in the 1995 mineral map resembles that at the 90% correct level. Coherent mineral patterns in the 1995 data can be used to make geologic interpretations that would be only marginally possible with the 1990 data. As in the previous figure, neither image is geometrically registered. Carb. = carbonate; temp. = temperature; wxl. = well-crystallized; pxl. = poorly-crystallized; musc. = muscovite; mont. = montmorillonite.

dominated by hematite. The areas surrounding the western center consist of Cambrian metasedimentary rocks with muscovite-rich zones that vary in Al and Fe composition; north and south the metasediments are interbedded with limestone. The eastern center is bordered on the north by unaltered volcanic rocks that have weak Fe-absorptions but lack minerals with strong vibrational absorptions; consequently no minerals from the vibrational portion of the spectral library were found in these areas at significant levels. These mineral maps also show the dispersal of eroded bedrock minerals onto the surrounding alluvial fans (Swayze, 1997).

Because the spectrally detectable minerals exposed at Cuprite occur as mixtures with other minerals, their spectral signatures are diluted. In most cases, spectral identification of these minerals requires higher S/N values than for the pure mineral phases (Table 3), especially on alluvial fans where the spectral signatures of minerals are diluted by signatures from soil and vegetation. This effect is most apparent in the 1990 AVIRIS mineral maps. The weakest mineral patterns are those expressed on the alluvial fans where the relatively low S/N of the 1990 data results in more misidentifications (speckled pattern) than seen in the maps of the 1995 data (solid pattern). If the speckle was due to mixed pixels where the spectrally-dominant mineral varied from pixel to pixel then a similar speckle pattern would be observed in the 1995 data because of better mapping accuracy at its higher S/N level. The most coherent patterns identified in the 1990 data are coincident with bedrock areas rich in goethite, hematite, jarosite, alunite, calcite, chalcedony, kaolinite, and muscovite.

The S/N of the 1990 AVIRIS data is high enough to allow differentiation of jarosite from hematite and goethite as predicted by the simulations, but is too low to reproduce the coherent pattern of the goethite + hematite ± jarosite areal mixture seen in the 1995 mineral map between the hydrothermal centers (Figure 23). Iron-mineral distribution patterns on alluvial fans are clearly dominated by single mineral categories in the 1995 maps although they are barely recognizable in the 1990 maps. It is apparent from this example that mineral maps created from low S/N spectral data should be used to map only a few broad categories of materials. Conversely, higher S/N may allow the differentiation of spectrally similar materials in many different categories. This relationship should be relatively independent of the method used for spectral identification (e.g., Tetracorder, unmixing, or neural networks).

As predicted from the modeling, differentiation of the kaolinite group minerals was achieved using the 1990 data. Modeling predicts a relatively low $S/N_{ID50\%} = 33$ for dickite, a value much lower than the S/N (~ 80) of 1990 AVIRIS data in the 2.2-μm region (Figure 22). The detection of scattered pixel clusters spectrally dominated by dickite on a ridge extending southwest from the western center (Figure 24), and X-ray diffraction verification of dickite in field samples collected from these areas (Swayze, 1997), corroborates our modeling results. A more rigorous test involves mapping alunite. As stated previously, the simulations predict that a $S/N_{ID50\%} > 42$ is required to differentiate high and intermediate temperature K-alunite. The presence of numerous rock outcrops spectrally dominated by high temperature K-alunite in the western center and similar outcrops of intermediate temperature K-alunite in the eastern center implies that the western center was once hotter than the eastern center at least at their present level of exposure. The S/N level of the 1990 data was adequate for differentiating both types of

alunite. Although test spectra of chalcedony were not modeled, the spectral detection of a large expanse of chalcedony (hydrous SiO_4) in the eastern center with the 1995 data but barely detectable with the 1990 data, indicates that this mineral's spectral signature is weak (as field data indicates from partial concealment beneath a coating of lichen). These mineral maps demonstrate that Tetracorder's band shape fitting technique works for both pure materials and mixtures.

6.0 DISCUSSION

To this point, model results have dealt with predicting the performance of existing imaging spectrometers. In the following discussion, the effects of bandpass (BP), sampling interval (SI), and signal-to-noise ratio (S/N) on spectral identification are explored in a more comprehensive way, with the goal of establishing the relative importance of these spectral parameters in the identification process.

6.1 Bandpass Effects on Spectral Identification

To measure the effects of BP on identification, test spectra were created from a well-crystallized (wxl) kaolinite spectrum convolved to BP widths ranging from 10 to 100 nm while maintaining a constant SI of 10 nm. Random noise was added to the test spectra and identity curves similar to that shown in Figure 13 were constructed for each BP, and then signal-to-noise of identification at 50% correct ($S/N_{ID50\%}$) values were determined for each identity curve. Figure 25 shows a $S/N_{ID50\%}$ curve where these S/N_{ID} values are plotted as a function of BP. As expected, the kaolinite test spectra convolved to broader bandpasses require higher S/N for correct identification. This finding is consistent with the observation that the spectral details of absorption bands are smeared out as BP broadens, making bands less diagnostic and more likely to be confused with other absorptions having similar wavelength positions.

For a given BP and SI there will be a S/N required to make a spectral identification at a given level of accuracy within a group of materials. This required S/N differs from the S/N achievable with a spectrometer because the later is dependent on spectrometer type, optical geometry, grating efficiency, detector sensitivity, target albedo, and signal level among others parameters. Curves in Figure 25 and in subsequent figures show the required S/N curves of identification at a given probability (e.g., 50% and 90% correct).

6.2 Sampling Interval Effects on Spectral Identification

To measure the effects of SI on identification, test spectra were created from a wxl kaolinite spectrum convolved to SI and BP values incremented from 4 to 31 nm. Random noise was added to the test spectra and identity curves were constructed for each increment, and then $S/N_{ID50\%}$ values were determined for each identity curve. Figure 26 shows a $S/N_{ID50\%}$ curve where the S/N_{ID} values are plotted as a function of SI where BP = SI as in many imaging spectrometers. The defined upper limit of 31 nm represents the SI above which a few materials in the spectral library have absorptions that are only one channel wide at the same wavelength position. Hence a spectrum of any one of these materials does not have a unique spectral shape and cannot be differentiated from the others with single channel features at the same wavelength. Theoretically each library spectrum has different maximum BP and SI values beyond which it cannot be

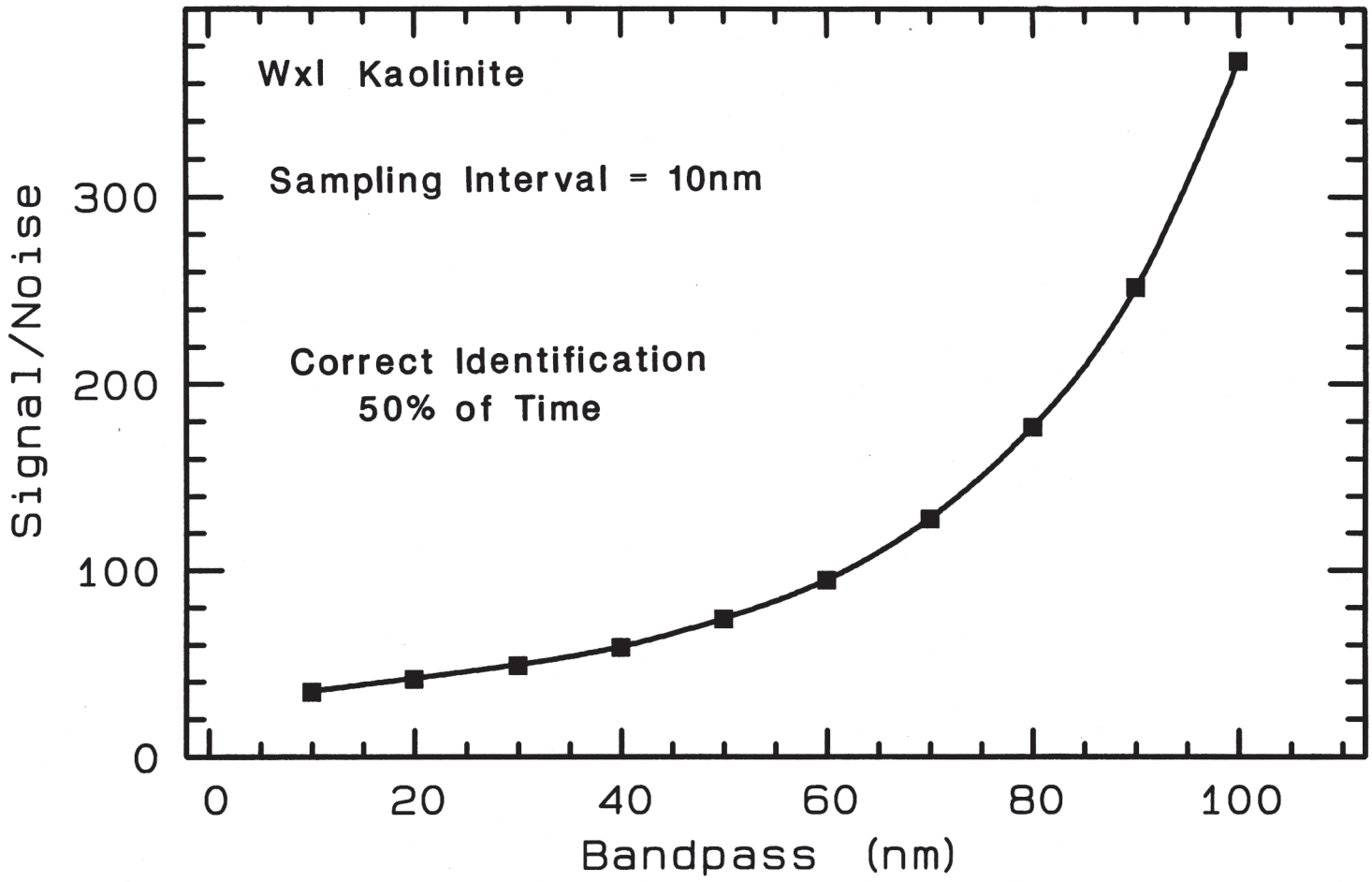

Figure 25. Signal-to-noise of identification (S/N_{ID}) curve showing S/N_{ID} values for the 50% correct level as a function of bandpass for well-crystallized kaolinite. The sampling interval of the test spectra was held constant at 10 nm. Signal-to-noise of identification increases rapidly at broad bandpasses, indicating that as bandpass exceeds the absorption band's FWHM confusion with spectral features of other materials may prevail.

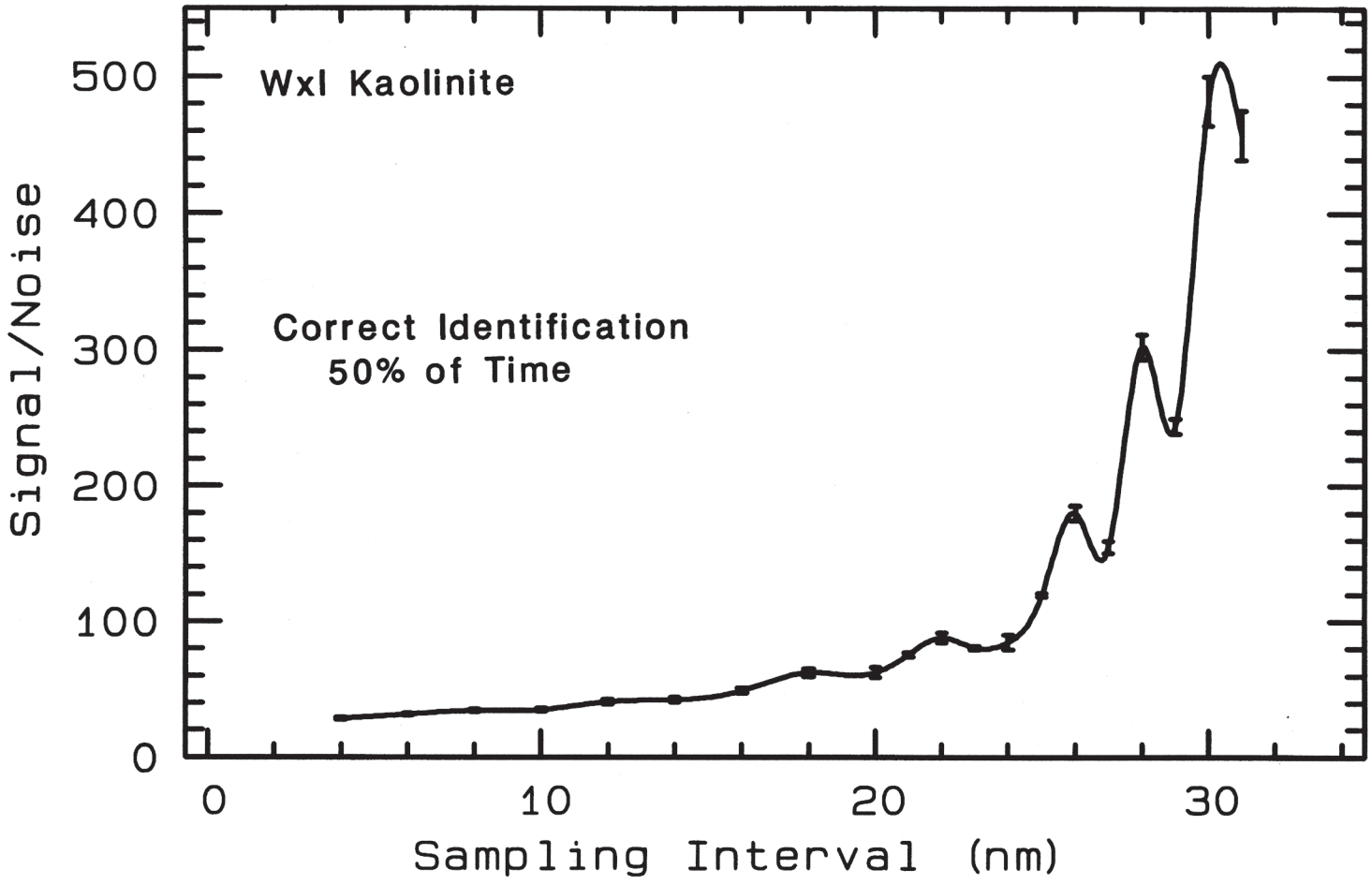

Figure 26. Signal-to-noise of identification (S/N_{ID}) curve showing S/N_{ID} values for the 50% correct level as a function of sampling interval for well-crystallized kaolinite. Test spectra are critically sampled (bandpass = sampling interval). Bars represent estimates of error in the position of identity curves used to derive the S/N_{ID} values.

differentiated regardless of S/N. A way around this limitation is to group spectrally similar materials together till the groups become spectrally unique relative to each other. Doing this will allow spectral differentiation at relatively broad BP and SI but will lower the information content of the resulting spectral maps.

The kaolinite S/N_{ID} curve increases as SI broadens (Figure 26). The point where the curve abruptly steepens (SI ~ 24 nm) is defined as the base of the identification wall above which the S/N_{ID} rapidly increases toward infinity with small increases in SI. The last data point on the curve at 31nm is the BP and SI combination above which well-crystallized kaolinite can no longer be differentiated from other minerals using the spectral library.

6.2.1 Spectral Aliasing and S/N_{ID} Curve Ringing

Superimposed on the S/N_{ID} curve in Figure 26 is a series of oscillations or ringing features that start at SI ~ 12 nm and increase in amplitude toward SI = 31 nm. Ringing is undoubtably present at all SI values, but is of very low amplitude at narrow SI values where it is effectively invisible at the scale of this plot. The ringing is apparently caused by spectral aliasing, a condition where the width of the SI and wavelength location of a spectrometer's channels can distort the true shape of a spectral absorption, causing it to resemble other absorptions. This situation can occur when the SI is nearly as broad as the narrowest diagnostic absorption of a material and the position of a channel does not coincide with or is not located near the bottom of the absorption. To test this hypothesis, a wxl kaolinite library spectrum was convolved eight times to a BP and SI equal to 28 nm, each time shifting the sampling position by 4 nm to shorter wavelengths (Figure 27). Listed to the right of the spectra are the corresponding $S/N_{ID50\%}$ values for noisy spectra generated from each convolved kaolinite spectrum. These S/N_{ID} values have nearly a two-fold variation produced solely by shifting channel position.

A second experiment was conducted using a kaolinite spectrum convolved to BP and SI equal to 14 nm. The convolution was repeated eight times, each time shifting the sampling position by 2 nm increments. Shifts in sampling position had little affect on S/N_{ID} values (~ 43) for noisy spectra generated from these spectra (Figure 28). The two sets of S/N_{ID} values plotted on the kaolinite S/N_{ID} curve are compared in Figure 29, which shows that ringing can be attributed to spectral aliasing. This experiment highlights the effects of spectral aliasing which are most pronounced when the SI coincides with that of the identification wall on the S/N_{ID} curve of a material. However, because there is less spectral aliasing at narrow SI values, the effect is likely to be small for spectrometers that have spectral resolutions that coincide with the flat portion of the S/N_{ID} curves for most of the minerals (e.g., AVIRIS and HYDICE). When using imaging spectrometer data with broad bandpasses and sampling intervals (> 16 nm), it would be useful to construct S/N_{ID} curves to optimize spectrometer channel positions to maximize the spectral contrast between materials likely to be encountered in the field. However, this may be difficult because the ringing in one curve may not be in phase with that in another S/N_{ID} curve of a different material. A better approach would be to use a BP and SI adequate for the most difficult identification in each spectral region.

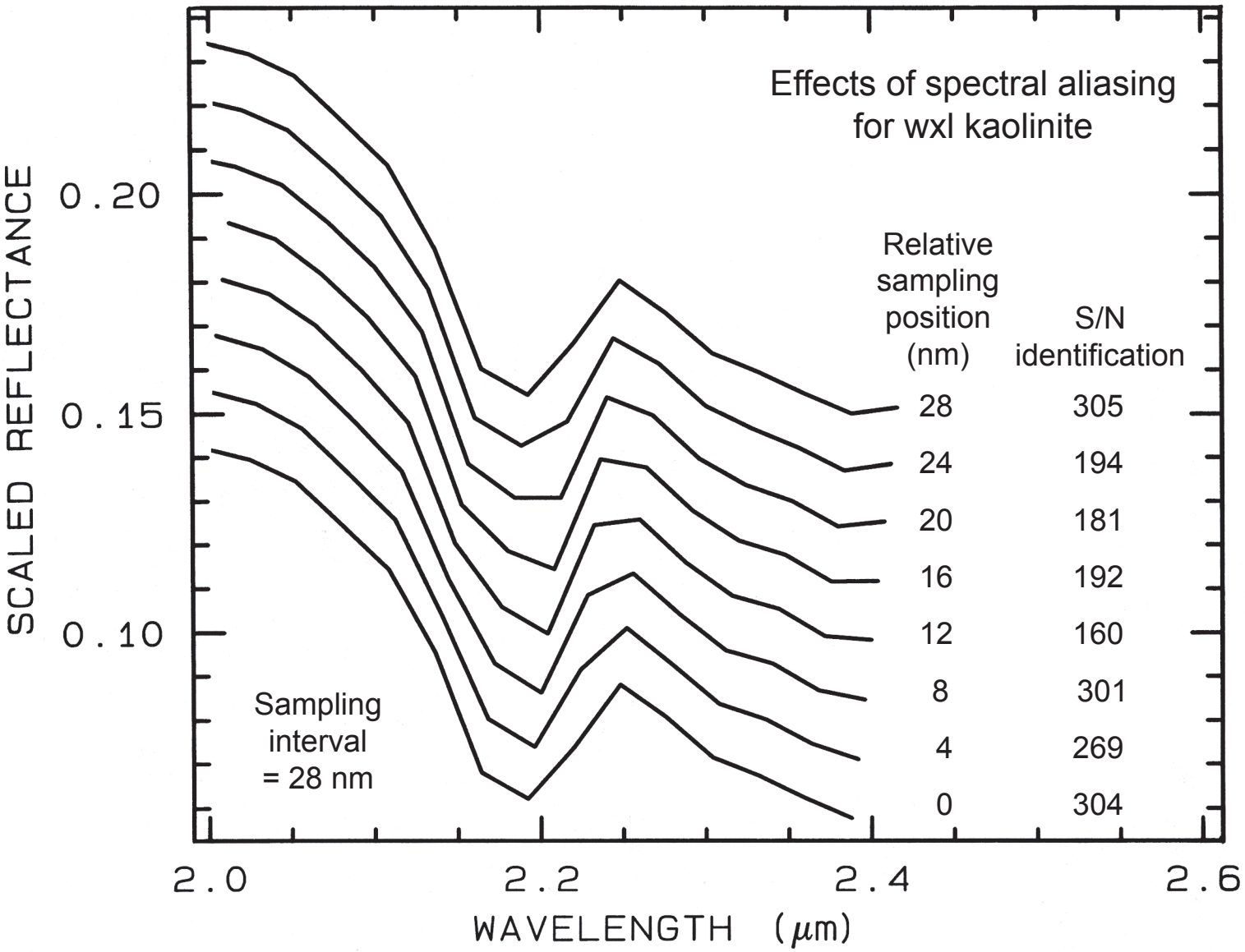

Figure 27. Details of the 2.2-μm absorption of a well-crystallized kaolinite convolved eight times to a bandpass and sampling interval equal to 28 nm, each time shifting the sampling position 4 nm toward shorter wavelengths. Listed to the right of the spectra are the corresponding signal-to-noise of identification values for the 50% correct level calculated for noisy test spectra generated from each convolved kaolinite spectrum.

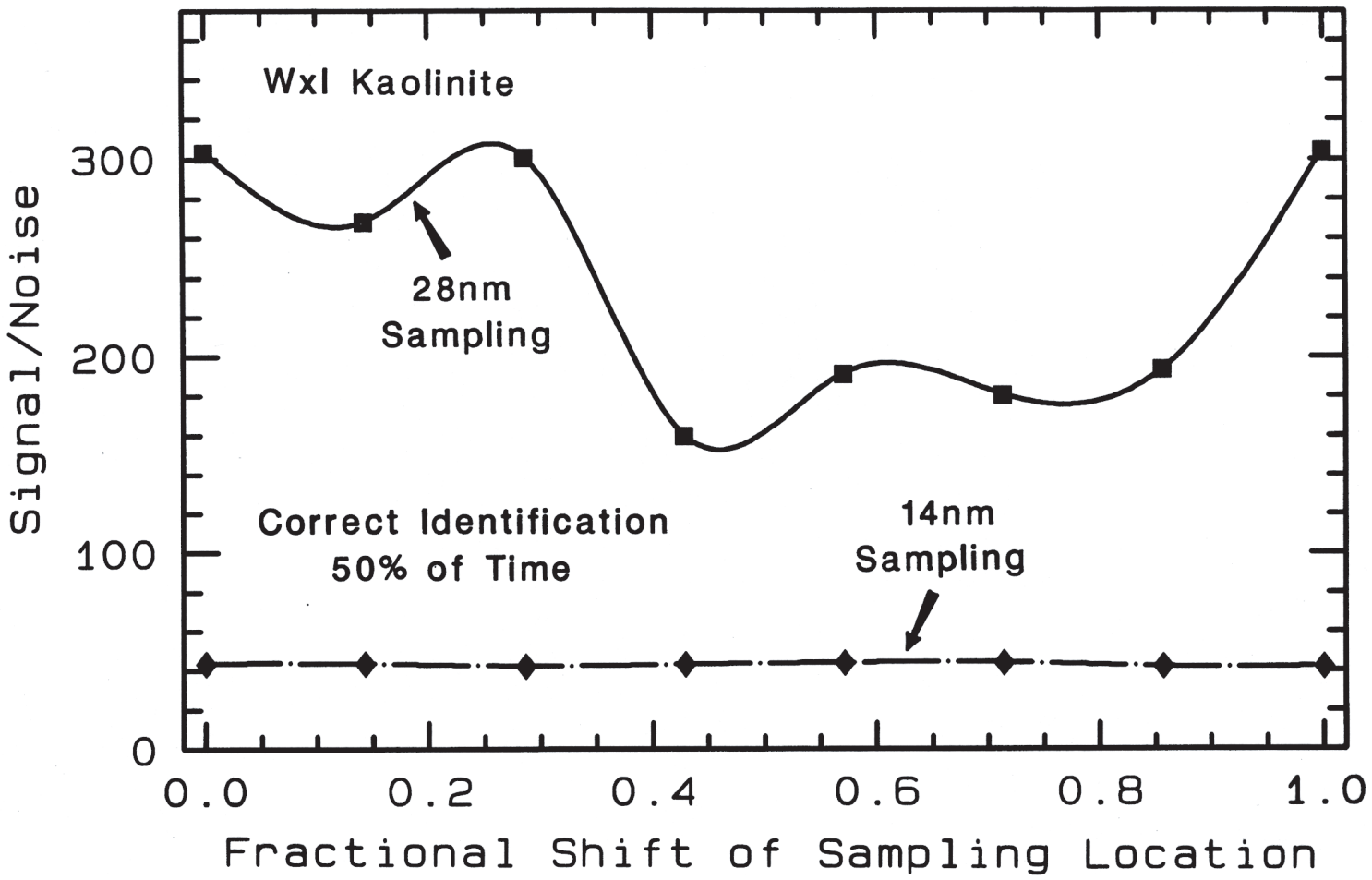

Figure 28. Signal-to-noise of identification values at the 50% correct level for noisy well-crystallized kaolinite test spectra convolved to 28 and 14 nm sampling intervals as a function of fractional shift of the sampling position. Upper curve sampling positions were shifted 4 nm for each successive set of noisy test spectra; bottom curve sampling positions were shifted 2nm. Note that "ringing" is almost non-existent in the lower curve.

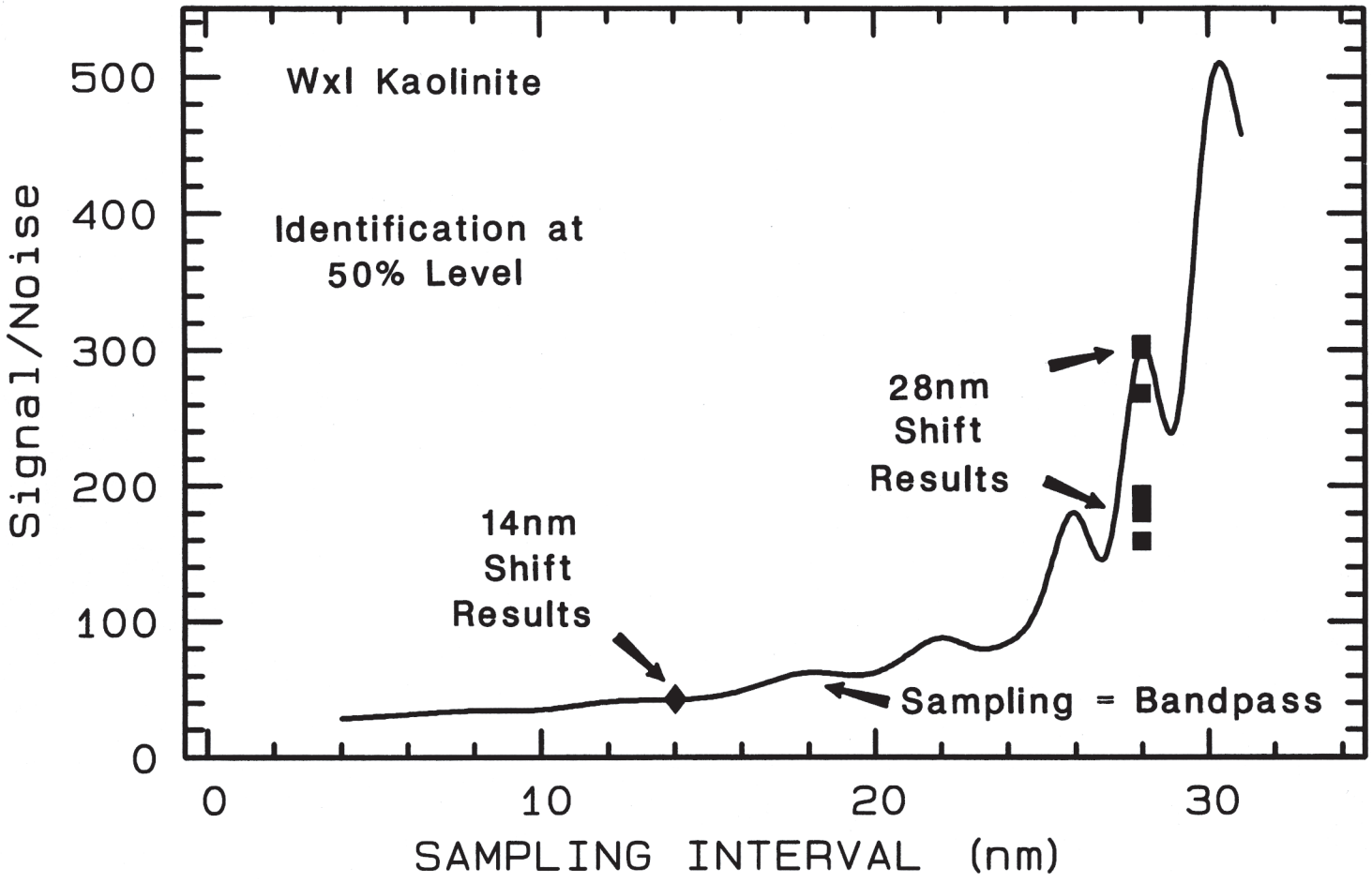

Figure 29. Signal-to-noise of identification values at the 50% correct level ($S/N_{ID50\%}$) from Figure 28 plotted on the well-crystallized kaolinite $S/N_{ID50\%}$ curve from Figure 26. Note that S/N_{ID} values of the14 nm spectra completely overlap and that the separation between S/N_{ID} values of the 28 nm spectra has the same amplitude as "ringing" in the S/N_{ID} curve.

6.2.2 Additional S/N_{ID} Curves

Signal-to-noise of identification curves for minerals with electronic absorptions (e.g., goethite and hematite) have gently inclined ramps with superimposed ringing (Figure 30). A likely explanation for this is that the broad Fe-absorptions are nearly fully resolved even at a BP and SI equal to 31 nm, so that spectrally oversampling them does not increase spectral detail or lower the S/N_{ID} significantly. Ringing in the goethite and hematite curves is probably related to spectral aliasing, but the amplitude is less than that in S/N_{ID} curves of minerals with narrow diagnostic absorptions. The S/N_{ID} curves for goethite and hematite have no identification walls over the SI range shown, but if they exist, they may occur at SI values broader than 31 nm. The identification wall for high temperature jarosite starts at 23 nm because this mineral's spectral features start to resemble those of other minerals at and beyond that SI value due to spectral undersampling of the narrow diagnostic Fe ligend-field absorption at 0.44 μm (natural FWHM = 21 nm; see Figure 2).

The FWHM of an absorption does depend on the spectral resolution used in the spectral measurement. However, the natural FWHM (NFWHM) is independent of spectral resolution and is the FWHM of a fully resolved absorption feature. Absorptions are fully resolved when subsequent narrowing of the BP and SI do not resolve more spectral details of an absorption. As a consequence, the NFWHM of an absorption is usually narrower than the FWHM of the same feature measured using broad BP and SI values. In this study, NFWHM refers to fully resolved absorptions.

In general, S/N_{ID} curves of minerals with vibrational absorptions steepen more rapidly than do S/N_{ID} curves of minerals with broader electronic absorptions as SI broadens (compare Figures 30 and 31). A likely explanation for this is that vibrational absorptions are narrower and measurements of them lose spectral detail at broad BP and SI values, where a relatively high S/N_{ID} is required for their identification. In the cases examined, S/N_{ID} curve ringing starts at about 16 nm. This is the critical BP and SI combination above which spectral aliasing becomes pronounced and above which the S/N_{ID} values start to drastically increase for minerals in the vibrational portion of the spectral library. Signal-to-noise of identification values at the 50% correct level for each of the four imaging spectrometers are plotted on the mineral $S/N_{ID50\%}$ curves at their respective SI positions (Figures 30 and 31).

6.3 Factors Controlling the Shape of S/N_{ID} Curves

Factors controlling the shape of S/N_{ID} curves can be inferred from the examples shown in Figures 25 through 31. As a general rule, the slope of a S/N_{ID} curve is controlled by the width of the material's diagnostic absorption features: wide absorptions have gently-inclined S/N_{ID} curves with no discernable identification wall and low amplitude ringing while narrow absorptions have steeply-inclined S/N_{ID} curves with well-defined identification walls and high amplitude ringing. Three factors determine the position of an identification wall as a function of *SI*. The first factor is the NFWHM of the diagnostic absorptions of a material. The wider the NFWHM of a diagnostic absorption, the broader the BP and SI can be before the identification wall is reached. In some cases, the position of an identification wall will be controlled in large measure by the NFWHM of the narrowest diagnostic spectral feature used for identification as was the case for

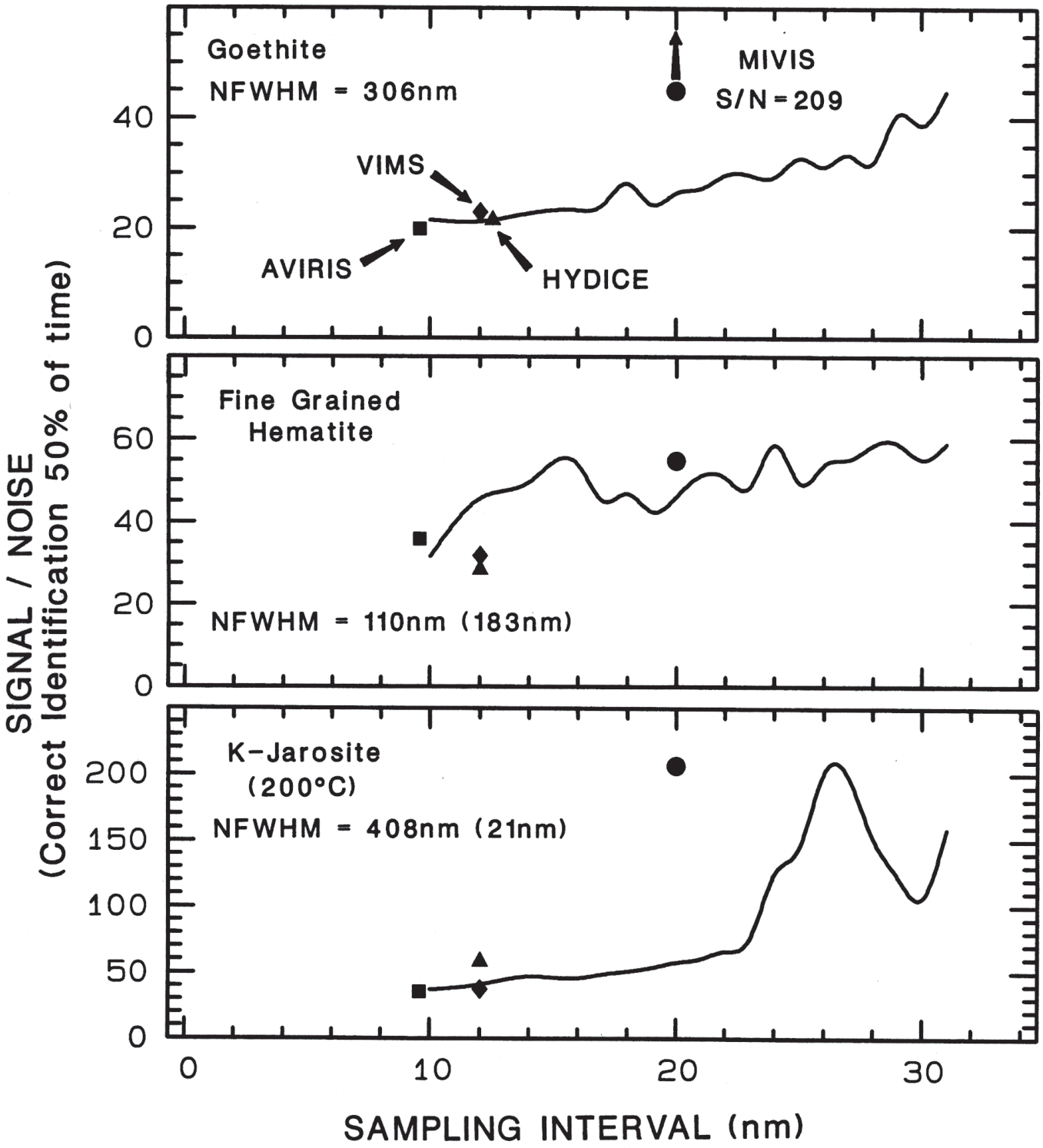

Figure 30. Signal-to-noise of identification curves at the 50% correct level ($S/N_{ID50\%}$) for minerals with absorptions in the electronic region. Test spectra were critically sampled. For each mineral, NFWHM is the natural full width half maximum of each absorption band measured from spectra collected at high spectral resolution. Numbers in parentheses are the NFWHM values of subordinate absorption bands. Symbols represent $S/N_{ID50\%}$ values for each imaging spectrometer. HYDICE and VIMS S/N_{ID} values plot below the hematite S/N_{ID} curve because of variations in the sampling intervals of these instruments which change over the wavelength range of the diagnostic hematite absorptions. MIVIS S/N_{ID} values plot above the S/N_{ID} curves for goethite, hematite, and K-jarosite because only the 0.48-µm absorption in each of these phases can be used for identification due to the 0.83 to 1.15 µm gap in MIVIS spectral coverage.

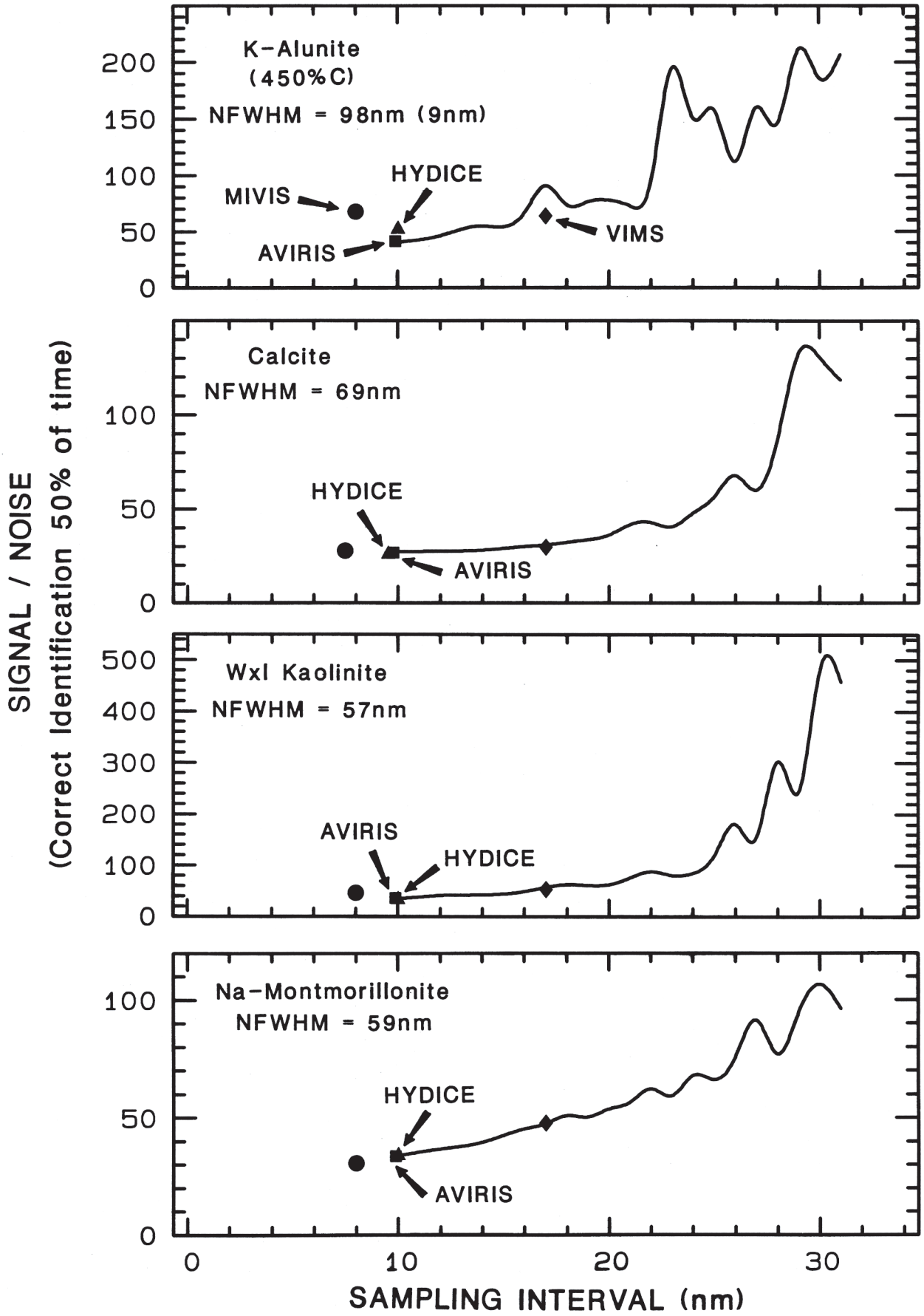

Figure 31. Signal-to-noise of identification curves at the 50% correct level ($S/N_{ID50\%}$) for minerals with absorptions in the vibrational region. Test spectra were critically sampled. See caption of Figure 30 for more details. For alunite the MIVIS S/N_{ID} value plots above the S/N_{ID} curve because this instrument's bandpass and sampling interval are too broad in the near-infrared to detect the diagnostic 1.48-μm alunite absorption.

jarosite.

The second factor is the level of spectral detail in the diagnostic absorptions of a material. Greater spectral detail enhances differentiation especially when absorptions of other materials occur at the same wavelength, but greater detail is easily lost when using broad SI values. In cases where materials with nearly identical spectral absorptions are being differentiated, the identification wall on their S/N_{ID} curves will occur at narrow BP and SI values. Consequently, narrow BP and SI values must be used in addition to high S/N to differentiate materials in these cases.

The third factor is the wavelength position and shape of the diagnostic absorptions of a material relative to those of other materials. The more nearly unique an absorption is, the less likely it will be confused with other absorptions, causing the identification wall to occur at relatively broad BP and SI values.

While the S/N_{ID} curves were derived using Tetracorder, we predict that other identification algorithms will produce S/N_{ID} curves of similar shape, though the position of the identification wall and onset of ringing could be shifted compared to those derived here.

6.4 S/N_{ID} Curves: When Bandpass is Broader and Narrower than the Sampling Interval

The shapes of S/N_{ID} curves were examined for cases where BP was a multiple of the SI for well-crystallized kaolinite (Figure 32). The S/N_{ID} curves with BP greater than the SI, plot progressively above the BP = 1 SI curve. The base of the identification walls and the onset of ringing also shift to narrower SI values, with amplitude of ringing increasing as BP broadens relative to the SI. This behavior is consistent with the observation that spectral aliasing increases as spectral features begin to resemble each other, as happens at broader bandpasses. Note that most of the S/N_{ID} curves are relatively flat from 4 to 16 nm, indicating that identification is relatively independent of BP over this SI range for BP $\leq$ 4 SI. Apparently, enough spectral detail exists, even at a BP four times the SI, to correctly identify kaolinite test spectra, though at a slightly higher S/N. It is apparent from these curves that the spectral identification of kaolinite is more adversely affected by increases in SI than by comparable increases in BP.

A distinction can be made between spectrally sampling a spectrometer's optical signal and sampling a material's spectral absorptions. Although most imaging spectrometers critically sample spectra (one sample per bandpass), the spectrometers do an adequate job of measuring the spectral absorptions of most materials because they sample the relatively broad absorptions of materials at Nyquist or better sampling rates.

6.5 Shape of S/N_{ID} Curves at the 90% Correct Level

Spectrally identifying a material at the 90% correct level may be the only way to achieve the certainty necessary for some remote-sensing applications such as mineral exploration, planetary landing-site evaluations, reconnaissance missions, and product quality assurance. With these more demanding applications in mind, kaolinite S/N_{ID} curves were calculated for the 90% correct level to examine the effects of ringing and S/N_{ID} required to achieve this higher level

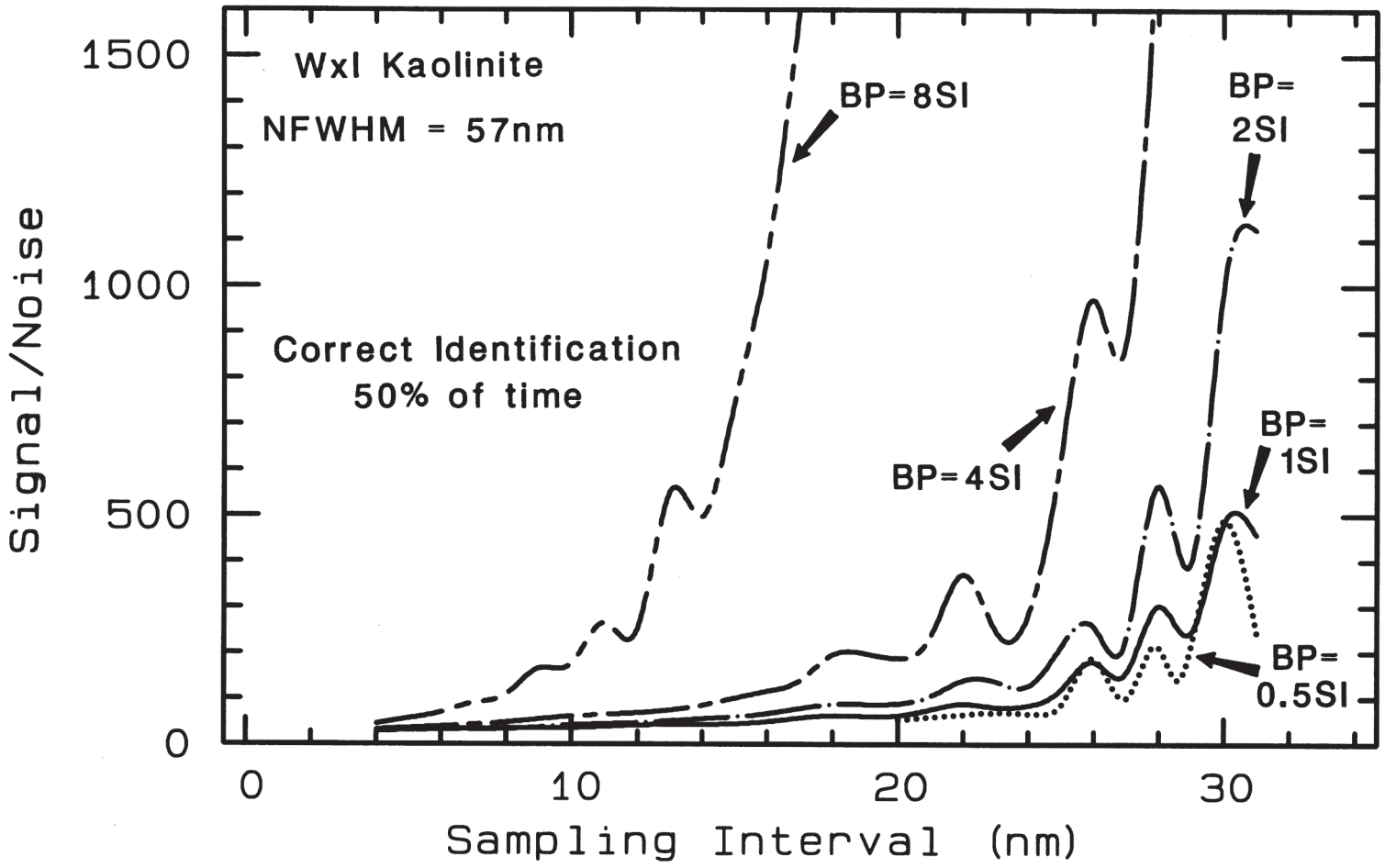

Figure 32. Signal-to-noise of identification (S/N_{ID}) curves for well-crystallized kaolinite for bandpasses 0.5, 1 (critical sampling), 2 (Nyquist sampling), 4, and 8 times the sampling interval at the 50% correct level. Note that the base of the identification walls shift to narrower sampling intervals and ringing intensifies as bandpass broadens. Overlap between the dotted curve (which begins at 20 nm) and the solid curve is likely caused by spectral aliasing in the undersampled spectra used to calculate S/N_{ID} values of the dotted curve.

of accuracy. Figure 33A shows both the 90% and 50% correct level S/N_{ID} curves for kaolinite when the BP is equal to the SI. Detectable ringing starts at about 16 nm in both curves, but the amplitude is significantly greater in the 90% curve. Consequently, the relatively flat portions of the S/N_{ID} curves, which are the most useful portions for spectral identification, contract toward narrow SI values as the need for accuracy increases. In addition, a higher S/N is required to achieve 90% accuracy in spectral identification with the S/N_{ID} increasing precipitously at broad BP and SI values when compared to the 50% curve. The 90% curve requires approximately double the S/N of the 50% curve before the identification wall, and as much as six times the S/N of the 50% curve beyond the identification wall. Clearly, the task of spectrally identifying materials to a high degree of certainty is much more difficult at BP and SI values beyond the identification wall of a given material. Figure 33B shows the 90% curves for kaolinite at bandpasses 1, 2, and 4 times the SI. As the BP broadens relative to the SI, the identification walls shift to narrower SI values and the amplitude of ringing increases. Ringing appears to grow exponentially.

6.6 Concept of a S/N_{ID} Surface

The S/N_{ID} curves for the identification of wxl kaolinite, shown in Figure 32, can be used to construct a 3-dimensional surface as a function of BP, SI, and S/N by interpolating S/N_{ID} values between the curves (Figure 34). For a given BP and SI combination, this surface defines the S/N required to correctly identify wxl kaolinite 50% of the time. Identification accuracy is greater than 50% for S/N values above this surface and less than 50% for S/N values below the surface. Ridges are parallel to the BP axis and their locations are controlled by spectral aliasing induced by changes in the SI. It is interesting that ringing persists even for narrow sampling at very broad BP values. Increasing the BP alone will not cause ringing as indicated by the smooth S/N_{ID} curve in Figure 25. The flat area of the 3-D surface encompasses the BP and SI combinations requiring the lowest S/N for spectral identification of wxl kaolinite. The overall shape of S/N_{ID} surfaces of other materials will undoubtably resemble that of kaolinite although they will differ in detail.

6.7 Imaging Spectrometer Design: the S/N for Sampling Interval Tradeoff

Is it worth broadening the SI to increase the S/N of a grating or prism spectrometer? The required S/N_{ID} concept can help answer this question by providing a method to calculate the optimum tradeoff between S/N and SI. First, the relationship between S/N and BP will be considered as it can be used to help determine the best BP and SI combination for spectral identification. In brief, keeping the BP narrow, without changing the light throughput to the focal plane, minimizes the required S/N_{ID} (as seen in Figure 25), preserves spectral details, and does not decrease the amount of signal incident on the detector elements in an array system. The narrowest BP attainable in a grating or prism spectrometer is limited by the spectral width of the detector elements, which is effectively equal to the SI (e.g., see the detector limited critical sampling case in Figure 3), therefore a critically sampling BP and SI combination minimizes the required S/N_{ID} and is the most effective array detector sampling configuration for spectral identification.

Just as we have defined a required S/N_{ID} curve we can likewise define an achievable S/N

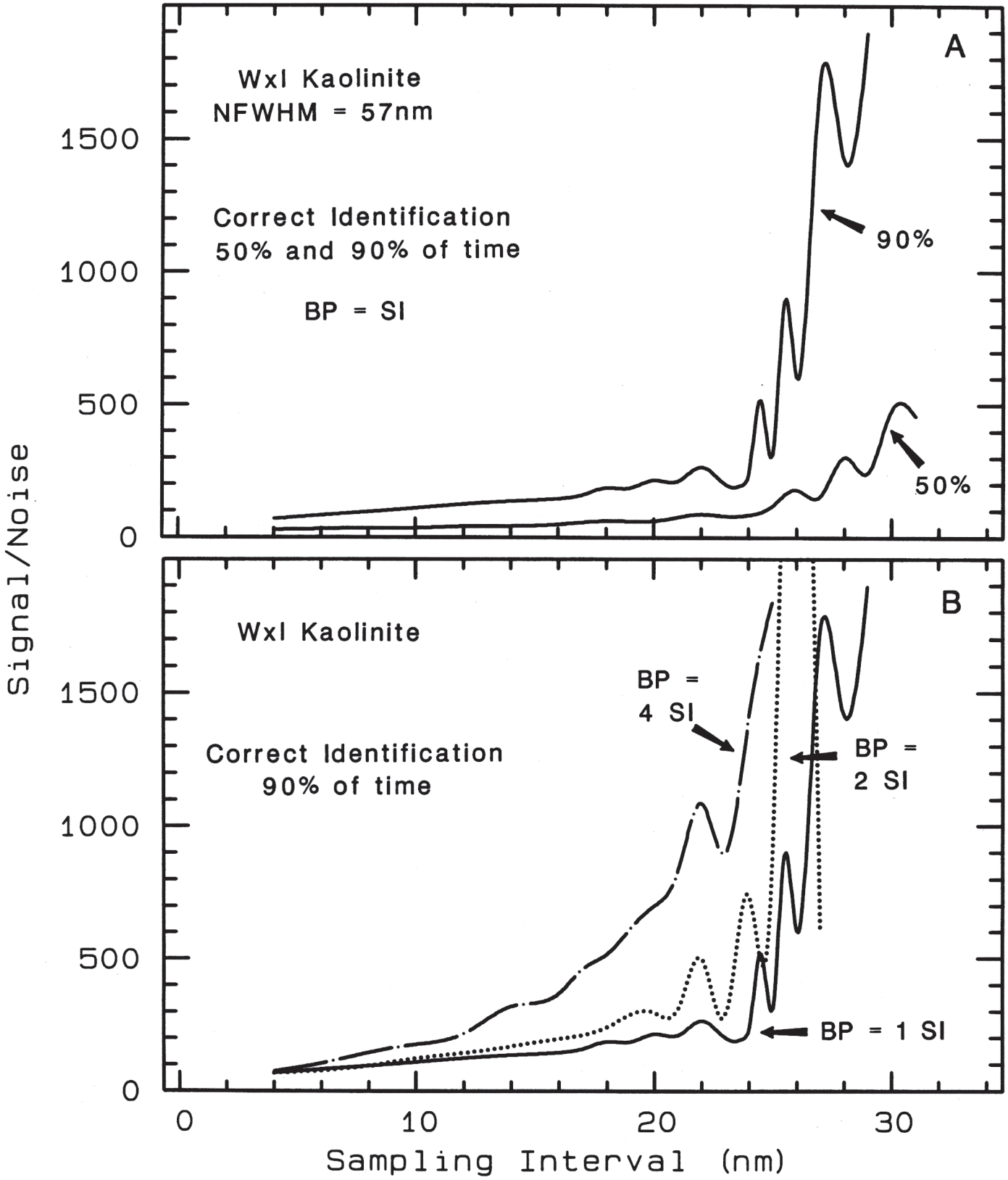

Figure 33. A) Signal-to-noise of identification curves for the 50% and 90% correct levels for well-crystallized kaolinite. Test spectra were critically sampled. B) Signal-to-noise of identification curves (S/N_{ID}) at the 90% correct level for well-crystallized kaolinite using test spectra with bandpasses equal to 1, 2, and 4 times the sampling interval (SI). Note that the curves are vertically separated at narrow bandpass (BP) and SI values and that the amplitude of "ringing" at 26 nm is greater than the overall height of the identification wall for the BP = 2 SI curve. On the BP = 2 SI curve, a 1 nm broadening of the SI increases the S/N_{ID} by an order of magnitude where $S/N_{ID} = 720$ at 25 nm and $S/N_{ID} > 7200$ at 26 nm.

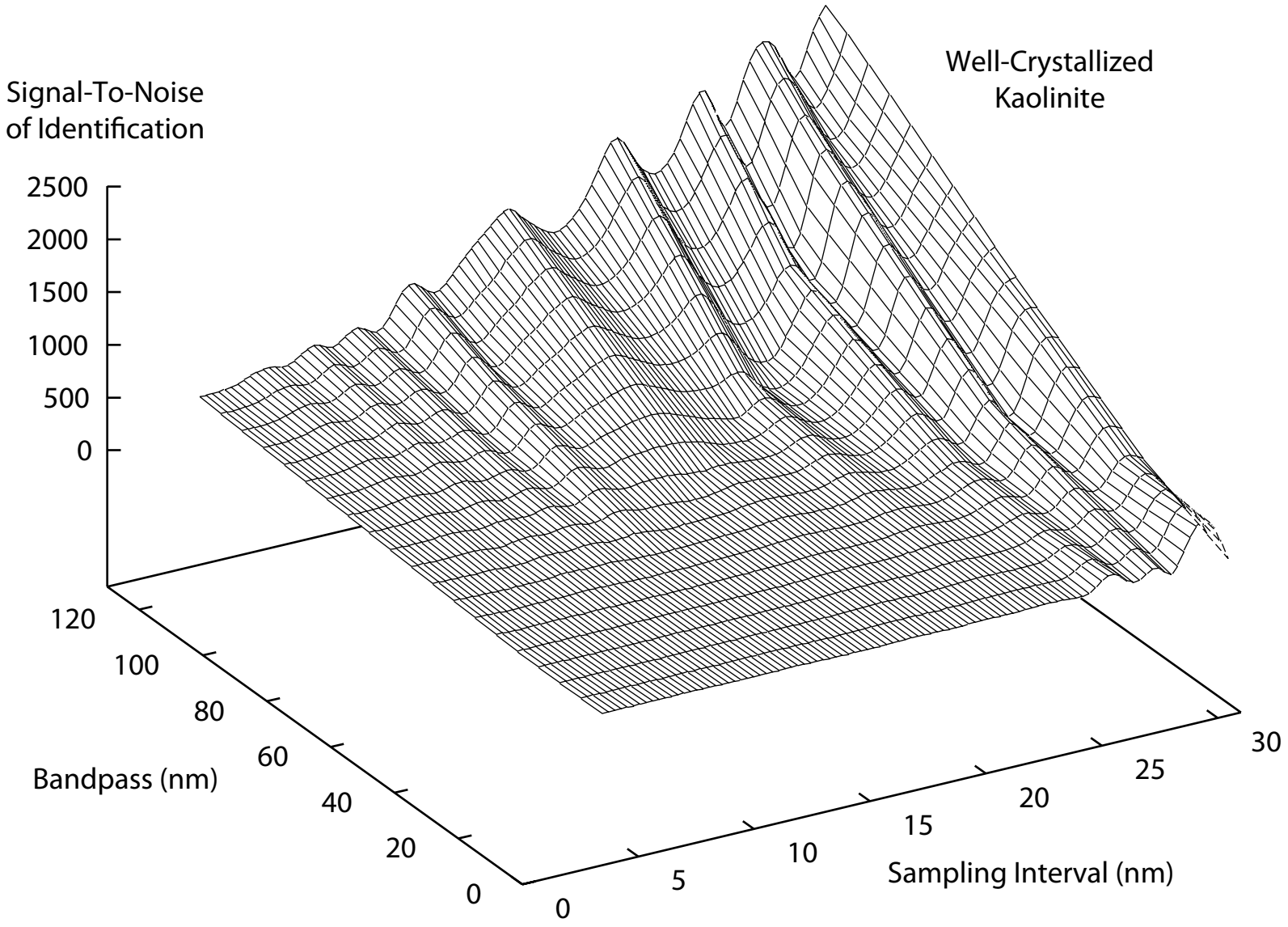

Figure 34. Signal-to-noise of identificationsurface for well-crystallized kaolinite at the 50% correct level as a function of bandpass and sampling interval. Test spectra were critically sampled.

curve as the range of S/N values that can be achieved, given a constant light throughput to the focal plane and fixed grating (or prism) configuration, by only varying the SI of the detector array when SI is equal to the detector size. Because critical sampling is best for identification, only the achievable S/N curve for BP = SI need be defined. Theoretically, the variation of S/N as a function of SI ranges between two extremes: that described by a photon-noise-limited system where S/N is proportional to the $\sqrt{SI}$, and that described by a detector-noise-limited system where S/N is directly proportional to the SI. The S/N in actual grating and prism spectrometers varies somewhere between these extremes depending to a large extent on the albedo of the target surface and incident light levels: bright surfaces may cause the system to behave more photon noise limited and dark surfaces cause the system to behave more detector noise limited.

Directly comparing achievable S/N and required S/N_{ID} curves is difficult due to ringing of the S/N_{ID} curve caused by spectral aliasing. A way to overcome this difficulty involves using the mean of the S/N_{ID} curve which is free from ringing. Figure 35 shows that a mean can be estimated by averaging the lower and upper tangential bounds of the S/N_{ID} curve for wxl kaolinite. Once a mean S/N_{ID} curve is estimated then it can be more easily compared with achievable S/N curves for both photon- and detector-noise-limited systems (Figure 36). Because we are interested in the relative change of achievable S/N, not its absolute magnitude, as the SI broadens, we can arbitrarily tie the achievable S/N curve levels to a reference point anywhere along the required S/N_{ID} curve. Choosing a reference point at the low end of the S/N_{ID} curve effectively sets the achievable S/N equal to the level of the required S/N_{ID} at that point allowing us to evaluate the tradeoff between achievable and required S/N values as the SI broadens.

Both achievable curves remain above the required curve out to 18.5 nm for the photon case and out to 27 nm for the detector case; beyond these points the achievable S/N curves are overwhelmed by the rapid increase of the required S/N_{ID} curve. The goal is to find the optimum SI values where the achievable S/N values are largest relative to the required S/N_{ID} values. This can be accomplished by dividing the achievable S/N curves by the mean S/N_{ID} curve thereby producing two convex upward curves (not shown) whose maximum values are at SI = 10.7 nm for the photon-noise-limited system and SI = 14.3 nm for the detector-noise-limited system at the 50% correct level (Figure 36). Choosing non-optimum SI values for either system will result in a lower level of identification accuracy than is possible at the optimum SI values.

The optimum SI values can be plotted as a function of the percent correct identification level for wxl kaolinite (Figure 37). In a photon-noise-limited system the optimum SI moves toward narrower values as the need for accuracy in spectral identification increases. In a detector-noise-limited system the optimum SI remains nearly constant even as the need for accuracy increases. Apparently the accuracy of Tetracorder, while using the photon system, is more sensitive to the width of the SI and less sensitive to the relatively small increases in S/N achieved by broadening the SI, whereas the accuracy of Tetracorder, while using the detector system, is less sensitive to the width of the SI and more sensitive to the relatively large increases in S/N achieved by broadening the SI in that system. As can be seen in Figure 37, the ratio of achievable / required S/N is nearly 1.0 above the 60% correct level (on the horizontal axis) in the photon system indicating that *SI* should not be traded for increased S/N in a photon-noise-limited

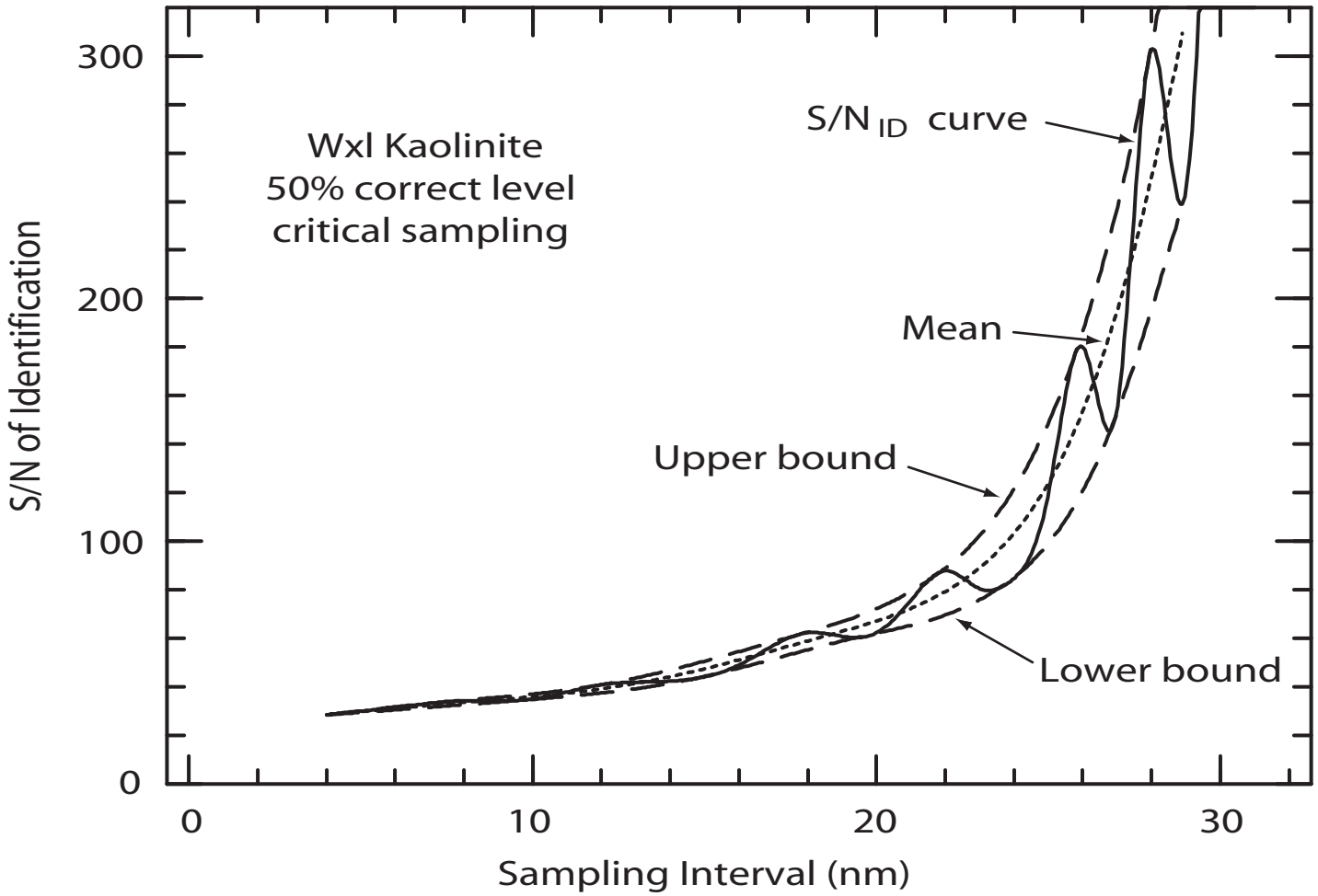

Figure 35. Signal-to-noise of identification (S/N_{ID}) curve for well-crystallized kaolinite at the 50% correct level and critical sampling bounded by upper and lower curves (dashed) drawn tangential to the oscillations caused by spectral aliasing. Because the locations of peaks and troughs on the S/N_{ID} curve depend on the wavelengths at which the kaolinite spectra were sampled (e.g., as demonstrated in Figures 24 to 26) the bounding curves theoretically encompass all possible values of the S/N required for identification. The mean S/N_{ID} curve (dotted) can be estimated by taking the average of the upper and lower bounding curves.

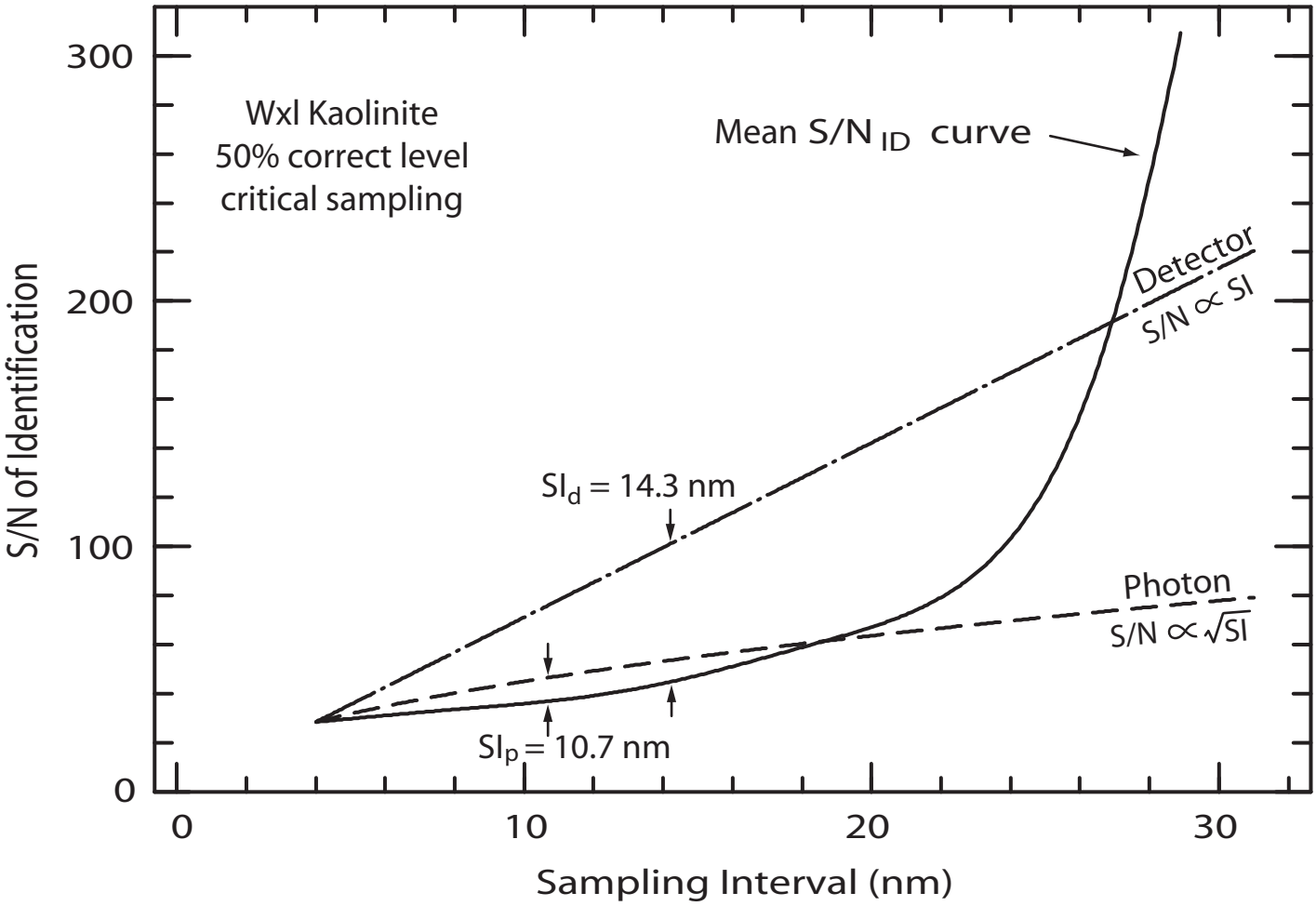

Figure 36. Dividing the achievable signal-to-noise ratio (S/N) curves for a photon-noise-limited system (dashed curve) and a detector-noise-limited system (dash - dotted curve) by the mean signal-to-noise of identification (S/N_{ID}) curve for well-crystallized kaolinite at the 50% correct level results in curves whose maximum values are the optimum sampling interval (SI) values for photon (SI_p) and detector (SI_d) noise limited systems. The S/N is proportional to the $\sqrt{SI}$ in a photon-noise-limited system and directly proportional to the SI in a detector-noise-limited system. The positions of the photon and detector achievable curves are not absolute. The S/N in a photon-noise-limited system is always greater than in a detector-noise-limited system.

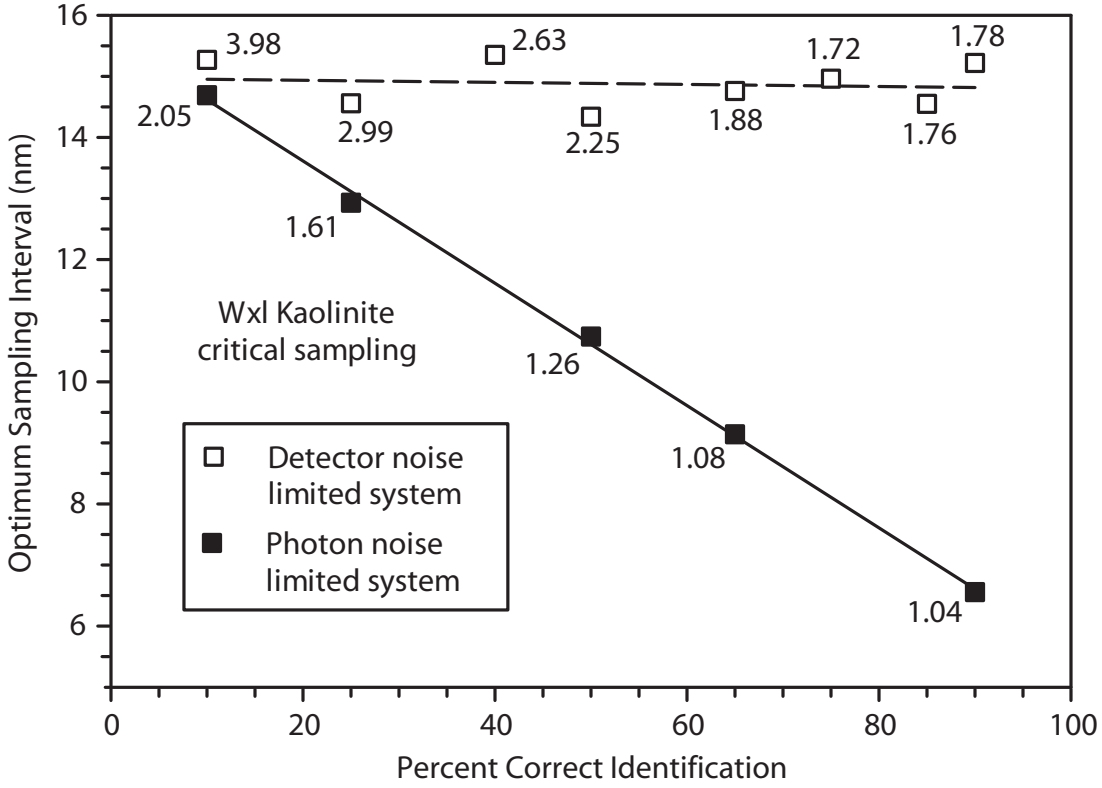

Figure 37. Optimum sampling interval (SI) values for both photon(SI_p) and detector (SI_d) noise limited systems as a function of percent correct identification for well-crystallized kaolinite determined using the technique shown in Figure 36. The solid line is best fit to the photon-noise-limited data described by: optimum SI_p = ((% correct * -0.1001) + 15.62) with r^2 = 0.998. The dashed line is best fit to the detector-noise-limited data described by: optimum SI_d = ((% correct * -0.001707) + 14.97) with r^2 = 0.017. This low r^2 value shows that the optimum sampling interval for the detector case is relatively independent of the percent correct identification level. Greater scatter in the detector-noise-limited data is due to the relatively larger magnitude of spectral alias ringing at higher SI values resulting in greater uncertainty in estimates of the mean signal-to-noise of identificationcurve. Numbers by each symbol indicate the ratio of achievable / require S/N.

system when high levels of accuracy are desired. The ratio of achievable / require S/N also decreases as the need for accuracy increases in the detector system but not to the same degree as in the photon system indicating that it is still worth trading SI for S/N in a detector-noise-limited system even when high levels of accuracy are desired provided the optimum SI calculated is narrower than that at the base of the identification wall.

Optimum SI values can also be calculated for other minerals and plotted as a function of the wavelength position of their diagnostic absorptions (Figure 38). Spectra of kaolinite, montmorillonite, and calcite have only one diagnostic absorption, whereas those of jarosite, hematite, and alunite have two diagnostic absorptions each. Because we do not know which of the absorptions in a mineral with two diagnostic absorptions has the most influence on the optimum SI determined for that mineral, we have assigned the same optimum SI to the wavelength position of each absorption. Although goethite has two diagnostic absorptions, we only used one for spectral identification in this study.

The narrowest optimum SI value in a given wavelength region can be used to define optimum SI profiles (top and bottom boundaries of the gray area in Figure 38). This concept can be used to design efficient spectrometers. The narrowest optimum SI in the profile would determine the actual SI of the array detector and the profile would be used as a guide by onboard processing software to co-add signals from adjacent detector elements to achieve the desired optimum SI for a given wavelength region, thus maximizing identification accuracy while reducing the volume of imaging data. In cases where atmospheric gases are being studied or their spectral signatures need to be removed from remote sensing data, spectral mapping will require the use of a SI narrow enough to allow differentiation between diagnostic gas absorptions, and thus this SI may become the actual SI of the spectrometer. If the optimum SI profile shown in Figure 38 were used to co-add signals from adjacent detector elements using the optimum SI for kaolinite as the actual SI, there would be nearly a 15% data reduction, relative to just using the actual SI, for both the photon- and detector-noise-limited systems according to:

$$\% \textit{ Reduction of data volume } = 100 - \left[\frac{\Sigma SI_{act}}{\Sigma SI_{pro}} * 100 \right] \tag{4}$$

where for each spectrometer channel SI_{act} is the actual SI and SI_{pro} is the optimum SI from the profile. This concept can be used to custom design a spectrometer for a specific mission by calculating an optimum SI profile at an acceptable percent correct level for all the materials and mixtures likely to be encountered during the mission with the flexibility to modify the SI profile as needed.

7.0 CONCLUSIONS

This study has explored the relationship between detector bandpass (BP), sampling interval (SI), and signal-to-noise ratio (S/N) for the identification of materials using reflectance

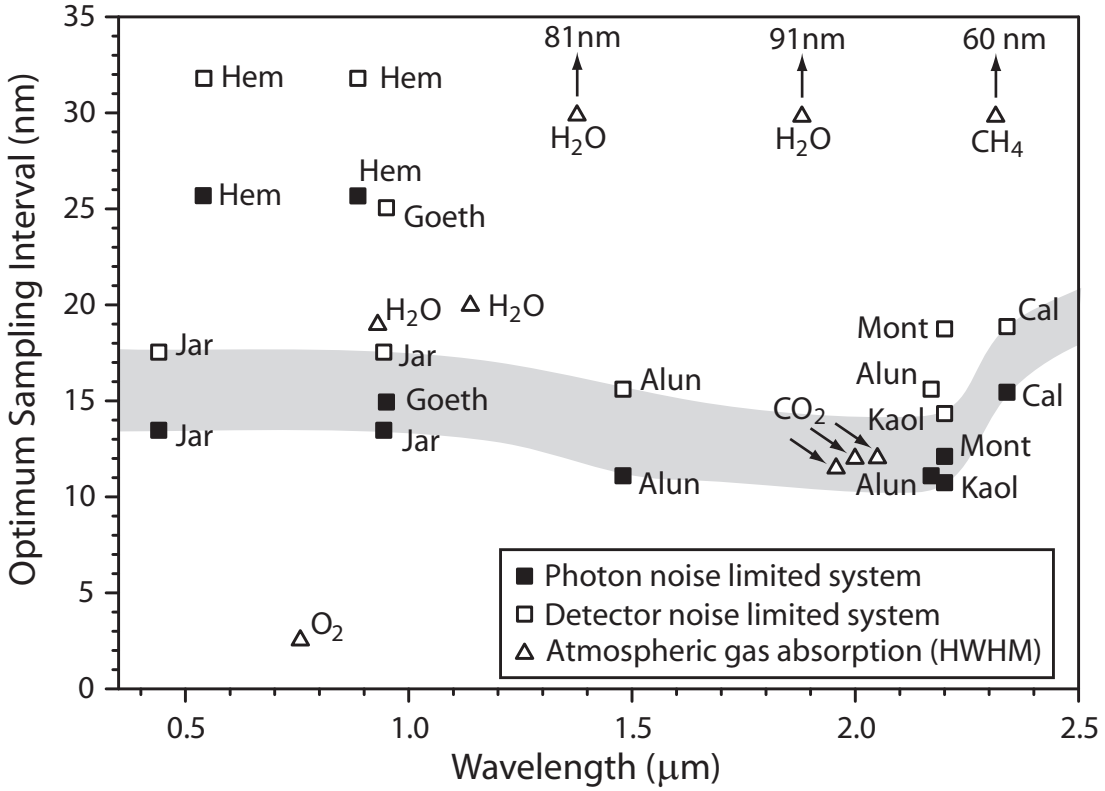

Figure 38. Optimum sampling interval (SI) values for photon- and detector-noise-limited systems at the 50% correct identification level versus wavelength positions for the diagnostic spectral absorptions used for identification of seven alteration minerals. The gray zone's lower boundary is the minimum optimal SI for identification of the minerals as a function of wavelength for a photon-noise-limited system. The gray zone's upper boundary is the minimum optimal SI for a detector-noise-limited system. Triangles mark wavelength positions and Half-Width-Half-Maxima (HWHM) of terrestrial atmospheric gas absorptions; the locations of the triangles do not necessarily depict the optimum SI values for identification of these gases. Arrows above H_2O and CH_4 triangles indicate that the HWHM values of absorptions from these gases at these wavelengths are beyond the upper bound of the plot at the specified SI values. Jar = jarosite; Hem = hematite; Goeth = goethite; Alun = K-alunite; Kaol = well-crystallized kaolinite; Mont = Na-montmorillonite; Cal = calcite.

spectroscopy from 0.4 - 2.5 μm. Findings can be summarized as follows:

1) The spectral absorptions of a material can be distinguished from similarly shaped absorptions of other materials at the same wavelengths positions, but in general, the accuracy of identifications diminishes as the S/N decreases and the BP and SI broaden. Broad band sensors like TM, ASTER, and MODIS have SI values well beyond that required for identification of many materials thus limiting their differentiating capability to only a few broad groups of materials.

2) Use of reference spectra with weak subordinate absorptions or saturated absorptions with low reflectance levels can impede spectral identification unless the S/N of the spectral data is high enough to preserve sufficient spectral detail in these bands to aid in the identification process.

3) The S/N required for spectral identification of a material (S/N_{ID}) increases linearly as BP and SI increase but then it sharply increases in a non-linearly way above a BP and SI threshold creating an identification wall. For materials with narrow diagnostic absorptions, this identification wall becomes nearly vertical as the SI approaches the width of the material's absorptions, indicating that high (perhaps infinite) S/N is required for identification at broad BP and SI values. Ringing caused by spectral aliasing starts on the S/N_{ID} curves, at the nearly-flat base of the identification wall, when the wavelength locations of the detector channels move out of phase with the positions of diagnostic absorption features as the SI broadens.

4) The slope of a S/N_{ID} curve is controlled by the width of a material's diagnostic absorptions: wide absorptions give rise to gently inclined S/N_{ID} curves with no discernable identification walls and low amplitude ringing while narrow absorptions give rise to steeply inclined S/N_{ID} curves with abrupt identification walls and high amplitude ringing.

5) There are BP and SI combinations beyond which spectral identification of materials requires an abrupt increase in sensor S/N, due to spectral aliasing – a condition where absorption features of different materials can resemble one another.

6) Factors that control the position of the identification wall on the S/N_{ID} curve of a material are the uniqueness of its diagnostic absorptions in terms of shape and wavelength isolation, the bandpass at which the material is measured, and the spectral diversity of materials in nature and in the spectral library used for spectral comparisons. The more isolated a material's spectral absorptions are in wavelength relative to absorptions of other materials, the broader the BP and SI values will be at which that materials's ringing and identification wall start. As a material's diagnostic absorptions are diluted or obscured by unrelated absorptions when other materials are added, the SI value where the identification wall and ringing begin may be considerably narrower than for the pure material.

7) Because the narrowest BP attainable in a grating or prism spectrometer is limited by the spectral width of the detector elements, which is effectively equal to the SI, a critically sampling BP and SI combination (where BP = SI) minimizes the required S/N_{ID} and is the most effective

array detector sampling configuration for spectral identification.

8) The flat region of a S/N_{ID} curve, which encompasses the most useful BP and SI combinations for spectral identification, contracts toward narrower SI values as the need for identification accuracy increases.

9) Sensor S/N is more critical for identification in the flat region of a S/N_{ID} curve because in this region small increases in S/N significantly boost the accuracy of spectral identification. The SI is more critical for identification in the steep region of the S/N_{ID} curve (e.g., at and beyond the identification wall) because broadening the SI can induce ringing which dramatically increases the S/N_{ID}. The BP is less critical than the SI and S/N because broadening it does not induce ringing and only gradually increases the S/N_{ID}.

10) It may not always be beneficial to broaden the SI to achieve a higher S/N. Optimum SI values can be calculated for the spectral identification of materials that balance the tradeoff of SI for S/N. Dividing the achievable S/N curve by the required S/N_{ID} curve for a particular material gives a curve whose maximum value is the optimum SI value for identification of that material. This calculation can be done for photon- and detector-noise-limited spectrometer systems.

11) The accuracy of spectral identifications is more sensitive to the width of the SI and less sensitive to the relatively small increases in S/N achieved by broadening the SI when using a photon-noise-limited spectrometer system (assuming a constant light throughput to the focal plane and fixed grating or prism configuration), whereas the opposite is true for a detector-noise-limited system. The SI should not be traded for increased S/N in a photon-noise-limited system when high levels of accuracy are desired, but it is worth trading SI for S/N in a detector-noise-limited system even when high levels of accuracy are desired provided the optimum SI calculated is narrower than that at the base of the identification wall. Table 5 shows the tradeoffs between parameters modeled in this study.

12) It is possible to select optimum BP-SI-S/N combinations for a particular remote sensing application during the design phase of a spectrometer. This involves plotting the optimum SI values for all the materials and mixtures likely to be encountered during a mission. The narrowest optimum SI values in this plot would define a profile that would be used by onboard processing software to co-add signals from adjacent detector elements in each wavelength region, thus maximizing identification accuracy while minimizing the volume of imaging data.

While this study has explored the relations between parameters controlling our ability to discriminate pure materials with spectroscopy, additional studies are need to examine the subtleties of spectral identification of mixtures and to compare the S/N_{ID} performance of Tetracorder with that of other identification algorithms.

Table 5. Tradeoffs between spectral parameters modeled in this study.

Bp	SI	S/N_{ID}	S/N_A*	$ID^{\dagger}_{accuracy}$ Photon	$ID^{\dagger}_{accuracy}$ Detector	Comment
If ↑ and	— then ↑		—	↓	↓	
↓	—	↓	—	↑	↑	1
—	↑	↑	↑	↓	↑	2, 3
—	↓	↓	↓	↑	↓	4
↑	↑	↑	↑	↓	↑	2, 3
↓	↓	↓	↓	↑	↓	1, 4
If ↑ and	↓ and	↑ then	↓	↓	↓	
↑	↓	↓	↓	↑	↓	4
↓	↑	↑	↑	↓	↑	1, 2, 3
↓	↑	↓	↑	↑	↑	1, 2, 3, 5

BP = bandpass; SI = sampling interval; S/N_{ID} = SIGNAL-TO-NOISE OF IDENTIFICATION.
S/N_A = achievable signal-to-noise; $ID_{accuracy}$ = Identification accuracy.
Photon = photon noise limited system; Detector = detector noise limited system.
↑ = increase; ↓ = decrease; — = no change.
[1] BP cannot be < SI (for grating or prism spectrometers).
[2] Valid if SI is not broadened beyond that at the base of the *identification wall*.
[3] Valid if SI moves toward optimum SI for detector noise limited system.
[4] Valid if SI moves away from optimum SI for detector noise limited system.
[5] Valid if SI moves toward optimum SI for photon noise limited system.
*Assumes a constant optical and grating (or prism) configuration.
†$ID_{accuracy}$ for photon noise limited system is always > detector noise limited system.
All cases assume spectral width of detectors is equal to the SI with 100% fill factor.

8.0 ACKNOWLEDGMENTS

The analytical approach used in this study was significantly refined and the performance of the USGS Tetracorder algorithm greatly improved from synergy during the decade of their co-development. This study also benefitted greatly from reviews by Sue Kropschot, Paul Lucey, Amanda Warner, Betina Pavri, Fred Kruse, Jim Crowley, Ray Kokaly, Brad Dalton, Ilaria Longhi, Maria Sgavetti, and an anonymous reviewer. Eric Livo, Trude King, and Andrea Gallagher provided resources and assistance. AVIRIS data were graciously supplied by the AVIRIS team at the Jet Propulsion Laboratory. Funding was provided by the USGS Rock Spectra and Remote Sensing Projects and NASA planetary program W15805 (R. Clark, PI).

9.0 REFERENCES

Abrams, M.J., R.P. Ashley, L.C. Rowan, A.F.H. Goetz, and A.B. Kahle, Mapping of hydrothermal alteration in the Cuprite mining district, Nevada using aircraft scanner images for the spectral region 0.46-2.36 μm, *Geology*, *5*, 713-718, 1977.

Ashley, R.P., and M.J. Abrams, Alteration mapping using multispectral images - Cuprite mining district, Esmeralda County, Nevada, *U.S. Geological Survey Open-File Report 80-367*, 17 pp., 1980.

Basedow, R.W., D.C. Carmer, and M.E. Anderson, HYDICE System, implementation and performance, *Proceedings of the International Society for Optical Engineering (SPIE), 248*, 258-267, 1995.

Bianchi, R., and C.M. Marino, CNR LARA project, Italy: MIVIS/MIDAS environmental airborne hyperspectral remote sensing system: *Proceedings of the First International Airborne Remote Sensing Conference and Exhibition*, Strasbourg, France, Sept. 11-15, 1994, vol. III, pub. by Environmental Research Institute of Michigan (ERIM), 1994.

Birk, R.J, and T.B. McCord, Airborne hyperspectral sensor systems, 47th National Aerospace and Electronics Conference, Dayton, OH, May 23-27, 8 pp., 1994.

Boardman, J.W., Using dark current data to estimate AVIRIS noise covariance and improve spectral analyses, Summaries of the Fifth Annual JPL Airborne Earth Science Workshop, ed. R.O. Green, *Jet Propulsion Laboratory Publication 95-1*(1), 19-22, 1995.

Brown, R.H., K.H. Baines, G. Bellucci, J.-P. Bibring, B.J. Buratti, E. Busoletti, F. Capaccioni, P. Cerroni, R.N. Clark, A. Corandini, D.P. Cruikshank, P. Drossart, V. Formisano, R. Jaumann, Y. Langevin, D.L. Matson, T.B. McCord, V. Mennella, E. Miller, R.M. Nelson, P.D. Nicholson, B. Sicardy and C. Sotin, The Cassini Visual and Infrared Mapping Spectrometer investigation, *Space Science Reviews*, submitted.

Chrien, T.G., M. Eastwood, R.O. Green, C. Sarture, H. Johnson, C. Chovit, and P. Hajek, Airborne Visible/Infrared Imaging Spectrometer (AVIRIS) onboard calibration system, Summaries of the Fifth Annual JPL Airborne Earth Science Workshop, ed. R.O. Green, *Jet Propulsion Laboratory Publication 95-1*(1), 31-34, 1995.

Clark, R.N., Spectral properties of mixtures of montmorillonite and dark carbon grains: Implications for remote sensing minerals containing chemically and physically adsorbed water, *J. Geophys. Res.*, *88*, 10635-10644, 1983.

Clark, R.N., Chapter 1: Spectroscopy of rocks and minerals and principles of spectroscopy, in

Manual of Remote Sensing, ed. A.N. Rencz, John Wiley and Sons, New York, 3-58, 1999.

Clark, R.N., and T. Roush, Reflectance spectroscopy: quantitative analysis techniques for remote sensing applications, *J. Geophys. Res.*, *89*, 6329-6340, 1984.

Clark, R.N., A.J. Gallagher, and G.A. Swayze, Material absorption band depth mapping of imaging spectrometer data using a complete band shape least-squares fitting with library reference spectra: Proceedings of the Second Airborne Visible/Infrared Imaging Spectrometer (AVIRIS) Workshop, ed. R.O. Green, *Jet Propulsion Laboratory Publication 90-54*, 176-186, 1990a.

Clark, R.N., T.V.V. King, M. Klejwa, G.A. Swayze, and N. Vergo, High spectral resolution reflectance spectroscopy of minerals, *J. Geophys. Res.*, *95*, 12653-12680, 1990b.

Clark, R.N., G.A. Swayze, A.J. Gallagher, N. Gorelick, and F. Kruse, Mapping with imaging spectrometer data using the complete band shape least-squares algorithm simultaneously fit to multiple spectral features from multiple materials, Proceedings of the Third Airborne Visible/Infrared Imaging Spectrometer (AVIRIS) Workshop, ed. R. O. Green, *Jet Propulsion Laboratory Publication 91-28*, 2-3, 1991.

Clark, R.N., G.A. Swayze, and A.J. Gallagher, Mapping the mineralogy and lithology of Canyonlands, Utah with imaging spectrometer data and the multiple spectral features mapping algorithm, Summaries of the Third Annual JPL Airborne Geoscience Workshop, ed. R.O. Green, *Jet Propulsion Laboratory Publication 92-14*(1), 11-13, 1992.

Clark, R.N., and G.A. Swayze, A.J. Gallagher, T.V.V. King, and W.M. Calvin, The U.S. Geological Survey, digital Survey, Digital Spectral Library: Version 1: 0.2 to 3.0 μm, *U.S. Geological Survey Open-File Report 93-592*, 1326 pp., 1993a.

Clark, R.N., G.A. Swayze, K. Heidebrecht, A.F.H. Goetz, and R.O.Green, Comparison of methods for calibrating AVIRIS data to ground reflectance, Summaries of the Fourth Annual JPL Airborne Geoscience Workshop, ed. R.O. Green, *Jet Propulsion Laboratory Publication 93-26*(1), 35-36, 1993b.

Clark, R.N., R.O. Green, G.A. Swayze, G. Meeker, S. Sutley, T.M. Hoefen, K.E. Livo, G. Plumlee, B. Pavri, C. Sarture, S. Wilson, P. Hageman, P. Lamothe, J.S. Vance, J. Boardman, I. Brownfield, C. Gent, L.C. Morath, J. Taggart, P.M. Theodorakos, and M. Adams, Environmental Studies of the World Trade Center area after the September 11, 2001 attack, *U. S. Geological Survey Open-File Report OFR-01-0429*, 265 pp., 2001.

Clark, R.N., G.A. Swayze, K. E. Livo, R.F. Kokaly, T.V.V. King, J.B. Dalton, J.S. Vance, B.W. Rockwell, T. Hoefen, and R.R. McDougal, Surface reflectance calibration of terrestrial imaging spectroscopy data, Proceedings of the Eleventh JPL Airborne Earth Science Workshop, ed. R.O. Green, *Jet Propulsion Laboratory Publication 03-04*, 43-63, 2002.

Clark, R.N., G.A. Swayze, K. E. Livo, R.F. Kokaly, S.J. Sutley, J. B. Dalton, R.R. McDougal, and C. A. Gent, Imaging spectroscopy: Earth and planetary remote sensing with the USGS Tetracorder and Expert Systems, *J. Geophys. Res.*, 2003, in press.

Crowley, J.K., Mapping playa evaporite minerals with AVIRIS Data: A first report from Death Valley, California, *Remote Sensing of Environment*, *44*, 337-356, 1993.

Crowley, J.K., D.R. Zimbelman, Mapping hydrothermally altered rocks on Mount Rainier, Washington, with Airborne Visible/Infrared Imaging Spectrometer (AVIRIS) data, *Geology, 25*(6), 559-562, 1997.

Dalton, J.B., T.V.V. King, D.J. Bove, R.F. Kokaly, R.N. Clark, J.S. Vance and G.A. Swayze, Distribution of Acid-Generating and Acid-Buffering Minerals in the Animas River Watershed as Determined by AVIRIS Spectroscopy, *Proceedings of the ICARD 2000 Meeting*, Denver Colorado, 1541-1550, 2000.

Farmer, V.C., *The Infrared Spectra of Minerals*, Mineralogical Society, London, 539 pp., 1974.

Fleischer, M., *Glossary of Mineral Species*, Mineralogic Record, Tucson, Arizona, 192 pp., 1980.

Fu, K.S., D.A. Landgrebe, and T.L. Phillips: Information processing of remotely sensed agricultural data, *Proceeding of the IEEE*, *57*(4), 639-653, 1969.

Gao, B-C, K.B. Heidebrecht, and A.F.H. Goetz, Derivation of scaled surface reflectances from AVIRIS data, *Remote Sensing of Environment*, *44*(2), 165-178, 1993.

Goetz, A.F.H., and Vinay Strivastava, Mineralogical mapping in the Cuprite mining district, Proceedings of the Airborne Imaging Spectrometer (AIS) Data Analysis Workshop, *Jet Propulsion Laboratory Publication 85-41*, 22-29, 1985.

Goetz, A.F.H., and W.M. Calvin, Imaging spectrometry: spectral resolution and analytical identification of spectral features, Imaging Spectroscopy II, ed. G. Vane, *Proceedings of the International Society for Optical Engineering (SPIE)*, *834*, 158-165, 1987.

Goetz, A.F.H., and J.W. Boardman, Quantitative determination of imaging spectrometer specifications based on spectral mixing models: Proceedings of the International Geoscience and Remote Sensing Symposium, Quantitative Remote Sensing: *An Economic Tool for the Nineties (IGARSS '89)*, *2*, 1036-1039, Vancouver, Canada, July 10-14, 1989.

Green, R.O; M.L. Eastwood, C.M. Sarture, T.G. Chrien, M. Aronsson, B.J. Chippendale, J.A. Faust, B.E. Pavri, C.J. Chovit, J. Solis, M.R. Olah, O. Williams, Imaging spectroscopy and the Airborne Visible/Infrared Imaging Spectrometer (AVIRIS), *Remote Sensing of Environment*, *65*, 227-248, 1998.

Hapke, B., Bidirectional reflectance spectroscopy 1. Theory, *J. Geophys. Res.*, *86*, 3039-3054, 1981.

Hunt, G.R., Spectral signatures of particulate minerals in the visible and near infrared: *Geophysics*, *42*(3), 501-513, 1977.

Hunt, G.R., and J.W. Salisbury, Visible and near-infrared spectra of minerals and rocks: I silicate minerals, *Modern Geology*, *1*, 283-300, 1970.

Hunt, G.R., and J.W. Salisbury, Visible and near-infrared spectra of minerals and rocks: II. Carbonates, *Modern Geology*, *2*, 23-30, 1971.

Hunt, G.R., and R.P. Ashley, Spectra of altered rocks in the visible and near infrared, *Economic Geology*, *74*, 1613-1629, 1979.

King, T.V.V., R.N. Clark, C. Ager, G.A. Swayze, Remote mineral mapping using AVIRIS data at Summitville, Colorado, and the adjacent San Juan Mountains: in Proceedings: Summitville Forum '95, eds. H.H. Posey; J.A. Pendelton; and D. Van Zyl, *Colorado Geological Survey Special Publication 38*, 59-63, 1995.

Kneizys, F.X, E.P. Shettle, G.P. Anderson, L.W. Abrew, J.H. Chetwynd, J.E.A. Shelby, and W.O. Gallery, Atmospheric Transmittance/Radiance; Computer Code LOWTRAN 7, AFGL, Hanscom AFB, Massachusetts, 1989.

Kokaly, R.F., D.G. Despain, R.N. Clark, K.E. Livo, Mapping vegetation in Yellowstone National

Park using spectral feature analysis of AVIRIS data, *Remote Sensing of Environment, 84*, 437-456, 2003.

Kruse, F.A., K.S. Keirein-Young, and J.W. Boardman, Mineral mapping at Cuprite, Nevada with a 68-channel imaging spectrometer, *Photogrammetric Engineering and Remote Sensing*, *56*(1), 83-92, 1990.

Kruse, F.A., Chapter 11: Visible-Infrared Sensors and Case Studies, in *Manual of Remote Sensing*, ed. A.N. Rencz, John Wiley and Sons, New York, 567-612, 1999.

Landgrebe, D.A., Useful information from multispectral image data: another look, in *Remote Sensing: The Quantitative Approach*, eds. P.H. Swain, and S.M. Davis, McGraw-Hill, New York, 396 pp., 1978.

Livo, K.E., R.N. Clark, F.A. Kruse, and R.F. Kokaly, Characterization of hydrothermally altered rock and hot spring deposits at Yellowstone National Park using AVIRIS data, Summaries of the Eight JPL Airborne Science Workshop, ed. R.O. Green, *Jet Propulsion Laboratory Publication 99-17*, 259-266, 1999.

Martinez-Alonso, S.E., Study of the infrared spectra of phyllosilicates through direct measurements, quantum mechanical modeling, and analysis of AVIRIS imaging spectrometer data: relationships with environment of mineralization, Ph. D. Dissertation, University of Colorado Boulder, 232 pp., 2000.

McDougal R.R., Roger N. Clark, K. Eric Livo, Raymond F. Kokaly, Barnaby W. Rockwell, and J. Sam Vance, Preliminary materials mapping in the Oquirrh Mountains region for the Utah EPA Project using AVIRIS data, Summaries of the 8th Annual JPL Airborne Earth Science Workshop, NASA JPL AVIRIS Workshop, ed. R.O. Green, *Jet Propulsion Laboratory Publication 99-17*, 291-298, 1999.

Metz, C.E., Basic principals of ROC analysis, *Seminars in Nuclear Medicine, VIII(4)*, 283-298, 1978.

Miller, E. A., G. Klein, D. Juergens, K. Mehaffey, J. Oseas, R. Garcia, A. Giandomenico, R. Irigoyen, R. Hickok, D. Rosing, H. Sobel, C. Bruce, E. Flamini, R. Devidi, F. Reininger, M. Dami, A. Soufflot, Y. Langevin, G. Huntzinger, The Visual and Infrared Mapping Spectrometer for Cassini, in Cassini/Huygens: A Mission to the Saturnian Systems, ed. L. Horn, *Proceedings of the International Society for Optical Engineering (SPIE)*, *2803*, 206-220, 1996.

Ready, P.J., P.A. Wintz, S.J. Whitsitt, and D.A. Landgrebe, Effects of compression and random noise on multispectral data, *Proceedings of the Seventh International Symposium on Remote Sensing of the Environment*, Environmental Research Institute of Michigan, Ann Arbor, Mich., 1321-1343, 1971.

Saksena, B.D., Infrared hydroxyl frequencies of muscovite, phlogopite and biotite micas in relation to their structures, *Journal of the Chemical Society, Frarady Transactions*, *60*, 1715-1725, 1964.

Shipman, Hugh, and J.B. Adams, Detectability of minerals on desert alluvial fans using reflectance spectra, *J. Geophys. Res.*, *92*(B10), 10391-10402, 1987.

Simon, J.H., The combined use of multispectral remotely sensed data from the short wave infrared (SWIR) and thermal infrared (TIR) for lithological mapping and mineral exploration, *Fifth Australasian Remote Sensing Conference,* Perth, Western Australia, *1*, 371-380, 1990.

Stanich, C.G., and F.G. Osterwisch, Advanced operational hyperspectral scanners: MIVIS and AHS: *Proceedings of the First International Airborne Remote Sensing Conference and Exhibition*, Strasbourg, France, Sept. 11-15, 1994, vol. II, Environmental Research Institute of Michigan (ERIM), 191-203, 1994.

Swain, P.H., Fundamental of pattern recognition in remote sensing, in *Remote Sensing: The Quantitative Approach*, eds. P.H Swain, and S.M. Davis, McGraw-Hill, New York, 396 pp., 1978.

Swayze, G.A., R.N. Clark, S. Sutley, and A.J. Gallagher, Ground-truthing AVIRIS mineral mapping at Cuprite, Nevada, Summaries of the Third Annual JPL Airborne Geosciences Workshop, Volume 1: AVIRIS Workshop, R.O. Green, *Jet Propulsion Laboratory Publication 92-14*, *1*, 47-49, 1992.

Swayze, G.A., The hydrothermal and structural history of the Cuprite Mining District, southwestern Nevada: an integrated geological and geophysical approach, Ph. D. Dissertation, University of Colorado Boulder, 399 pp., 1997.

Swayze, G.A., K.S. Smith, R.N. Clark, S.J., Sutley, R.M. Pearson, J.S. Vance, P.L. Hageman, P.H. Briggs, A.L. Meier, M.J. Singleton, and S. Roth, Using imaging spectroscopy to map acidic mine waste, *Environmental Science and Technology*, *34*, 47-54, 2000.

Swayze, G.A., R.N. Clark, S.J. Sutley, C.A. Gent, B.W. Rockwell, D. L. Blaney, J.L. Post, and B.P. Farm, Mineral mapping Mauna Kea and Mauna Loa Shield Volcanos on Hawaii using AVIRIS data and the USGS Tetracorder spectral identification system: lessons applicable to the search for relict Martian hydrothermal systems, Proceedings of the Eleventh JPL Airborne Earth Science Workshop, ed. R.O. Green, *Jet Propulsion Laboratory Publication 03-04*, 373-387, 2002.

Telford, W.M., L.P. Geldart, R.E. Sheriff, and D.A. Keys, *Applied Geophysics,* Cambridge University Press, New York, 860 pp., 1976.

Vane, G., R.O. Green, T.G. Chrien, H.T. Enmark, E.G. Hansen, and W.M. Porter, The Airborne Visible/Infrared Imaging Spectrometer (AVIRIS), *Remote Sensing of Environment*, *44*(2/3), 127-144, 1993.